Performance Studies of Large Size Micromegas Detectors

Studien zum Betriebsverhalten von großflächigen Micromegas Detektoren

Masterarbeit der Fakultät für Physik
der
Ludwig-Maximilians-Universität München

vorgelegt von
Philipp Lösel
geboren in München

München, den 02.10.2013

Gutachter: Prof. Dr. Otmar Biebel

Abstract

In 2018 the Large Hadron Collider at CERN will be upgraded to a higher instantaneous luminosity of $3 \times 10^{34}\text{cm}^{-2}\text{s}^{-1}$. Due to the similarly increasing background hit rate in the Small Wheel region of the ATLAS experiment, the currently installed Monitored Drift Tube chambers will no longer be able to cope with the hit rate and they will be replaced by small strip Thin Gap Chambers and Micromegas detectors. The performance of these novel detectors is currently under test.

In this thesis the performance of a large Micromegas detector with an active area of $92 \times 102\text{cm}^2$ and equipped with resistive strip readout plane is investigated in three measurement campaigns. First in a testbeam with 120 GeV pions at SPS/CERN, in which scans along the strips and variation of the incident pion angle as well as voltage variations were performed. Using a reference telescope, consisting of four reference Micromegas with two-dimensional readout, spatial and angular resolution, efficiency, homogeneity and signal propagation time on the striplines of the readout structures were investigated. Second a dedicated measurement with cosmic muons in Garching/Munich is presented investigating the signal propagation time with improved timing. Third, the homogeneity of the large resistive strip Micromegas with respect to spatial and angular resolution, efficiency, pulse height and mechanical stability has been investigated in the Cosmic-Ray Facility, which is a high precision test facility developed by LMU Munich for the investigation of Muon Drift Tube chambers.

The large Micromegas chamber has shown efficiencies up to about 98 %. The averaged overall efficiency to cosmic muons is $\eta = (95.18 \pm 0.03)\,\%$. It has shown an averaged spatial resolution of $\overline{\sigma_{\text{sr}}} = (83.0 \pm 0.9)\,\mu\text{m}$ in the scan along the strips with perpendicular incident 120 GeV pions. The measurement in the Cosmic-Ray Facility has shown only a spatial resolution $\sigma_{\text{sr}} = (238.7 \pm 1.3)\,\mu\text{m}$ for track angles between $-1°$ and $1°$. It is not jet understood, why this result is three times higher. An angular resolution of $\sigma_\Theta \approx 5°$ for large angles of incidence could be achieved.

The analysis for the signal propagation time on the copper readout strips led to two slightly different results, that agree well within their respective uncertainties. It is $t_{\text{propagation}} = (5.60 \pm 0.64)\,\text{ns} \cdot \text{m}^{-1}$ for the scan along the detector strips with 120 GeV pions and $t_{\text{propagation}} = (6.59 \pm 0.57)\,\text{ns} \cdot \text{m}^{-1}$ for the measurement with cosmic muons. The averaged result agrees well with the literature value of $t_{\text{propagation}} = 5.64\,\text{ns} \cdot \text{m}^{-1}$.

Overall the detector showed a good performance.

Zusammenfassung

Im Jahr 2018 wird der Large Hadron Collider am CERN zu einer höheren instantanen Luminosität von $3 \times 10^{34}\mathrm{cm}^{-2}\mathrm{s}^{-1}$ aufgerüstet. Wegen der ähnlich stark ansteigenden Untergrundtreffenrate in der Small Wheel Gegend des ATLAS Experiments, sind die derzeitig dort installierten Monitored Drift Tube Kammern nicht länger in Lage mit der Trefferrate umzugehen und werden durch small strip Thin Gap Chambers und Micromegas Detektoren ersetzt. Das Betriebsverhalten dieser neuartigen Detektoren wird derzeitig untersucht.

In dieser Arbeit wird das Betriebsverhalten eines großflächigen Micromegas Detektors in drei Messaufbauten untersucht. Dieser Detektor hat eine aktive Fläche von $92 \times 102\mathrm{cm}^2$ und ist mit einer resistiven Ausleseebene ausgestattet. Die erste vorgestellte Messkampagne ist ein Teststrahl mit 120 GeV Pionen am SPS/CERN, in dem Messreihen entlang der Streifen, Veränderungen des Einfallswinkel der Pionen aber auch Messreihen mit verschiedenen Spannungen durchgeführt wurden. Mit einem Teleskop, bestehend aus vier Micromegas mit zweidimensionaler Auslese als Spureferenz, wurden Orts- und Winkelauflösung, Effizienz, Homogenität und die Signalausbreitungszeit auf den Streifenbahnen der Auslesestruktur untersucht. Als zweites wird eine Messung mit kosmischen Myonen in Garching/München vorgestellt, mit der die Signalausbreitungszeit mit verbesserter Zeitmessung untersucht wurde. Drittens, die Homogenität des großen Micromegas im Bezug auf Orts- und Winkelauflösung, Effizienz, Pulshöhen und mechanischer Stabilität wurde in einem Teststand mit kosmischer Strahlung untersucht. Der Teststand wurde von der LMU München für die Hochpräzesions Untersuchungen von Muon Drift Tube Kammern entwickelt.

Die große Micromegas Kammer zeigte Effizienzen bis zu 98 %. Die über den ganzen Detektor gemittelte Effizienz für kosmische Myonen is $\eta = (95.18 \pm 0.03)\,\%$. Sie hatte eine gemittelte Ortsauflösung von $\overline{\sigma_{\mathrm{sr}}} = (83.0 \pm 0.9)\,\mu\mathrm{m}$ in der Messreihe entlang den Streifen mit 120 GeV Pionen, die senkrecht zu der Detektorebene einfielen. Eine Ortsauflösung von $\sigma_{\mathrm{sr}} = (238.7 \pm 1.3)\,\mu\mathrm{m}$ für einen Einfallswinkel von -1° and 1° zeigte sich im Teststand mit kosmischen Myonen, es ist noch nicht verstanden, warum dieses Ergebnis einen Faktor drei größer ist. Für große Winkel konnte eine Winkelauflösung von $\sigma_\Theta \approx 5^\circ$ erreicht werden.

Die Analyse zur Signalausbreitungszeit auf den Kupfer Auslesestreifen führte zu zwei leicht unterschiedlichen Ergebnissen, die gut in ihren jeweiligen Unsicherheiten übereinstimmen. Für die Messreihe entlang den Detektorstreifen mit 120 GeV Pionen ist das Ergebnis $t_{\mathrm{propagation}} = (5.60 \pm 0.64)\,\mathrm{ns} \cdot \mathrm{m}^{-1}$ und $t_{\mathrm{propagation}} = (6.59 \pm 0.57)\,\mathrm{ns} \cdot \mathrm{m}^{-1}$ für die Messung mit kosmischen Myonen. Das gemittelte Ergebniss stimmt gut mit dem Literaturwert von $t_{\mathrm{propagation}} = 5.64\,\mathrm{ns} \cdot \mathrm{m}^{-1}$ überein.

Im Großen und Ganzen zeigte der Detektor ein gutes Betriebsverhalten.

Contents

1 Introduction

1.1 The Large Hadron Collider

The Large Hadron Collider (LHC) is a 14 TeV center of mass energy proton-proton collider at CERN[1]. It is embedded in a tunnel 100 m underneath Geneva with a circumference of 27km. The protons are led in bunches in two beampipes. Currently every 50 ns bunches collide in four interaction points. At each of these points experiments are installed, CMS[2], ATLAS[3], LHCb[4] and ALICE[5] (see figure 1.1).

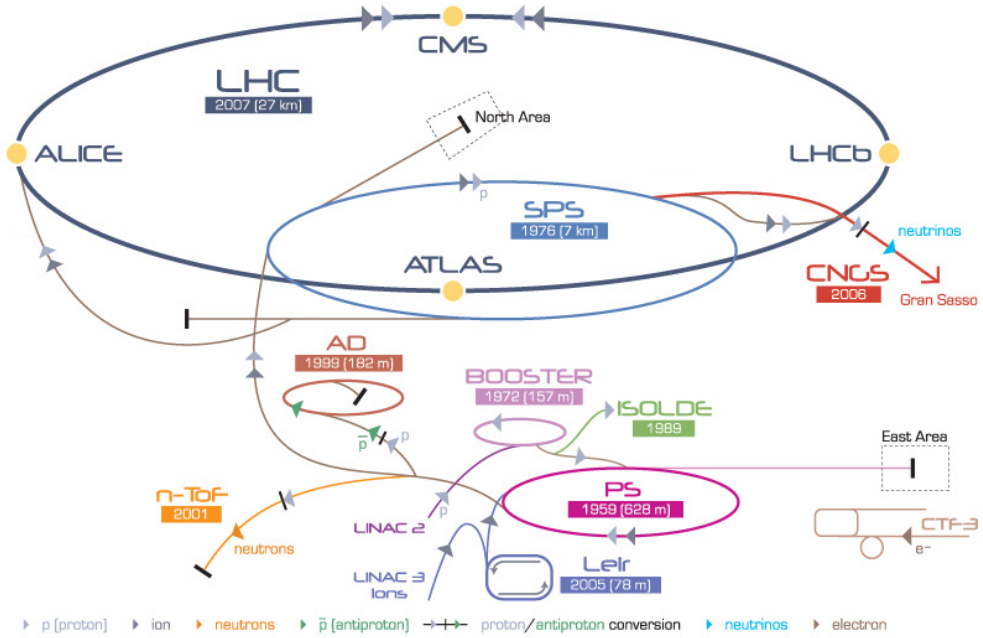

Figure 1.1: CERN accelerator complex: LHC with its experiments ALICE, ATLAS, CMS and LHCb, pre-accelerators Proton Synchrotron (PS) and Super Proton Synchrotron, LINear ACcelerators (LINAC), Low Energy Ion Ring (LEIR), Antiproton Decelerator (AD), CLIC Test Facility (CTF3), CERN Neutrons to Gran Sasso (CNGS), Isotope Separator OnLine DEvice (ISOLDE) and Neutrons Time of Flight (n-ToF). Taken from [CERN website, 2008].

ALICE is a general-purpose, heavy-ion detector which focuses on QCD[6], the

[1] Conseil Européen pour la Recherche Nucléaire
[2] Compact Muon Solenoid
[3] A Toroidal LHC ApparatuS
[4] Large Hadron Collider beauty
[5] A Large Ion Collider Experiment
[6] quantum chromodynamics

strong-interaction sector of the Standard Model. It is designed to address the physics of strongly interacting matter and the quark-gluon plasma at extreme values of energy density and temperature in nucleus-nucleus collisions [ALICE Collaboration, 2008].

The asymmetric LHCb detector is designed for precision measurements of CP violation and rare decays of B hadrons [LHCb Collaboration, 2008].

The CMS detector has been optimized for the search of the Standard Model Higgs boson over a mass range from 90 GeV to 1 TeV, but it also allows detection of a wide range of possible signatures from alternative electro-weak symmetry breaking mechanisms. CMS is also well adapted for the study of top, beauty and tau physics at lower luminosities and will cover several important aspects of the heavy ion physics program [CMS Collaboration, 2008]. The ATLAS detector will be treated separately in section 1.2.

The LHC was running in 2011 with a center of mass energy of 7 TeV and in 2012 with 8 TeV. About $25\,\mathrm{fb}^{-1}$ data were collected with an instantaneous luminosities up to of $6 \times 10^{32}\mathrm{cm}^{-2}\mathrm{s}^{-1}$. Currently there is an upgrade ongoing, after which almost the design center of mass energy will be reached and the bunch spacing reduced to 25 ns. Until the year 2018 up to $100\,\mathrm{fb}^{-1}$ data will be collected with the nominal luminosity of about $1 \times 10^{34}\mathrm{cm}^{-2}\mathrm{s}^{-1}$.

1.2 The ATLAS Experiment

The ATLAS experiment [ATLAS Collaboration, 2008] is like the CMS experiment a multipurpose experiment. It is searching for new discoveries in the head-on collisions of protons of extraordinarily high energy. It was designed for a broad physics program, including the search for the Higgs boson over a wide mass range.

The ATLAS detector has an onion-like layout, shown in figure 1.2. The Inner Detector begins a few centimetres from the beam axis. It measures inter alia the vertex position of the products of hard proton collisions. Around the Inner Detector the electromagnetic and hadronic calorimeters are arrange to measure the energy of the particles, which are stopped there. The outer most detector system is the Muon Spectrometer, which measures the muon track points.

1.3 Motivation

In 2018 the LHC will be upgraded to deliver an instantaneous luminosity of a factor two or three over design luminosity. With this higher luminosity, the mean number of interactions per bunch crossing, the so called pile up, will increase from the current value of 25 by a factor of five. The background hit rate will increase accordingly. The Monitored Drift Tubes (MDT) and Cathode Strip Chambers (CSC), which are currently integrated in the Small Wheel regions of the ATLAS detector, cannot handle this any more. To have a better performance at higher luminosity the ATLAS detector has to be upgraded. The upgrade in 2018 focuses on the end-cap region, especially the Small Wheels. The detector replacement is necessary in order to ensure the muon track resolution and the trigger performance.

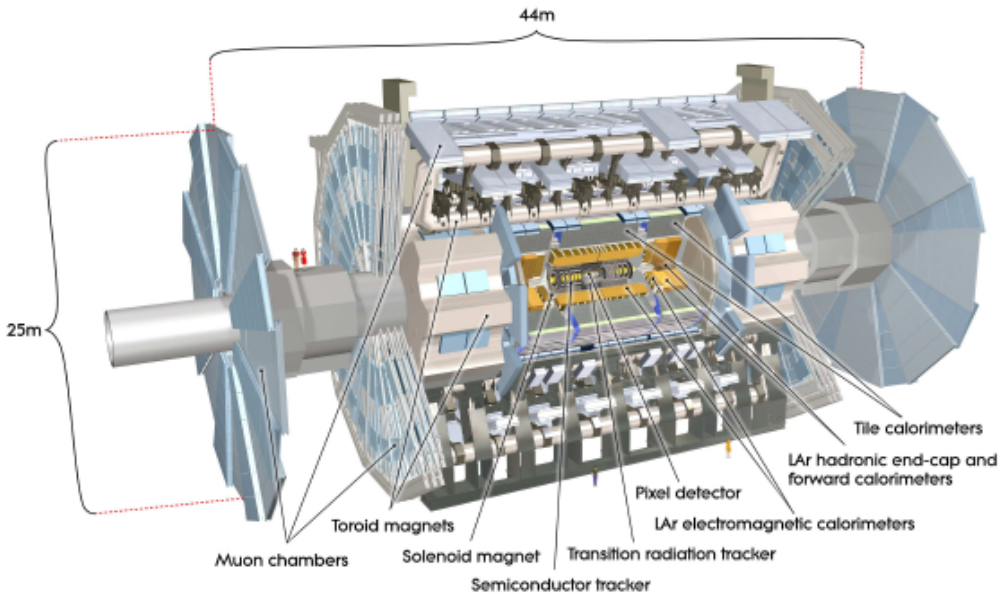

Figure 1.2: Cut-away view of the ATLAS detector, taken from [ATLAS Collaboration, 2008].

For this purpose small strip Thin Gap Chambers and Micromegas will be used. This Thesis covers only Micromegas issues.

The Small Wheel is separated in 16 sectors (see figure 1.3). The Micromegas detectors will be arranged in small and large sectors, which require detectors with a strip length of up to 2 m. Each sector consists of eight Micromegas layers, divided in two multiplets of four layers. Figure 1.4 (left) shows the schematic arrangement of these detectors. In the multiplets the Micromegas are mounted pairwise back-to-back (see figure 1.4 (right)) [ATLAS Collaboration, 2013].

Micromegas detectors should fulfill for that purpose the following requirement [Nikolopoulos et al., 2009]:

- High counting rate capability, for hit rates $> 20\,\mathrm{kHz/cm^2}$
- High single plane detection efficiency above 97 %
- Good spatial resolution of approximately 100 μm
- Second coordinate measurement
- Two-track separation at distance of 1 mm to 2 mm
- Good time resolution on the order of 5 ns to allow for bunch crossing identification
- Level-1 triggering capability
- Good aging properties

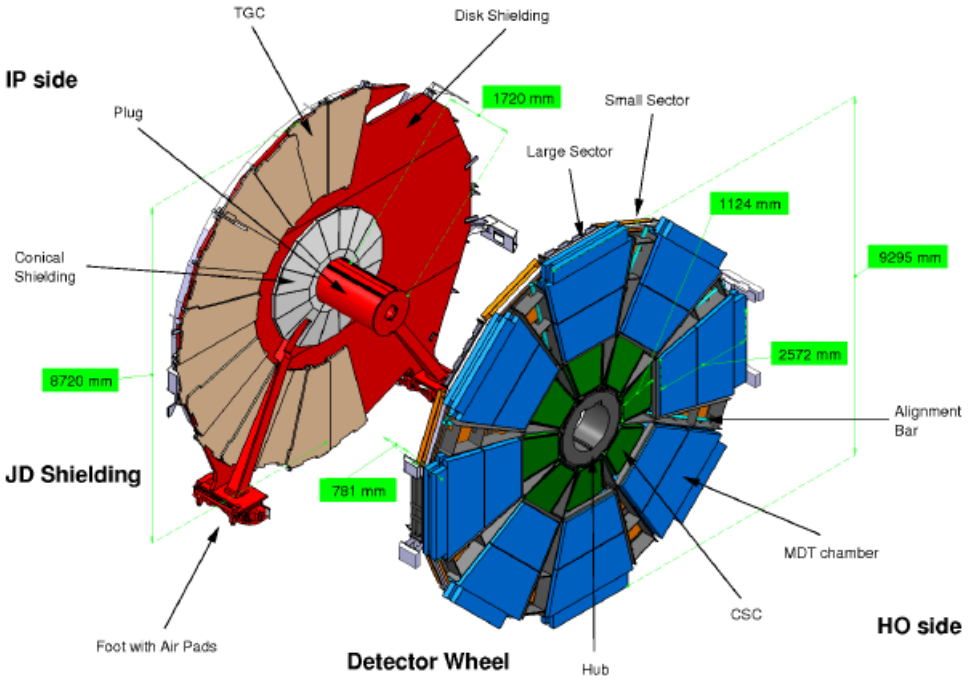

Figure 1.3: Components and layout of a present Small Wheel, taken from [ATLAS Collaboration, 2013].

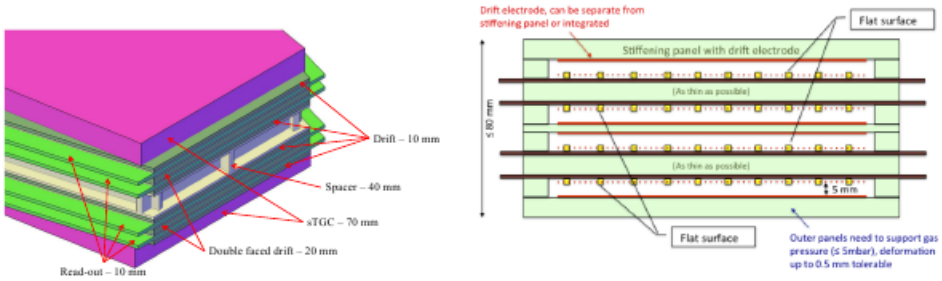

Figure 1.4: Arrangement of the detectors in a sector (left) and in a multiplet (right), taken from [ATLAS Collaboration, 2013].

In this thesis a large Micromegas detector is under investigation to measure its properties. Its spatial resolution, measured with high energy pions and cosmic muons, efficiencies, mechanical stability and pulse height homogeneity will be discussed. Furthermore it will be shown, that the signal propagation time for charge signal on the readout strips can be measured and, in timing applications, must be corrected for.

2 The Micromegas Detector

Particles are detected and investigated through their interaction with matter. This chapter describes these interactions, the working principle of Micromegas detectors and their current applications. As source for most of the theoretical background the textbook of Leo [Leo, 1994] was taken.

2.1 Interaction of Particles and Photons with Matter

2.1.1 Energy Loss According to Bethe-Bloch

One of the basic reactions of particle radiation in matter is the energy loss of a charged particle. The other is the deflection from its incident direction. These effects are based primarily on the particle's collision with atomic electrons and its scattering from nuclei. Other processes are Cherenkov radiation, nuclear reactions and bremsstrahlung, which are no further detailed here, since they are not relevant for Micromegas detectors. The average energy loss of charged particles per unit length is given by the Bethe-Bloch Formula (see Eq. (2.1)) with two corrections, the density effect correction δ and the shell correction C.

$$-\frac{dE}{dx} = 2\pi N_{\mathrm{A}} r_{\mathrm{e}}^2 m_{\mathrm{e}} c^2 \rho \frac{Z}{A}\frac{z^2}{\beta^2}\left[ln\left(\frac{2m_{\mathrm{e}}\gamma^2 v^2 W_{\max}}{I^2}\right) - 2\beta^2 - \delta^2 - 2\frac{C}{Z}\right] , \qquad (2.1)$$

with c: speed of light, r_{e}: classical electron radius, m_{e}: electron mass, N_{A}: Avogadro's number, I: mean excitation potential, Z, A and ρ: atomic number, atomic weight and density of absorbing material, z and v: charge in units of e and velocity of the incident particle, and $\beta = v \cdot c^{-1}$ of the incident particle, $\gamma = \left(\sqrt{1-\beta^2}\right)^{-1}$ and $W_{\max} \simeq 2m_{\mathrm{e}}c^2\beta^2\gamma^2$: maximum energy transfer to an electron in a single collision.

The so called stopping power $dE \cdot dx^{-1}$ is dominated by β^{-2}. It decreases with the increasing velocity of the incident particle until a velocity of $\beta\gamma \approx 0.96c$ is reached (see figure 2.1). At this point the energy loss distribution has a minimum. Particles with this energy are called minimum ionizing particles. Now the β^{-2} term is almost constant and the distribution rises again due to the logarithmic dependence of the Bethe-Bloch formula. [Leo, 1994, p. 24 ff.]

2.1.2 Photons

The three main processes for the interaction of photons with matter are the photoelectric effect, Compton scattering and pair production. Figure 2.2 shows the total photon absorption cross section for lead.

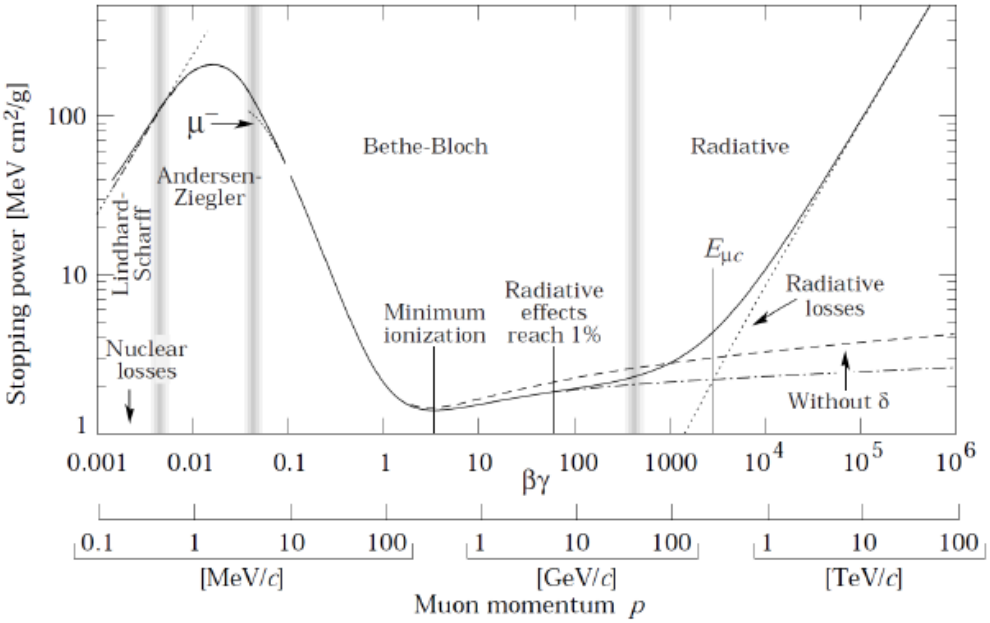

Figure 2.1: Stopping power for a positive charged muon in copper as a function of its momentum p, taken from [Groom et al., 2001].

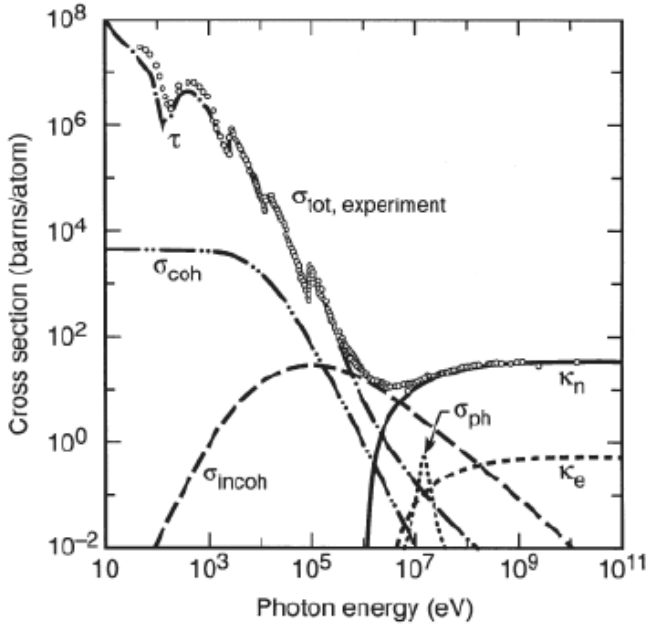

Figure 2.2: Total photon absorption cross section as a function of its energy in lead with contributions of atomic photo effect τ, coherent scattering σ_{coh}, incoherent (Compton) scattering σ_{incoh}, nuclear-field and electron-field pair production, κ_{n} and κ_{e} , and nuclear photo absorption σ_{ph}, taken from [Thomson, A. C. et. al., 2009].

The absorption of a photon by an atomic electron, followed by the emission of the electron from the atom is called photoelectric effect. Due to simultaneous energy- and momentum-conservation only bound electrons can be involved in this effect with the nucleus absorbing the recoil momentum.

For photon energies between 100 keV and 1 MeV the dominating effect is the Compton scattering. This can be understood as elastic scattering of a photon on an electron of the absorber material. The photon transfers some of its energy to the electron.

Pair production is the dominating process for higher energies. If the photon has at least energies above the pair-production threshold, it can convert into an electron-positron pair. This can only occur in the presence of a third body, to conserve the momentum. [Leo, 1994, p. 54 ff.]

2.1.3 Ionization

As previously explained, the two main processes of energy loss of charged particles in matter are ionization and excitation. Excitation has a cross section of $\sigma_{max} \simeq 10^{-17}\,\mathrm{cm}^2$ and ionization $\sigma_{max} \simeq 10^{-16}\,\mathrm{cm}^2$. Nevertheless excitation is in general the dominant process because of the relatively high energy threshold of ionization. The ionization directly created by an incident particle in the gas detector is called primary ionization. Positive ions and electrons are created. If the energy transfer to the electron through primary ionization is high enough, this electron creates new ion-electron pairs (secondary ionization). Such high energy electrons are called δ-electrons. In argon at normal temperature and pressure, the mean energy necessary to create an ion-electron pairs is 26eV [Beringer, J. et. al. (Particle Data Group), 2012].

In the absence of an external electric field the created electron can recombine with an ion or can be captured by a gas atom, forming a negative ion. The latter is especially relevant in electronegative gases such as oxygen.

In gas detectors the electrical field is used to separate the ion-electron pairs. The electrons drift to the positively charged anode and the ions to the negatively charged cathode. Their averaged velocity is called drift velocity and is limited by its collision with other particles. The drift velocity of electrons is about a factor of 1000 higher as for ions because of their mass and depends on the electric field and the pressure [Leo, 1994, p. 130 ff.]. Figure 2.3 shows the electron drift velocity as a function of the electric field for several gas mixtures of $Ar : CO_2$, simulated with Garfield [Garfield, 2013].

2.2 Avalanche Multiplication

Because of the small amount of primary electrons in a gas detector, the charge has to be multiplied for detection. In wire gas detectors, the drift field increases towards the very thin wire, reaching values sufficiently high for charge amplification. In Micromegas detectors, a planar high-field region is formed by a thin micro mesh, held at a distance of typically 100 um to the anode strips. By the strong electric

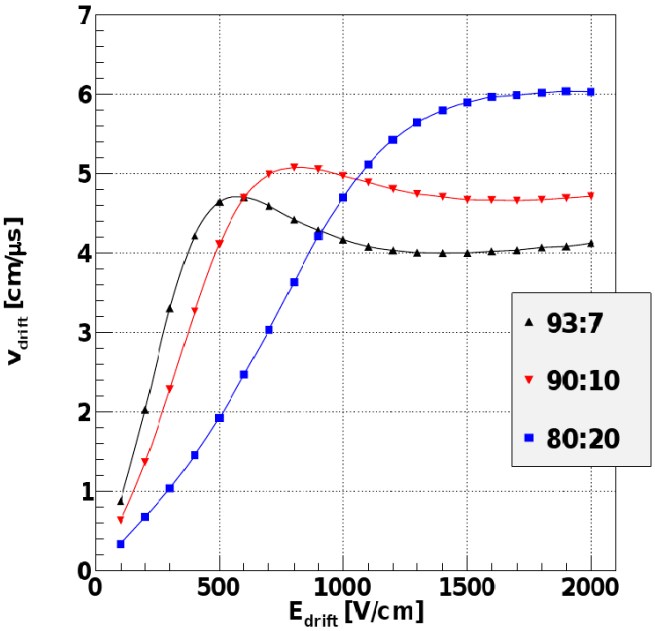

Figure 2.3: Electron drift velocity as a function of the electric field for several gas mixtures of $Ar : CO_2$, simulated with Garfield, taken from [Bortfeldt, 2013]

field in the amplification region the electrons are accelerated to high energies and create new electrons in collisions with gas atoms. The multiplication factor or gas gain M can be calculated with the first Townsend coefficient $\alpha = \lambda^{-1}$, where λ is the electrons mean free path:

$$M = \frac{n}{n_0} = \exp(\alpha x) \ , \tag{2.2}$$

where n is the number of produced electrons, n_0 is the number of initial electrons and x is the amplification distance.

In a uniform electric field the first Townsend coefficient is not a function of x. The gas gain is physically limited by the so called Raether limit ($\alpha x \approx 20$) above which breakdown occurs. [Leo, 1994, p. 135 f.]

2.3 Working Principle of a Micromegas Detector

Micromegas (MICRO-MEsh-GAseous Structure) detectors are planar gas detectors developed in 1996 for the detection of charged particles [Giomataris et al., 1996]. The upper picture in figure 2.4 shows a cross-section of a Micromegas detector.

If a muon crosses the detector, it ionizes the gas on its way. The ion-electron pairs get separated by the electric field in the drift region, which usually has a width of 5 mm. Due to the electric field the ions drift to the cathode and the electrons to the grounded mesh, which separates the drift and the amplification region. To keep a constant distance of 128 μm between the anode and the mesh, the mesh lies on pillars, which are spaced by 2.5 mm and have a height of 128 μm.

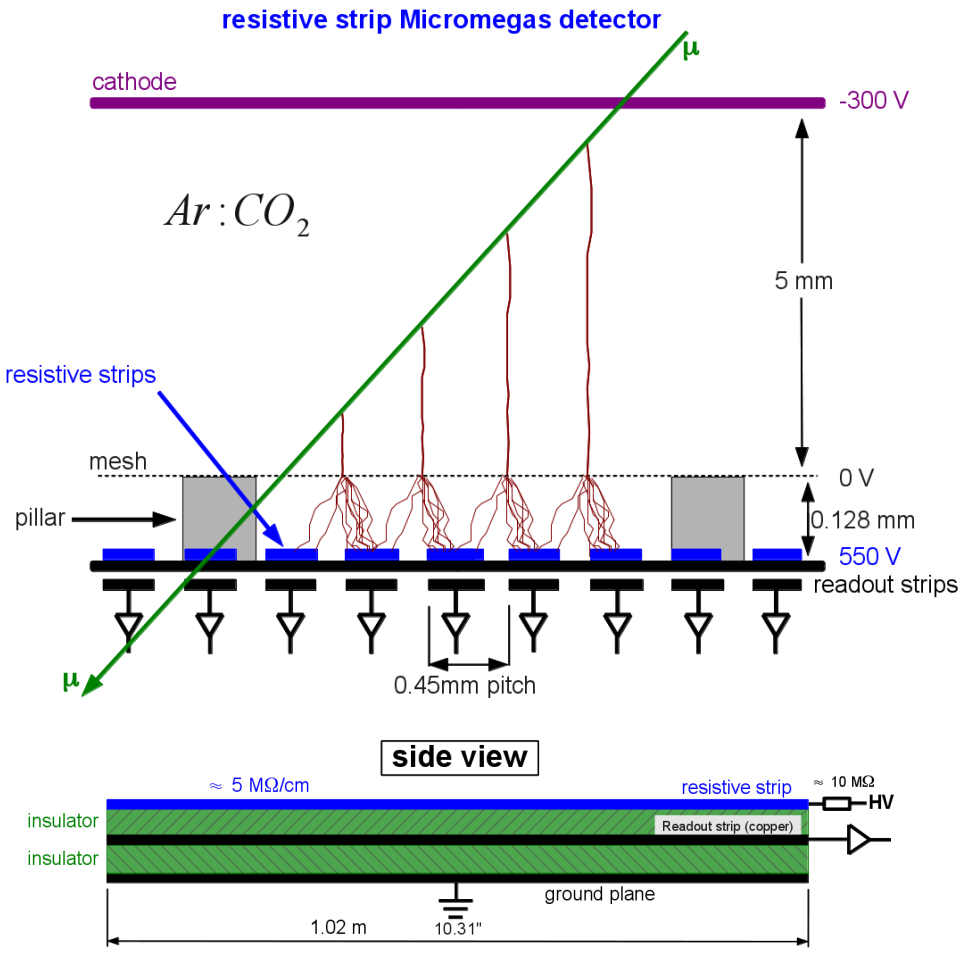

Figure 2.4: Scheme of a Micromegas detector (upper) and its sideview (lower).

In the amplification region the electrons are multiplied due to the high electric field with the mechanism, described in section 2.2. The charge is collected on the resistive strips with a resistivity of about 5 MΩ per cm. An insulator layer separates the resistive and the copper readout strips (see lower picture in figure 2.4). The Micromegas detector becomes spark-insensitive by adding a layer of resistive strips on top of the insulator above the readout strips. The readout strips are no longer exposed to the charge created in the amplification region, instead the signals are capacitively coupled to the strips [ATLAS Collaboration, 2013].

2.4 Current Applications

Since Micromegas detectors were developed about 15 years ago, they are currently used in diverse experiments. In the following, two examples are described.

Twelve planes of $40 \times 40\,\mathrm{cm}^2$ size Micromegas were installed in the COMPASS[1] experiment at CERN. They were operated with efficiencies up to 99%. The spatial resolution was determined using all twelve planes for tracking. In the central zone a value of 65 μm was optained at a strip-pitch of 360 μm. [Platchkov et al., 2003]

A Micromegas detector has been mounted on the CAST[2]-experiment at CERN. It showed good stability and an energy resolution of 25% (FWHM) was measured at 5.9 keV. [Andriamonje et al., 2004]

2.5 Technical Properties of the Micromegas Used in this Work

The test chamber (L1), which is investigated in this thesis, is a resistive strip Micromegas detector. It has 2048 resistive and readout strips (copper), which are about 102 cm long. The strip pitch is 0.45 mm, so its active area is $92.16 \times 102\mathrm{cm}^2$. The drift and amplification gaps are 5 mm and 128 μm wide. The detectors have been operated with an $Ar : CO_2$ 93:7 % vol gas mixture at atmospheric pressure for the measurement in the pion testbeam and with a small overpressure in the other measurements presented in this thesis. Because of the large size of the detector, it consists of two PCB[3] boards, glued together in the middle of the active area along the strips.

The four Micromegas reference chambers, used for the track determination during the scans of L1 with high energy pions, called Tmm2, Tmm3, Tmm5 and Tmm6, are also resistive strip Micromegas. But they have two dimensional readout and a strip pitch of 0.25 mm.

[1] COmmon Muon Proton Apparatus for Structure and Spectroscopy
[2] Cern Axion Solar Telescope
[3] Printed Circuit Board

3 Readout Electronics

In the following chapter, the readout electronics that have been used to read out the Micromegas in the test beam measurements at H6, in the laboratory in Munich and in the Cosmic Ray Facility will be described.

The copper readout strips are connected to the readout frontend boards via 130 pin Panasonic connectors [Panasonic Corporation, 2013]. Each frontend board carries a 128 channel, multiplexing, analogue pipeline APV25 chip. The APV25 integrates the collected charge on the strips. Usually two frontend boards are connected to build a master-slave pair. Through one HDMI[1] cable each pair is connected to the ADC[2] card on which the data are digitized and sent to the FEC[3] card. From the SRU[4] the data is transferred via ethernet to the readout system.

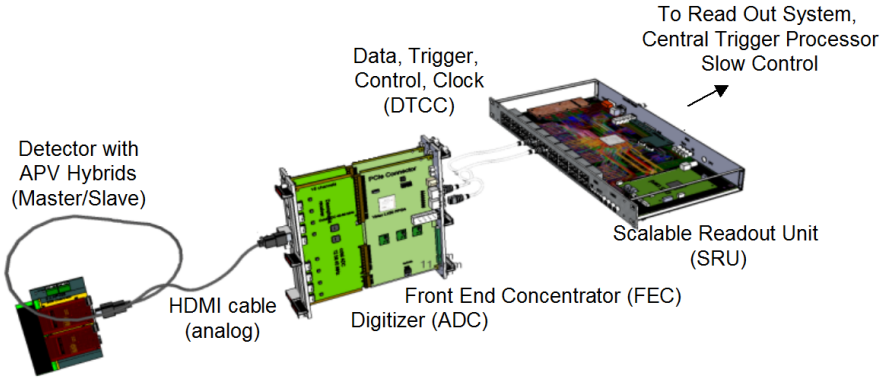

Figure 3.1: Scheme of the readout chain, taken from [Zibell, 2013].

3.1 The charge sensitive APV25 ASIC

The charge collected on the strips is read out by APV25 ASICs[5] based frontend boards (see figure 3.2). These ASICs were developed for the readout of silicon strip detectors in the vertex detector of the CMS experiment. Each of the 128 channels of the APV25 contains a charge sensitive preamplifier, a shaper and a 192 column deep analogue memory. The collected charge is integrated and written every 25ns to the analogue memory. This has been matched to the LHC bunch clock, running

[1] High Definition Multimedia Interface
[2] Analogue to Digital Converter
[3] Front End Concentrator
[4] Scalable Readout Unit
[5] Application Specific Integrated Circuit

at 40 MHz. After reception of a trigger, a configurable number of so called time bins can be read out. [Jones, 2001]

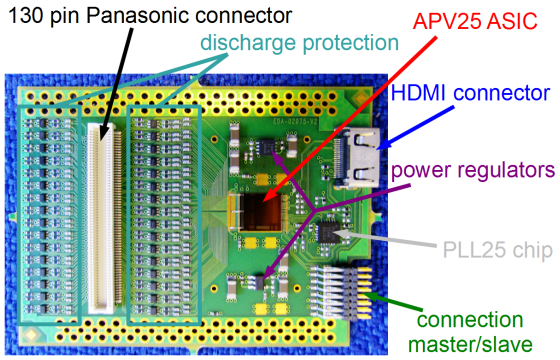

Figure 3.2: Picture of the frontend board with APV25 ASIC, Panasonic connector, power regulators (MAX8556), discharge protection (NUP4114), PLL25 chip [Placidi et al., 2000], HDMI connector and connector to another frontend board.

Figure 3.3 shows the circuit of one the 128 preamplifiers (left) and the of the memory pipeline (right). A schematic picture for the 192 column deep analogue memory for each preamplifier is shown in the left picture in figure 3.4 and the output of the selected columns in the right.

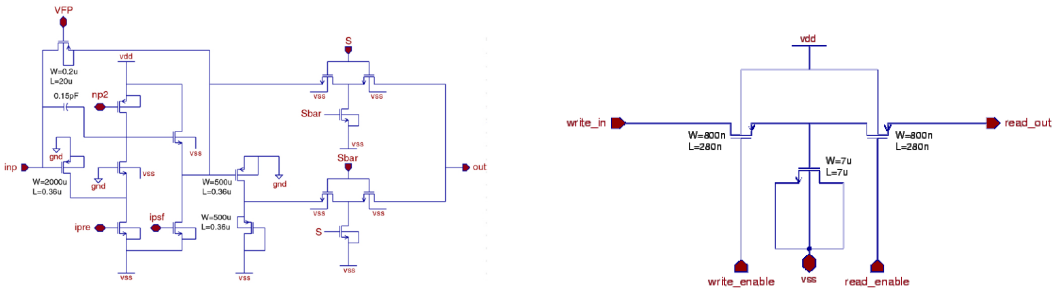

Figure 3.3: Circuit of one of the 128 preamplifiers (left) and the memory pipelines (right) on the AVP25 ASIC, taken from [Zibell, 2013].

Due to the randomly arriving muons and pions in the measurements made for this thesis, the trigger could not be synchronized with the clock of the APV25. With this asynchronicity the data has a 25 ns time jitter. But with additional time measurements the time jitter can be eliminated (see section 5.2 and 6.4.2).

3.2 The Scalable Readout System

The combination of ADC card, FEC card and SRU is called Scalable Readout System (SRS) [Martoiu et al., 2011]. The ADC card, which converts the analogue data from the APV25 ASICs to digital data, is with the FEC card one element in an Eurocrate. Further jobs of the FEC card are data formating, header generation and addition of time stamps. In the used ALtas data format (see figure 3.5 right)

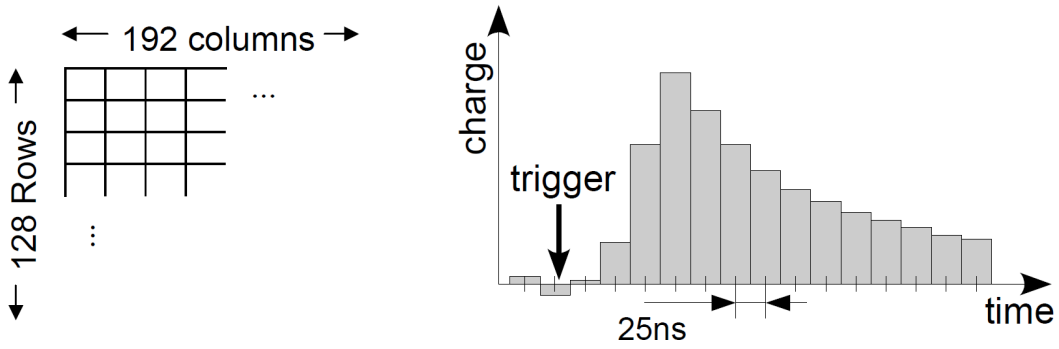

Figure 3.4: Schematics of the APV25 analogue memory (left) and the reead out signal (right), taken from [Zibell, 2013].

the SRS data is contained. The SRU can operate up to 40 FEC cards, adds new headers and converts the data into the ATLAS format. In the measurements for this thesis, where the SRS was used, the data were sent to the readout PC and then recorded.

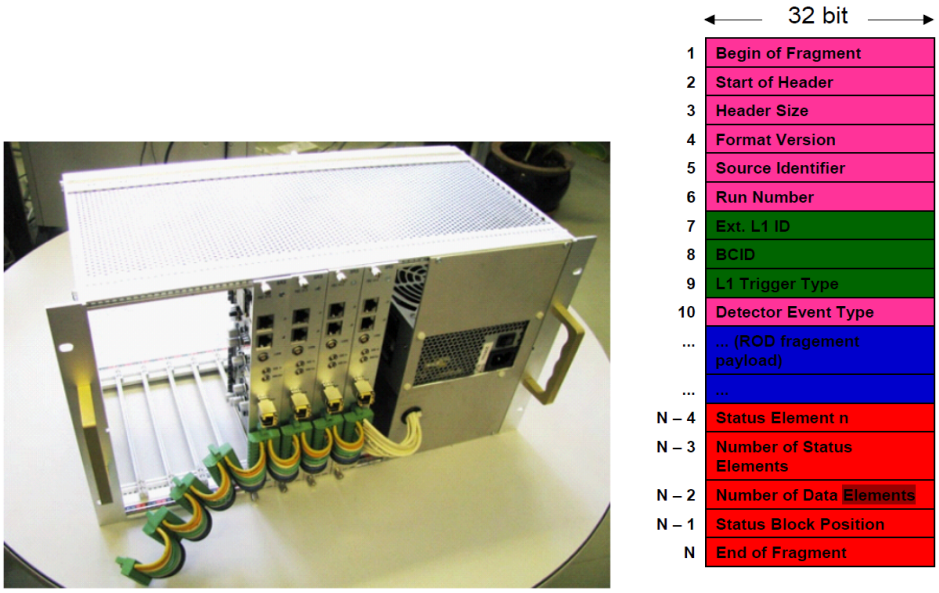

Figure 3.5: Photo of several FEC cards in a Eurocrate (left), taken from [Toledo et al., 2011], and the schematics of the ATLAS data format with its 32-bit words (right), taken from [Zibell, 2013].

3.3 FEC Standalone Mode

It is possible to operate the FEC card without SRU. In this case the FEC card gets directly the trigger and delivers the data via ethernet to the readout PC. If this readout system is used, the data acquisition is done with a program developed by the MAMMA collaboration, called mmdaq.

4 Analysis Tools

In this chapter tools which are needed for the analysis of the data are described.

4.1 Signal Fit

A typical signal can be seen in figure 4.1. The physical information is contained in the rise of the signal. The information, that is extracted by fitting, is the signal starting point and the charge. The charge is represented by the maximum of the signal. The time information is a little bit more complicated, as the signal rise must be fitted with the inverse Fermi function $q(t)$:

$$q(t) = \frac{q_0}{1 + \exp(\frac{t_0 - t}{\Delta t})} + q_{\text{pedestal}} \ . \tag{4.1}$$

t_0 is the time when half of the maximum charge is reached. Δt is the width of the signal rise. 10% and 90% of the maximum charge are reached at the time $t(0.1 \cdot q_0) = t_0 - \ln 9 \cdot \Delta t$ and $t(0.9 \cdot q_0) = t_0 + \ln 9 \cdot \Delta t$, respectively. These two points and $t(0.5 \cdot q_0) = t_0$ lie on a straight line, which can be extrapolated to the signal baseline to approximate the starting point of the signal t_s (see Eq. (4.2)).

$$t_\text{s} = t_0 - \frac{\ln 9}{0.8} \Delta t \tag{4.2}$$

This is also shown in figure 4.1. From now on t_s is always used for every time information, unless otherwise stated.

If the fit of the signal rise does not converge, the signal is interpreted as noise. Accidentally acquired noise signals can be discriminated from real signals by comparing the fit results. For noise, the signal width can be too narrow, so there is only charge in one timebin. If the maximum charge is smaller than 100 ADC counts, the signal is also unphysical, e.g. is created by an upward fluctuation of the baseline, because the true charge spectrum starts at higher charge. The signal has to start after a certain time after the trigger, due to the finite drift time of the electrons in the Micromegas detector. If it starts too long after the trigger it is most probably no signal. The smaller the quadratic deviation χ^2 between fit and data points the better is the fit. So if the χ^2 is high, the fit did not converge and the fit parameters are not very good. To exclude the noise, cuts were made on the fit parameters:

- $q_0 > 100$ [ADC counts]
- $0.1 < \Delta t < 2$ [timebins]
- $0 < t_0 < 13$ [timebins]

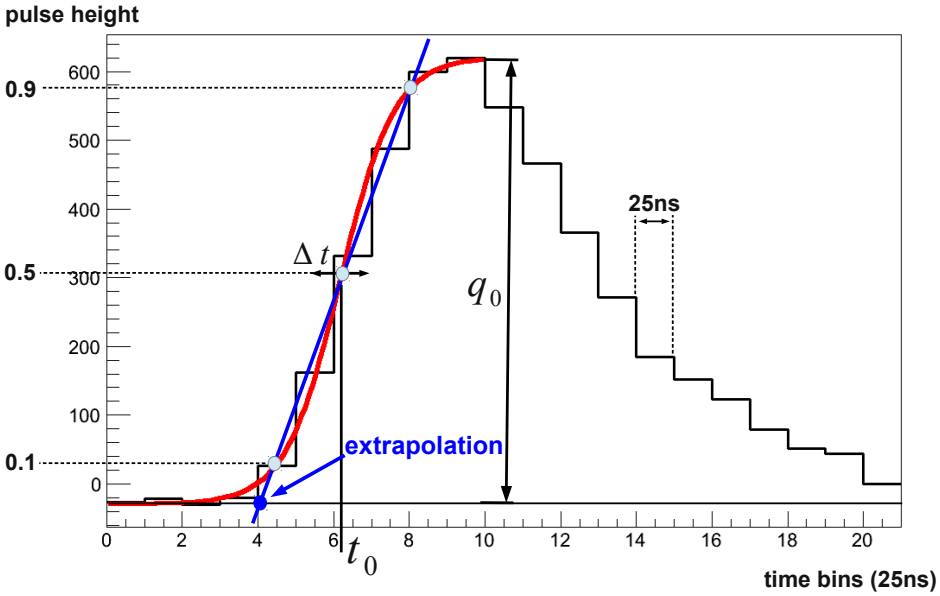

Figure 4.1: Strip signal with fit and extrapolation.

- $\frac{\chi^2}{NdF} < 50$

where NdF is the number of degrees of freedom of the fit.

4.2 Cluster Reconstruction

When the detector is hit, usually more than one strip registers a signal. Each incident particle creates a so called cluster, which has to be reconstructed.

Clusters are characterized by the following properties. The cluster charge q_{clu} is the sum over all strip charges within a cluster. As charge of a strip, the maximum value of the signal shape is taken. The cluster position x_{clu} is the average over the strip number weighted with its charge:

$$x_{\text{clu}} = \frac{\sum_{\text{strips}} x_{\text{strip}} \cdot q_{\text{strip}}}{q_{\text{clu}}} \,. \tag{4.3}$$

In the following, the charged average cluster position will be called centroid method. Figure 4.2 shows the cluster charge with the typical Landau distribution. The first peak in this distribution is noise. Figure 4.3 shows the cluster position for one run. The peaks in this distribution are noisy strips, created by e.g. strips which are accidentally soldered together.

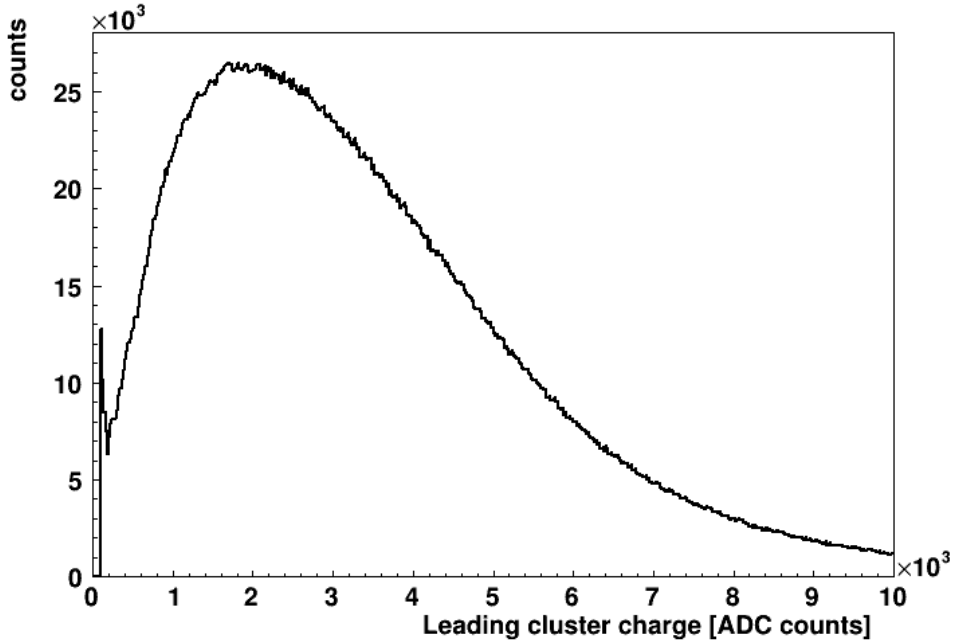

Figure 4.2: Distribution of the cluster charge.

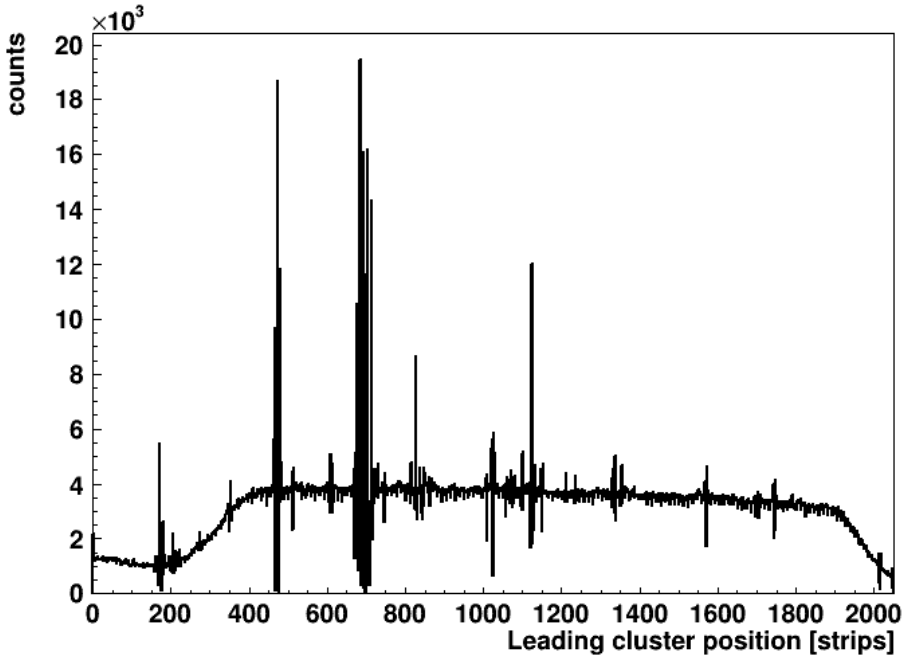

Figure 4.3: Distribution of the cluster position.

4.3 Fit of Straight Lines

The method for the reconstruction of a straight track is taken from [Horvat, 2005, p. 194]. Slope m and intersection b of a straight track $x = mz + b$ reconstructed through the track points $(x_\mathrm{i}, z_\mathrm{i})$, i = 1,...,N are determined by minimizing the χ^2-function (see Eq. (4.4)). N is the number of detectors used for the track fit. The track points are recorded in the reference detectors and weighted with their estimated spatial resolutions $\tilde{\sigma}_\mathrm{i}$.

$$\chi^2 = \sum_{\mathrm{i}=1}^{\mathrm{N}} \frac{1}{\tilde{\sigma}_\mathrm{i}^2}(x_\mathrm{i} - b - mz_\mathrm{i})^2 \ , \tag{4.4}$$

From the minimization requirements $\frac{\partial\chi^2}{\partial b} = 0$ and $\frac{\partial\chi^2}{\partial m} = 0$ follows:

$$\begin{aligned} \sum_{\mathrm{i}=1}^{\mathrm{N}} \frac{1}{\tilde{\sigma}_\mathrm{i}^2}(x_\mathrm{i} - b - mz_\mathrm{i}) = 0 \ , \\ \sum_{\mathrm{i}=1}^{\mathrm{N}} \frac{z_\mathrm{i}}{\tilde{\sigma}_\mathrm{i}^2}(x_\mathrm{i} - b - mz_\mathrm{i}) = 0 \ . \end{aligned} \tag{4.5}$$

The new parameters g_1, g_2, Λ_{11}, Λ_{12} and Λ_{22} are defined as

$$(g_1, g_2) = \sum_{\mathrm{i}=1}^{\mathrm{N}} \frac{x_\mathrm{i}\,(1, z_\mathrm{i})}{\tilde{\sigma}_\mathrm{i}^2} \ , \tag{4.6}$$

$$(\Lambda_{11}, \Lambda_{12}, \Lambda_{22}) = \sum_{\mathrm{i}=1}^{\mathrm{N}} \frac{(1, z_\mathrm{i}, z_\mathrm{i}^2)}{\tilde{\sigma_\mathrm{i}}^2} \ . \tag{4.7}$$

Inserting (4.7) in (4.5) gives

$$\begin{aligned} \Lambda_{11} b + \Lambda_{12} m = g_1 \ , \\ \Lambda_{12} b + \Lambda_{22} m = g_2 \ . \end{aligned} \tag{4.8}$$

That yields the result

$$b = \frac{1}{\mathrm{D}}\,(g_1\Lambda_{22} - g_2\Lambda_{12}) \tag{4.9}$$

and

$$m = \frac{1}{\mathrm{D}}\,(-g_1\Lambda_{12} + g_2\Lambda_{11}) \ , \tag{4.10}$$

where

$$\mathrm{D} = \Lambda_{11}\Lambda_{22} - \Lambda_{12}^2 \tag{4.11}$$

Eq. (4.9) and Eq. (4.10) are intersection and slope of the reconstructed particle's track.

4.4 μTPC Mode

In gas detectors the created ionization electrons have a finite drift velocity v_{drift}. So the electrons created nearby the cathode arrive later at the readout than those electrons created closer to the anode (see figure 4.4). This time difference for the electrons created along the path of the minimum ionizing particle can be used for the reconstruction of the track angle. If it is possible to measure the arrival time of charge clusters on strips, this so called μTPC method can be used.

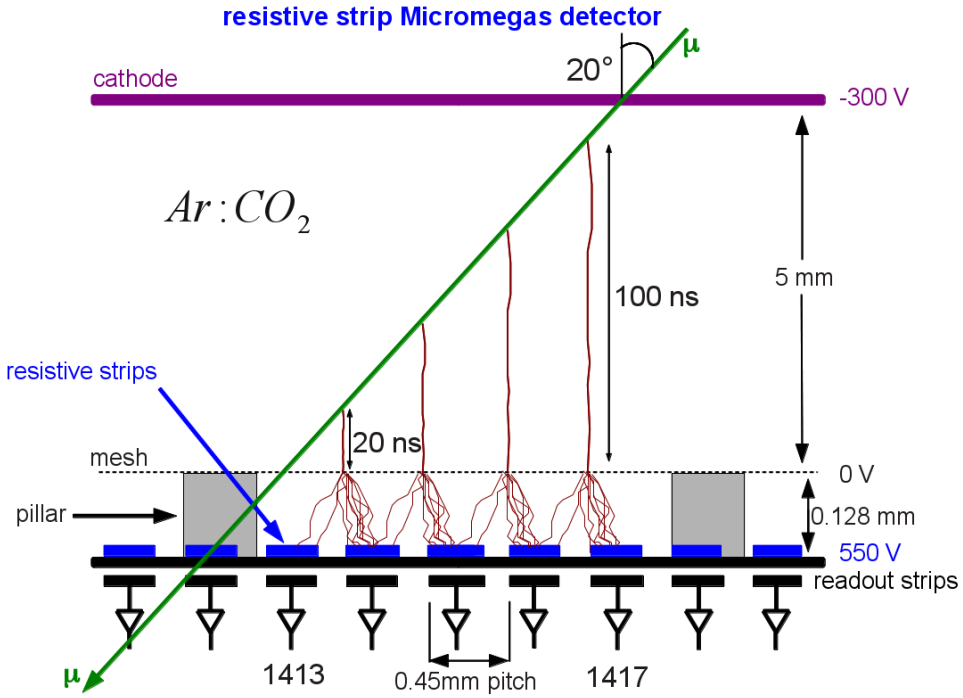

Figure 4.4: Scheme of a muon track through the Micromegas for the angle reconstruction with different drift times for different ionization along the muon path.

The name is inspired by the Time Projection Chamber, which is a gas detector for tracking and momentum measurement in the same volume [Nygren and Marx, 1978]. With Micromegas detectors it is possible to reconstruct the angle of incidence Θ in only one plane:

$$\Theta = \arctan\left(\frac{\mathrm{p}}{m \cdot v_{\text{drift}} \cdot \mathrm{tb}}\right) , \tag{4.12}$$

where p is the pitch of the strips, tb the length of one timebin (25 ns) and m the slope of the fitted straight line (Eq. (4.9)) in the time-strip-space.

The time-strip number-correlation is fitted with a straight line (see figure 4.5 (lower)), with the method described in section 4.3. As weight for the data points the strip charge normalized to the cluster charge is taken.

The upper picture in figure 4.5 shows a cluster with the typical signal shape. It can be seen, that the signal starts on each strip at different times.

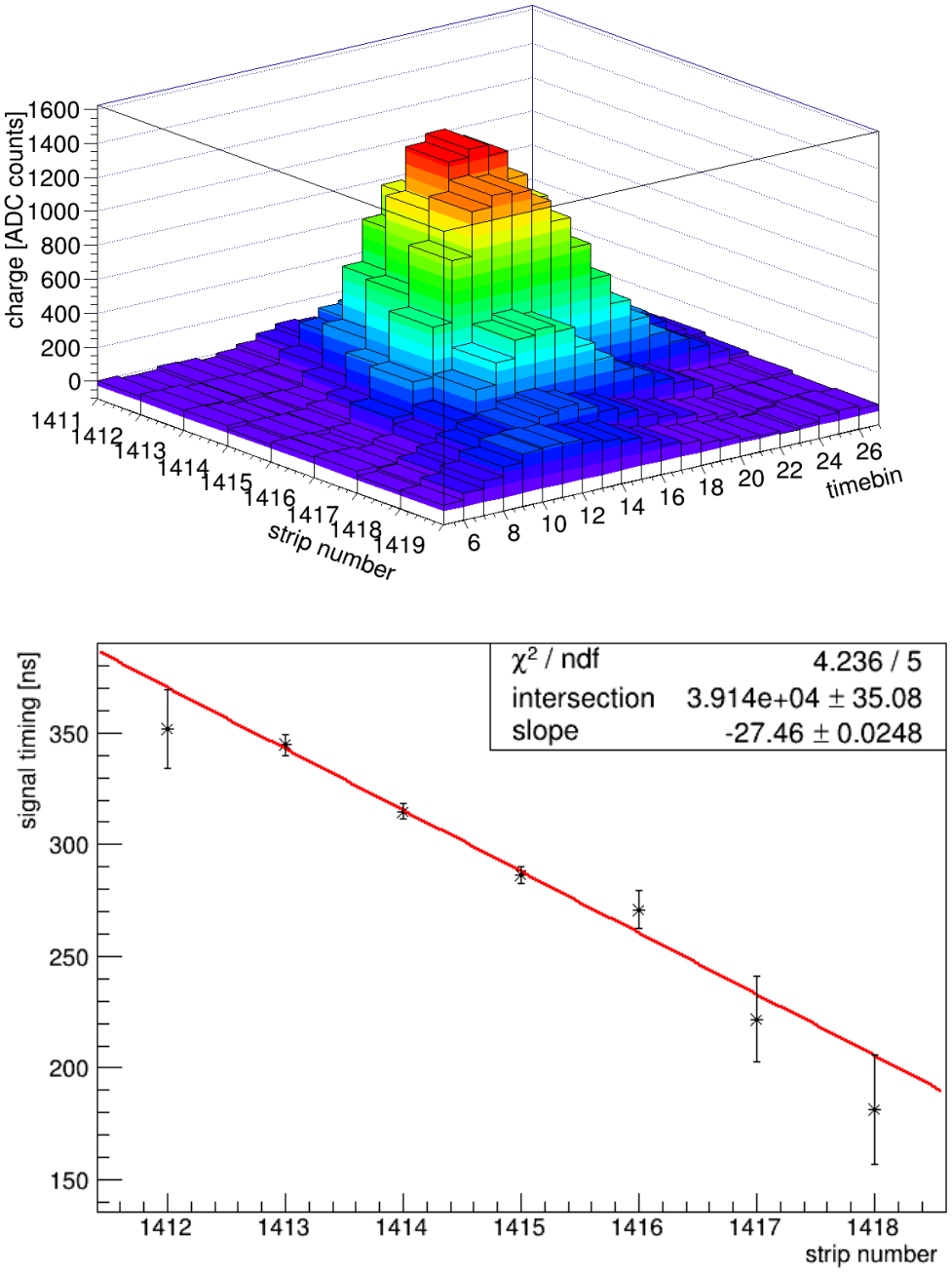

Figure 4.5: Eventdisplay for one cluster (upper) and the extracted signal timing versus the strip number for that cluster (lower).

5 Measurements

In order to investigate the large Micromegas chamber three measurement campaigns were performed. First a measurement with a telescope of Micromegas detectors in a pion testbeam at SPS/CERN. Second, a measurement with Cosmic muons without reference detectors to investigate the signal timing. And a third in the Cosmic-Ray Facility in Garching/Munich with two MDT chambers as reference detectors, which have a very good spatial resolution.

5.1 Pion Testbeam at SPS/CERN

The pion testbeam is at SPS is a well-defined and well focused beam with high energy. It is a perpendicular to the detector planes and has low multiple scattering. So the tracking of the pions is easy . It is a good possibility to study spatial resolution.

5.1.1 Experimental Setup

The behaviour of the $1\,\mathrm{m}^2$ large Micromegas chamber L1 has been investigated with 120 GeV pions. The 120 GeV pion beam was generated at the CERN North Area from an intense 450 GeV proton beam. Tracks were monitored with a detector telescope, consisting of four reference chambers (see figure 5.1). The beam was perpendicular to the reference detectors. It was possible to rotate the L1 chamber around the y-axis. Runs were taken to investigate the angular reconstruction via μTPC mode as a function of the angle of incidence. The telescope has a full length of about 1 m with two pairs of reference chambers, each pair separated by about 5.5 cm. Between the pairs of reference detectors eight small test chambers were installed, but not used for this analysis. The L1 chamber had a distance of 41.1 cm to the telescope (see figure 5.1).

The strips of the L1 chamber were oriented along the y-axis. For each detector the connector of the strips along the y-axis were on its upper side. The connectors of the reference detector for the strips along the x-axis are in figure 5.1 behind the chambers. The coincidence signal of two scintillators, one located before the test chamber and one after the telescope, were used as trigger. About 250 runs, each with 20000 events, were taken with the FEC standalone version and mmdaq (see section 3.3). Different measurements were performed: scans along the strips, variations of the voltages and rotations of the test chamber. As drift and amplification voltages 300 V and 550 V were used.

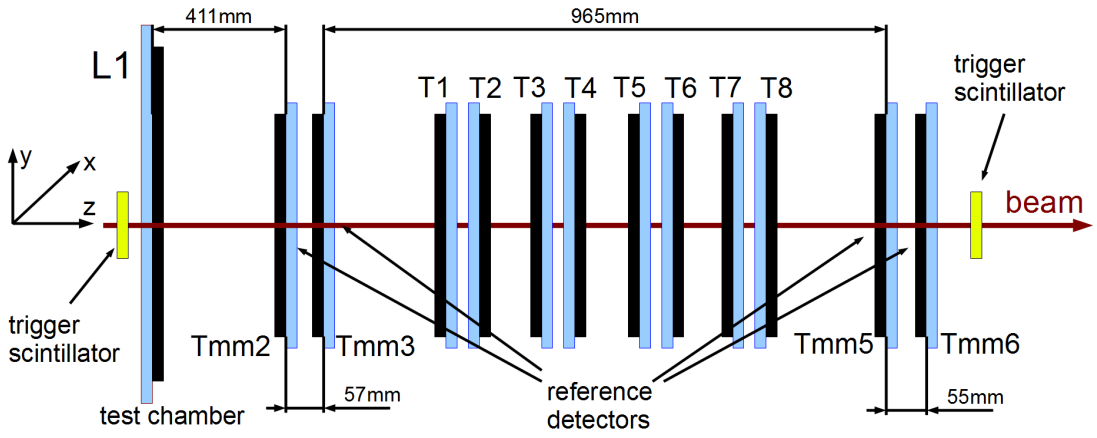

Figure 5.1: Schematic setup of the telescope in the testbeam.

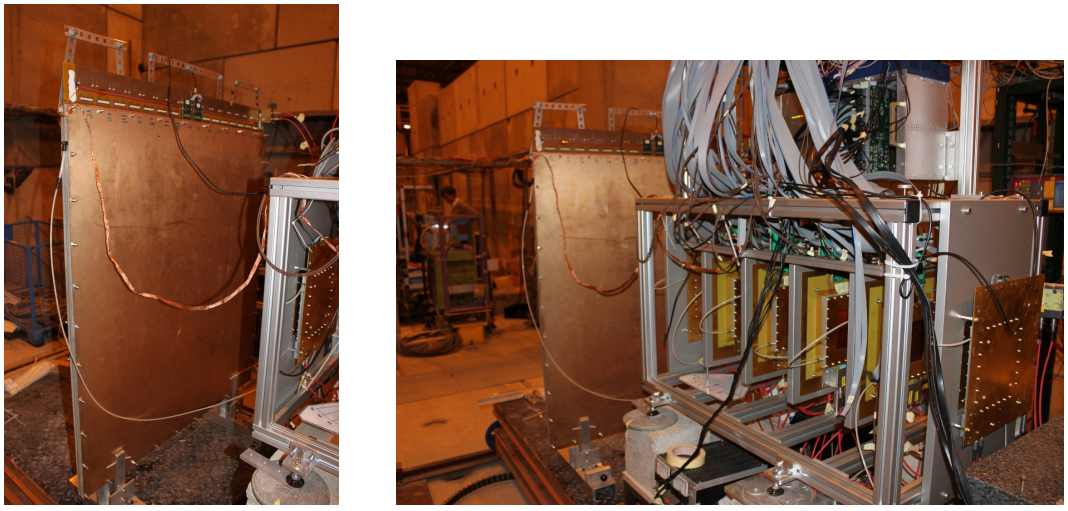

Figure 5.2: Photos of the setup in the testbeam.

5.1.2 Scans Along the Strips

The beam spot used for this testbeam was only about 1 cm^2 in area. In order to investigate the homogeneity of the large detector, it was scanned in y-direction (see figure 5.3). One y-scan was made in the middle of the detector with connectors 5 to 12 attached to APV25 frontend boards. And two on the edges of the detector on the left side with connector 1 and 2 and one on the right side with connector 15 and 16 attached to the APV25 frontend boards. During the two latter scans the strips of the reference detectors perpendicular to the strips of the test chamber were not read out any more.

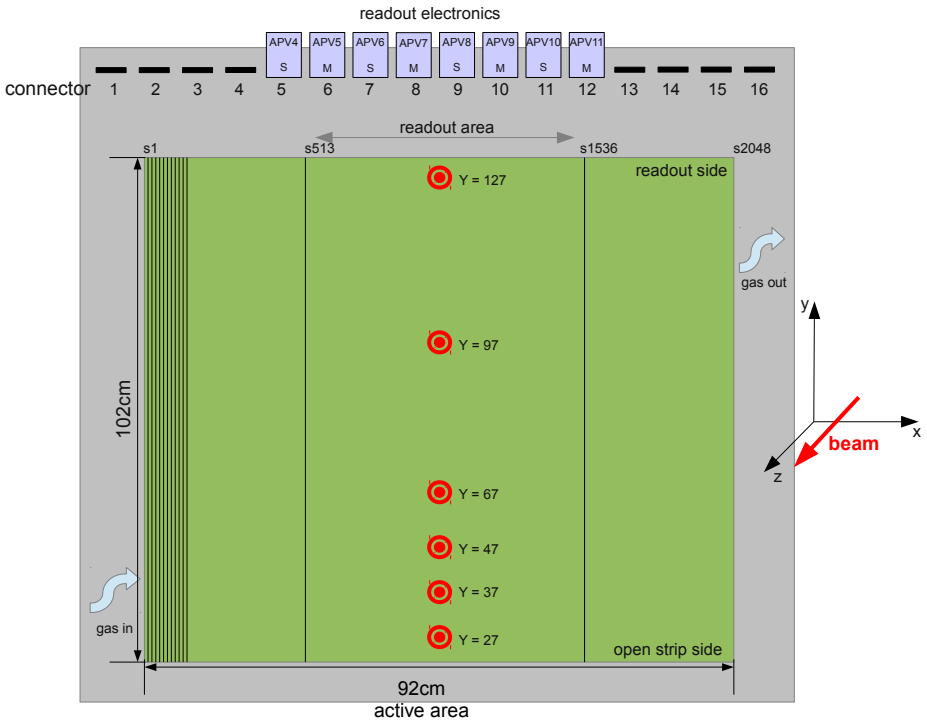

Figure 5.3: Schematic of the test chamber with y positions.

5.1.3 Alignment

The following alignment was made for each scan along the strips and the rotation runs separately.

The position and orientation of the four reference detectors and the detector under investigation has to be aligned precisely. In the following an iterative algorithm for automatic alignment is presented. Rotations are allowed around the z axis and shifts along the x- and y-axis. The pions from the beam pass the detectors on straight lines.

In this analysis the leading cluster is used for position determination in each detector, that means the cluster with the highest cluster charge, and only events

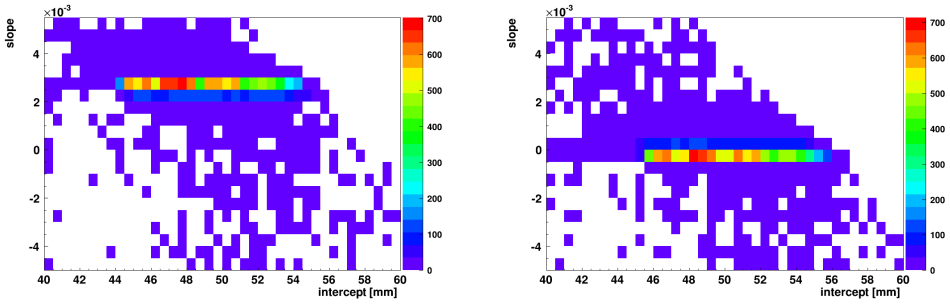

Figure 5.4: Distribution slope versus intercept of the track before correction (left) and after correction (right).

with at least one hit in every reference detector.

It is assumed, that the beam is perpendicular to the detectors and horizontal, so the slope of the track should vanish. If it were not, it would change the effective strip-pitch. But the corrections of the track angle are so small, that it doe not matter. In the first step of the alignment only the first and the last reference detector (Tmm2 and Tmm6) are used for the fit. The fit has to be done for the x- and y-coordinate separately. If the track slopes are not zero (see figure 5.4 (left)) the position of the last detector (Tmm6) has to be corrected by x_{cor} and y_{cor}, given by the mean value of the track slope $\overline{m}$ times the difference in the z-position of the two detectors $\Delta z = 1077\,\mathrm{mm}$ (see figure 5.5):

$$x_{\mathrm{cor}} = \overline{m_{\mathrm{x}}} \cdot \Delta z \tag{5.1}$$

and

$$y_{\mathrm{cor}} = \overline{m_{\mathrm{y}}} \cdot \Delta z \ , \tag{5.2}$$

where $\overline{m_{\mathrm{x}}}$ and $\overline{m_{\mathrm{y}}}$ are the mean values of the the slope for x- and y-coordinate.

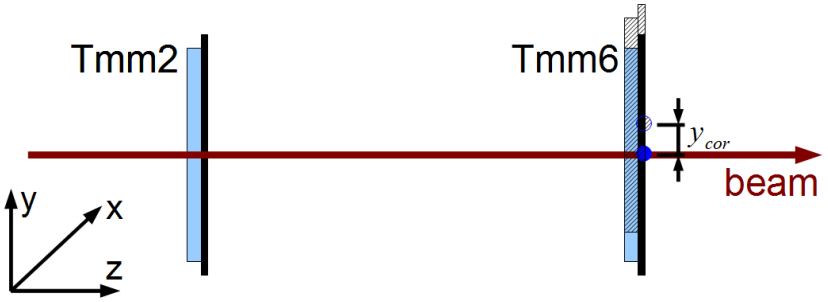

Figure 5.5: Scheme of the Tmm6 correction y_{cor} in the telescope, where the grey shaded detector shows the position before the correction.

The second step is the alignment of the positions of the two reference detectors in the middle. For that the residual distribution is used. The residual is the difference of the calculated position of the track defined by Tmm2 and Tmm6 for the respective z-position and the position of the hit in the detectors Tmm3 and Tmm5. For the hit position the cluster position is used. In figure 5.6 a scheme of

the position corrections of the detectors is shown. They have to be shifted by the value of the Gaussian mean of these distributions Δr_{Tmm3} and Δr_{Tmm5} (see figure 5.7).

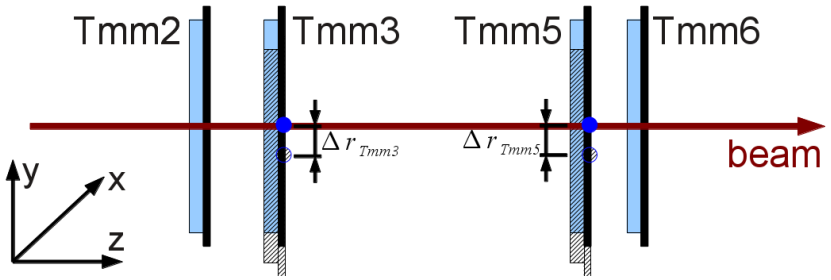

Figure 5.6: Scheme of the Tmm3 and Tmm5 corrections Δr_{Tmm3} and Δr_{Tmm5}, where the grey shaded detectors show their position before the correction.

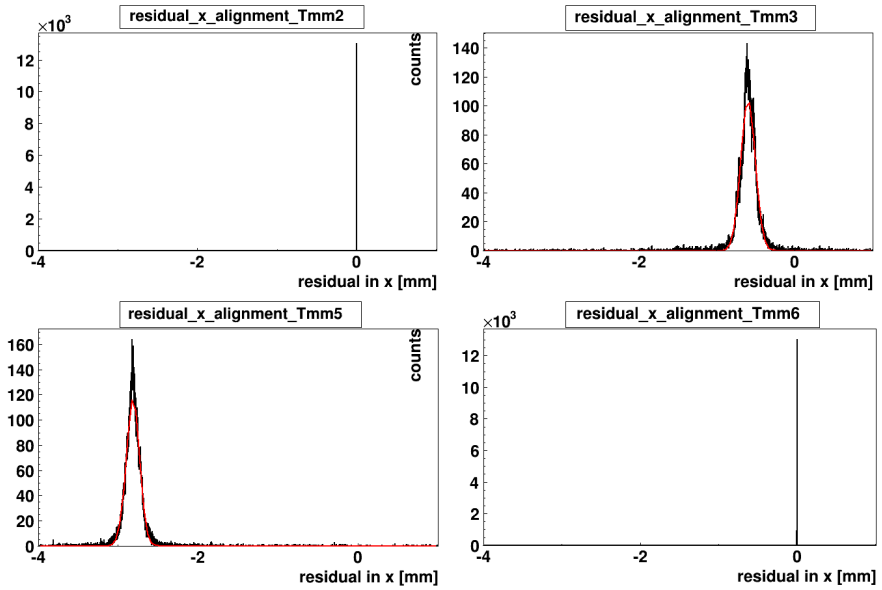

Figure 5.7: Residual distributions for the telescope detectors in step 2 of the alignment procedure before corrections. Two distributions are exactly zero, because only these to detectors were used for the track fit.

After the alignment of the reference detectors the mean of the residual distribution is zero (see figure 5.8) and all of them can be used for the fit of the track. Then the position of the test chamber can be corrected similarly using the residual distribution.

The third step is the correction of the rotation around the z-axis, for which the two dimensions x and y are used. If the detector is not rotated around the z-axis, the residual distributions in y versus the x-coordinate of the cluster and the residual in x (Δx) versus the y-coordinate of the cluster should have a slope equal to zero. If the slope is not equal to zero, the correction α for the rotation

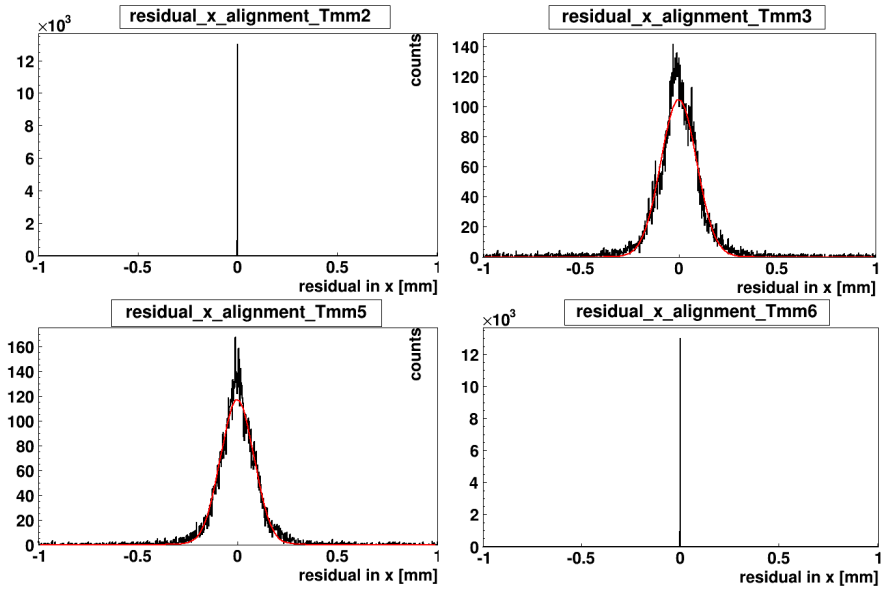

Figure 5.8: Residual distributions for the telescope detectors after step 2. Two distributions are exactly zero, because only these two detectors were used for the track fit.

can be calculated with the slope a (see figure 5.9 left):

$$\tan\alpha = a = \frac{\Delta x}{y}$$

After that correction the slope in figure 5.9 (right) is zero. Now, a second iteration of the position alignment is necessary, because the rotational corrections can shift the detectors again. All detectors are thus shifted by the mean of the respective residual distribution until it is zero. After this correction, the telescope and the L1 chambers are reasonable well aligned. This rotational correction could not be made for the scans along the strip at the edges of the test detector, because of the missing information of the position perpendicular to the strips of the L1 chamber.

5.1.4 Determination of the Track Accuracy

The spatial resolution of a detector can be extracted from the standard deviation of the residual distribution. The width of the residual distribution σ_r, is given by the quadratic sum of the intrinsic spatial resolution σ_sr and the track accuracy σ_track [Carnegie et al., 2005]:

$$\sigma_\mathrm{r} = \sqrt{\sigma_\mathrm{sr}^2 + \sigma_\mathrm{track}^2}\ . \tag{5.3}$$

To calculate the spatial resolution for the test chamber (L1) obviously the track accuracy is needed. The track accuracy can be calculated from the spatial resolution of the reference detectors, determined with the method suggested by Carnegie. For each detector two values will be determined for the standard deviations of the

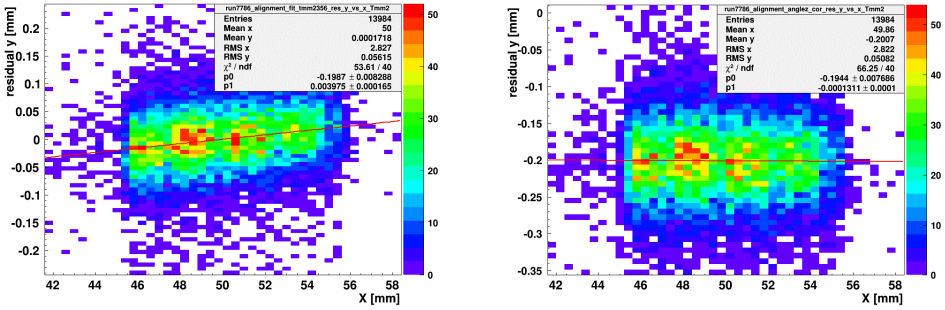

Figure 5.9: Distribution residual y versus x before correction (left) and after correction (right).

residual distribution, one with all detectors in the fit included $\sigma_{\mathrm{i,included}}$ and one with the detector to be studied excluded $\sigma_{\mathrm{i,excluded}}$. To estimate the spatial resolution, the geometrical average of these two standard deviation is calculated:

$$\sigma_{\mathrm{i}} = \sqrt{\sigma_{\mathrm{i,included}} \cdot \sigma_{\mathrm{i,excluded}}} \ , \tag{5.4}$$

with its error $\Delta\sigma_{\mathrm{i}}$:

$$\Delta\sigma_{\mathrm{i}} = \frac{1}{2\sigma_{\mathrm{i}}} \sqrt{(\sigma_{\mathrm{i,included}} \cdot \Delta\sigma_{\mathrm{i,excluded}})^2 + (\sigma_{\mathrm{i,excluded}} \cdot \Delta\sigma_{\mathrm{i,included}})^2} \ , \tag{5.5}$$

where i stands for the reference detectors. This is done for each separately.

To get the values for the standard deviation, the residual distribution is fitted with two Gaussian functions (see Eq. (5.6)), this is shown in figure 5.10. The two Gaussian functions are chosen because of the δ-electrons, which are produced in some of the events, they lead to the tails in the residual distribution.

$$f(x) = A_1 \exp(-\frac{(x-\mu_1)^2}{2\sigma_1^2}) + A_2 \exp(-\frac{(x-\mu_2)^2}{2\sigma_2^2}) \ , \tag{5.6}$$

where A_{k} are the amplitudes, μ_{k} the means and σ_{k} the standard deviations of the two Gaussian functions with $\mathrm{k} = 1$ for the narrow one and $\mathrm{k} = 2$ for the broad one.

Because of the fit with two Gaussian functions and the chosen range, the ratio of the entries in the narrow and in the broad Gaussian function has to be taken in account for the error $\Delta\sigma_{\mathrm{fit}}$ of the standard deviation. That can be done by the integrals of the two functions, which are given by:

$$I_{\mathrm{i}} = \int_{-\infty}^{\infty} A_{\mathrm{i}} \exp(-\frac{(x-\mu_{\mathrm{i}})^2}{2\sigma_{\mathrm{i}}^2}) = \sqrt{\frac{2}{\pi}} A_{\mathrm{i}} \sigma_{\mathrm{i}} \tag{5.7}$$

The ratio $R = I_2 \cdot I_1$ was for every fit between 15 % and 20 %.

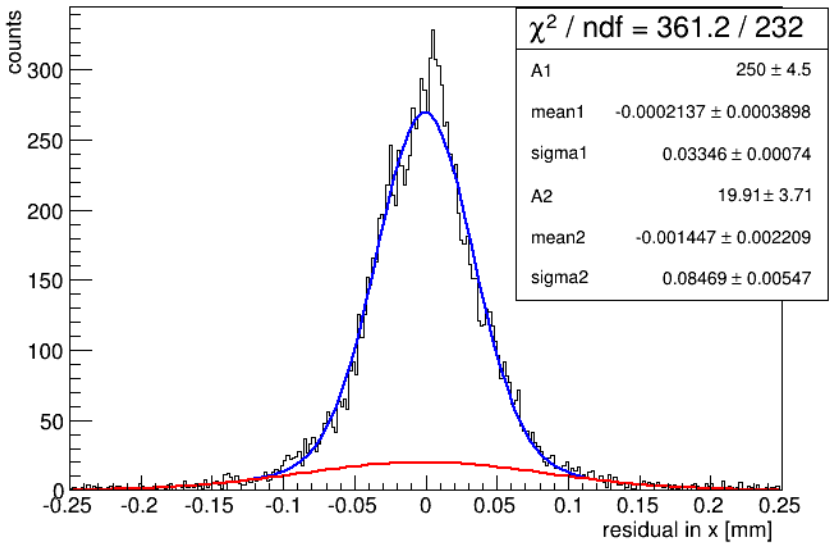

Figure 5.10: Residual distributions fitted with two Gaussian functions.

The spatial resolutions for each detector and run are filled in histograms (see figure 5.11). And the arithmetic average for the spatial resolution and for its error is calculated by:

$$\overline{\sigma_i} = \frac{1}{N}\sum_{j=1}^{N}\sigma_{i,j} \qquad \text{and} \qquad \overline{\Delta\sigma_i} = \frac{1}{N}\sum_{j=1}^{N}\Delta\sigma_{i,j}\ , \tag{5.8}$$

where N is the number of runs being different for each of the three scans along the strips of the L1 chamber.

The calculation of the track accuracy σ_{track} as a function of the test chamber's position z_{L1} is done starting from the analytic χ^2-minimization by: [Horvat, 2005, p. 195].

$$\sigma_{\text{track}}(z_{\text{L1}}) = \sqrt{\frac{\Lambda_{22} - 2z_{\text{L1}}\Lambda_{12} + z_{\text{L1}}^2\Lambda_{11}}{\Lambda_{11}\Lambda_{22} - \Lambda_{12}^2}}\ , \tag{5.9}$$

with its error

$$\begin{aligned}\Delta\sigma =& \sqrt{\sum_{i=1}^{n}\left(\frac{\partial\sigma}{\partial\overline{\sigma_i}^3}\overline{\Delta\sigma_i}\right)^2} \\ =& \sqrt{\sum_{i=1}^{n}\left(\frac{1}{\sigma\overline{\sigma_i}^3 D}\left(\sigma^2\left(\Lambda_{22} + \Lambda_{11}z_i^2 - 2\Lambda_{12}z_i\right) - \left(z_i - z_{\text{L1}}\right)^2\right)\overline{\Delta\sigma_i}\right)^2}\ .\end{aligned} \tag{5.10}$$

where n is the number of detectors used for the track reconstruction and σ means $\sigma_{\text{track}}(z_{\text{L1}})$. Λ_{11}, Λ_{12}, Λ_{22} and D are given in (4.7) in section.

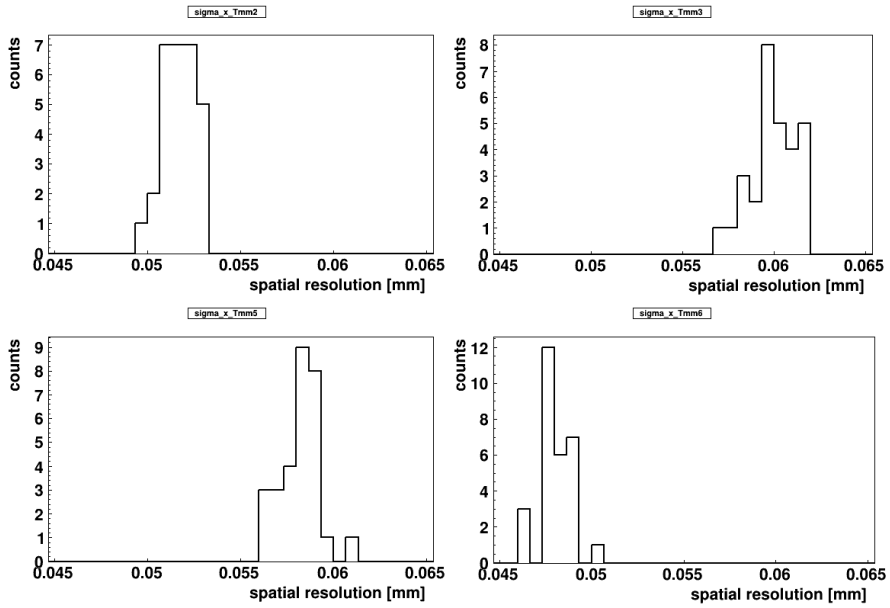

Figure 5.11: Spatial resolution for the four reference detectors, one entry for each run of the scan in the middle of L1.

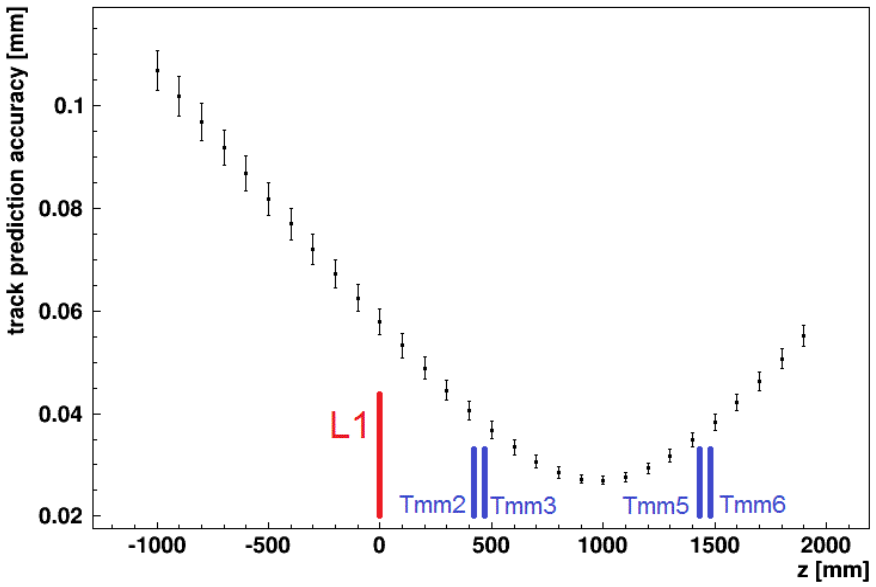

Figure 5.12: Track prediction accuracy as a function of the distance to the telescope. The positions of the reference chambers and the test chamber are marked with blue and red lines, respectively.

The track prediction accuracy as a function of the distance from the telescope is plotted in figure 5.12. The best value for the track accuracy would be inside the reference telescope. For the actual position $z_{\mathrm{L1}} = 0$ it yields the result for the scan in the middle:

$$\sigma_{\mathrm{track,x}} = (57.8 \pm 2.5)\,\mu\mathrm{m}\ . \tag{5.11}$$

The same analysis was made for the y-direction, which leads to the result

$$\sigma_{\mathrm{track,y}} = (61.5 \pm 2.8)\,\mu\mathrm{m}\ . \tag{5.12}$$

The latter will not be used in this analysis, since the test chamber has only one dimensional readout. For the scans along the strips on the edges the track accuracy was also determined, which yields the result:

$$\begin{aligned} \sigma_{\mathrm{track,x}} &= (63.3 \pm 3.3)\,\mu\mathrm{m} \text{ for the left side } \textit{and} \\ \sigma_{\mathrm{track,x}} &= (63.0 \pm 3.4)\,\mu\mathrm{m} \text{ for the right side}\ . \end{aligned} \tag{5.13}$$

Due to the absence of the readout electronics for the strips in x-direction the corrections of the rotation around the z-axis could not be made. So the reference detectors are not totally aligned and the track accuracy gets worse. In section 6.1.1 is shown, that this has an effect on the spatial resolution.

5.2 Measurement with Cosmic Muons

To investigate the signal timing of the large Micromegas chamber a measurement with cosmic muons was performed. Eight scintillators, four above and four below the Micromegas, trigger on crossing muons. The scintillator data was read out to get exact timing information on the trigger.

5.2.1 Experimental Setup

Four pairs of trigger scintillators were located along the strips of the horizontally oriented test chamber (see figure 5.13 and 5.14). For each pair one scintillator is above and one below the detector to trigger coincident on muons. The trigger signal is also used to eliminate the jitter from the APV25 readout, which is read out with the FEC standalone system. With a TDC[1] the scintillators were read out. It was thus possible to register which scintillator was hit and also to determine the asychronous scintillator timing with respect to the synchronous SRS trigger signal as the TDC was stopped with the synchronous signal from the FEC card. The VME[2] data stream and the SRS data stream have to be merged in order to correlate the TDC information with the strip information from the APV25s. This is done with a 12-bit counter [Bortfeldt et al., 2013]. The counter gives the number of the event as 12-bit digit to both data streams, so this number can be checked

[1] Time to Digital Converter
[2] Versa Module Eurocard

in the analysis. In this measurement only one run with about 100000 events was taken.

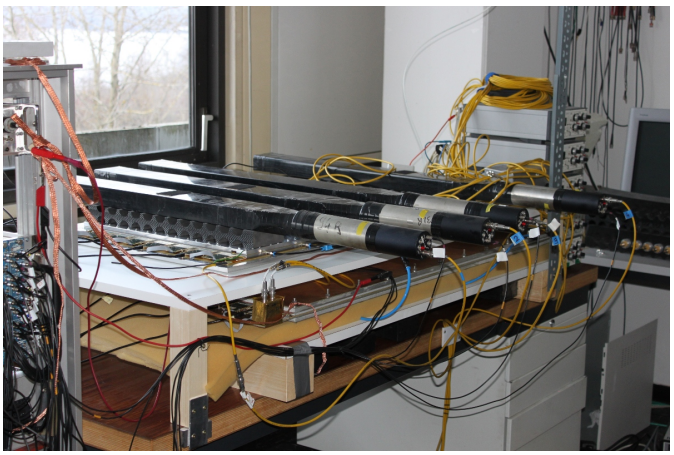

Figure 5.13: Picture of the experimental setup.

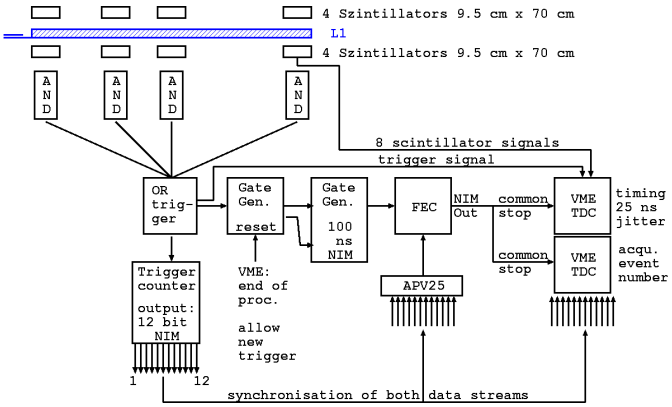

Figure 5.14: Logic scheme of the experimental setup

5.3 Cosmic-Ray Facility

The Max-Planck Institute for Physics has built together with LMU Munich 88 BOS[3] MDT chambers for the barrel of the ATLAS muon spectrometer. The Cosmic-Ray Facility (CRF) was developed by LMU Munich for quality control and calibration of the MDT chambers. To make exact measurements with the MDT chambers the exact wire positions inside the tubes have to be known. The CRF has two reference chambers consisting of six tube layers. Between the upper (MDT1) and the lower (MDT2) reference chamber the test chamber is installed, which shall be investigated.

The reference chambers were calibrated in a X-ray tomograph, so the wire positions are well known.

[3]Barrel Outer Small

Both MDT chambers consist of two multilayers, which have three layers with 72 tubes glued together. Each tube is 4 m long and has a diameter of 3 cm. So the total active area is about 8 m^2. With these chambers the track of the muon going through the setup can be reliably measured. The tracks in MDT1 and MDT2 can be extrapolated or combined to get a hit prediction for the test chamber. The muon track angle ranges between about -30° and 30°.

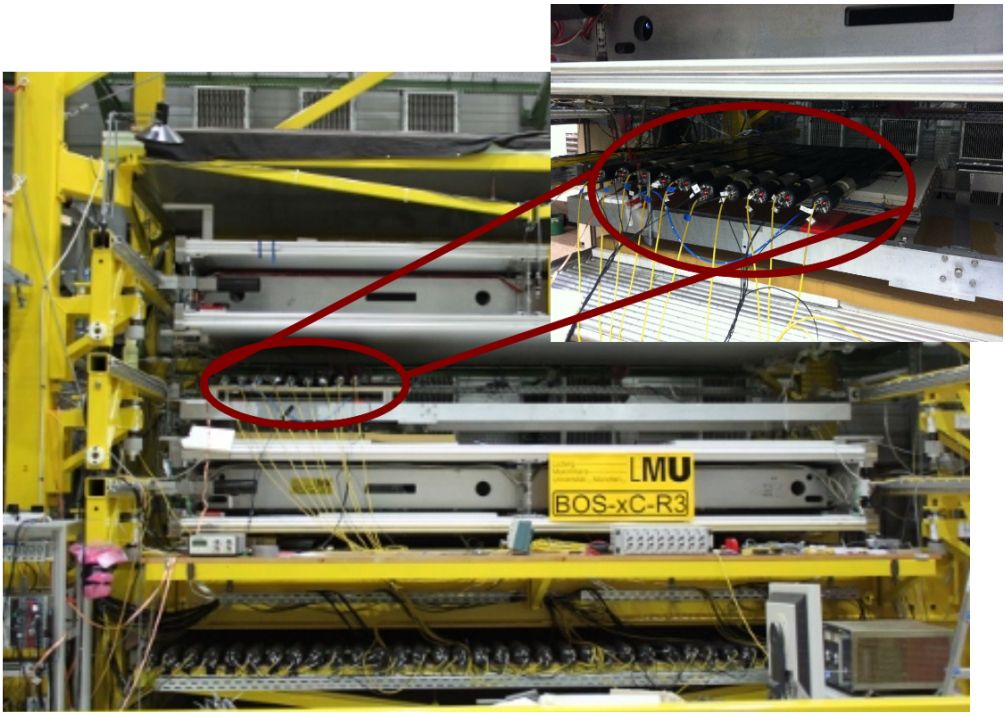

Figure 5.15: Photo of the experimental setup of the CRF (left) and the test chamber in the CRF with the additional trigger scintillators on top of it (right).

5.3.1 Experimental Setup

Figure 5.15 shows a photo of the experimental setup and figure 5.16 a schematic drawing of it. For this measurement only the reference chambers and the two scintillator layers, also called hodoscope of the CRF are used. The hodoscopes are oriented perpendicularly to the drift tubes and give a hit information along the anode wires. Above the reference chambers the upper hodoscope is installed consisting of 42 9 cm wide scintillation counter. The two layers of the lower hodoscope, consisting of 38 scintillators each, with a width of 10 cm, have their readout on opposite sides and overlap by half their width. So the average over the timing of the scintillator gives the event time. Between the lower hodoscope and the lower reference chamber a 34 cm thick iron absorber is installed to harden the muon spectrum and as a consequence to reduce multiple scattering in the reference and in the test chambers. All muons with not at least an energy of 600 MeV are absorbed in the iron. Underneath the lower hodoscope streamer tubes are installed, with a spatial resolution of about 1 cm, to measure the muons scattering angle

from interaction within the iron absorber. But these streamer tubes were not used in this measurement. [Dubbert et al., 2002]

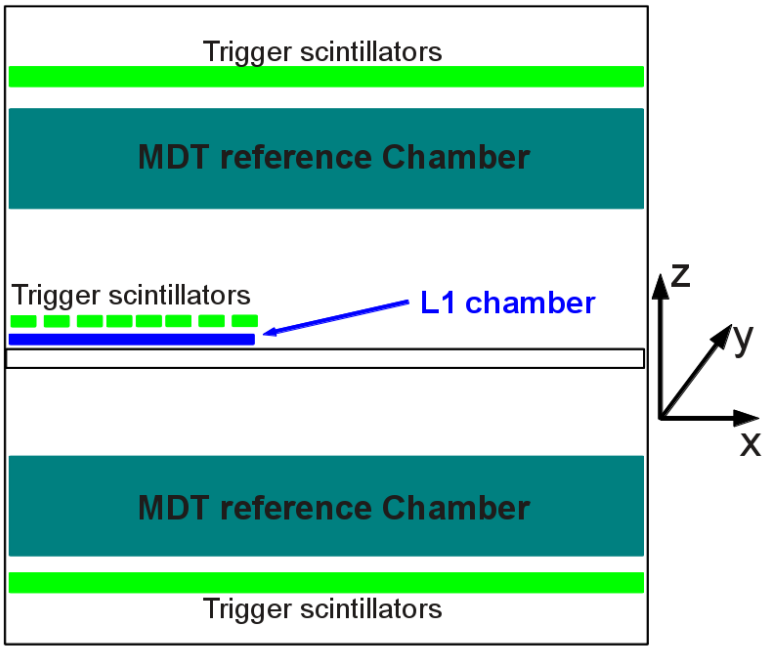

Figure 5.16: Schematic setup of the measurement.

Instead of a MDT test chamber the L1 Micromegas chamber is installed between the reference chambers. On top of the Micromegas eleven additional 9.5 cm wide scintillators, which are perpendicular to the strips, allow to trigger only on muons, that have crossed the active area of the Micromegas.

The Micromegas detector was read out with SRS and the MDT chambers with an ATLAS readout system especially modified for the CRF. Additionally to the CRF's standard readout system, which is described in [Rauscher, 2005], it is recorded, which scintillator, lying on top of the micromegas, has been hit. To merge these two data streams, an event number was recorded by both streams. One long run over about five days were taken. Muon tracks that could not be used for the analysis were excluded, afterward 6.7M evernts remained. Some short runs with about 20000 events were taken for the optimization of the operational parameters

5.3.2 Optimization of the Micromegas Operational Parameters

To determine the working point of the test chamber several high voltage scans were performed. Runs were taken with different voltages, the leading cluster charge distributions were fitted with a Landau function and the most probable values were plotted versus the electrical field strength.

Figure 5.17 shows the pulse height as a function of the amplification field between mesh and resistive anode strips. The drift voltage was fixed at $U_{\text{drift}} = -150\,\text{V}$. If the amplification voltage becomes to high, the rate of discharges between the mesh and the strips increases significantly. So as compromise between a sufficiently high pulse height and acceptably low spark rate it was decided to use $U_{\text{ampl}} = 570\,\text{V}$ for the amplification voltage, which corresponds to an electric field of $E \approx 44.5\,\text{kV/cm}$.

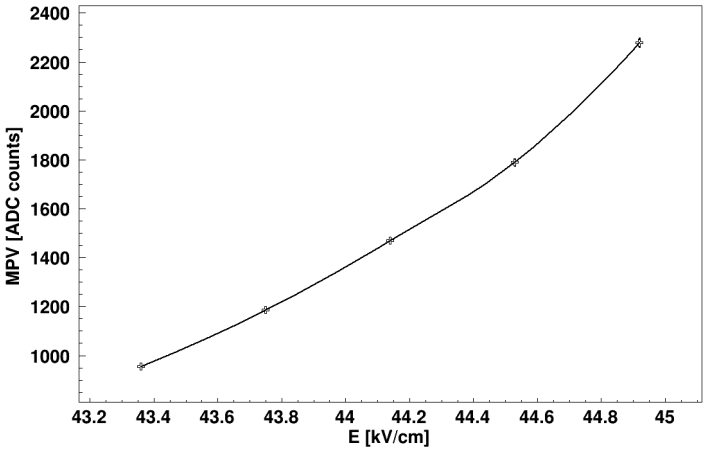

Figure 5.17: Scan of the amplification voltage, most probable value of leading cluster distribution versus electric amplification field.

With this fixed amplification voltage the variation of the pulse height as a function of the drift voltage was measured (see figure 5.18). The maximum pulse height is reached at $U_{\text{drift}} = -175\,\text{V}$, so this value has been chosen for the drift voltage.

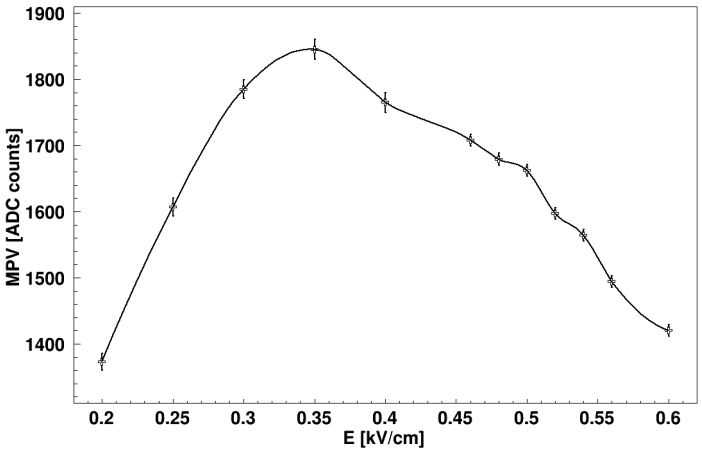

Figure 5.18: Scan of the drift voltage, most probable value of leading cluster distribution versus electric drift field.

5.3.3 Event Selection

The event selection for the reference chambers is discussed in [Rauscher, 2005]. In the lower hodoscope two hits in two overlapping scintillators are required and one hit in the upper hodoscope.

For the following analysis only events were used, in which the tracks measured in the two reference chambers are similar. The central part of the distribution of the difference between the slopes (see figure 5.19 left) was fitted with a Gaussian function. All events outside the range of 1σ around the mean value were excluded. The distribution of the difference between the intercepts (see figure 5.19 right) was fitted with two Gauss functions overlaid. And again all events outside the range of 1σ of the slimmer Gauss function around the mean value were excluded.

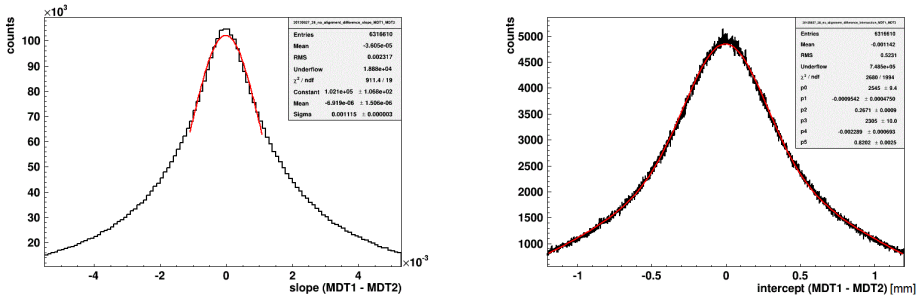

Figure 5.19: Distribution of the difference between the track slopes (left) and intercepts (right) of the tracklets from MDT1 and MDT2, fitted with Gaussian functions.

All events in which not exactly one of the additional eleven scintillators has seen a signal were excluded, too.

5.3.4 Alignment

The positions of the reference chambers are already well aligned. The L1 chamber has to be aligned to the coordinate system of the reference chambers. It can be rotated around all three axes and shifted in three directions as well.

The correction of the shift in x- and y-direction works as described in section 5.1.3, the chamber has to be shifted into the respective direction until the mean value of the residual distribution is zero. For perpendicular tracks is no shift in the z-direction, so these are used for this correction.

For the shift in the z-direction it is a little bit more complicated. Therefore the Micromegas chamber can easily be split into rectangles of $57.6 \times 97.7\,\mathrm{mm}^2$, where one side is defined by the 128 strips connected to a specific APV25 and the other by the width of a trigger scintillator. So the x-position of these rectangles is given by the scintillator ID and the y-position by the APV ID. Thus it is also possible to investigate the internal deformation of the chamber.

In figure 5.20 the muon track, the actual and the assumed position are shown. α is given by the MDT chambers with the slope m_y of the track

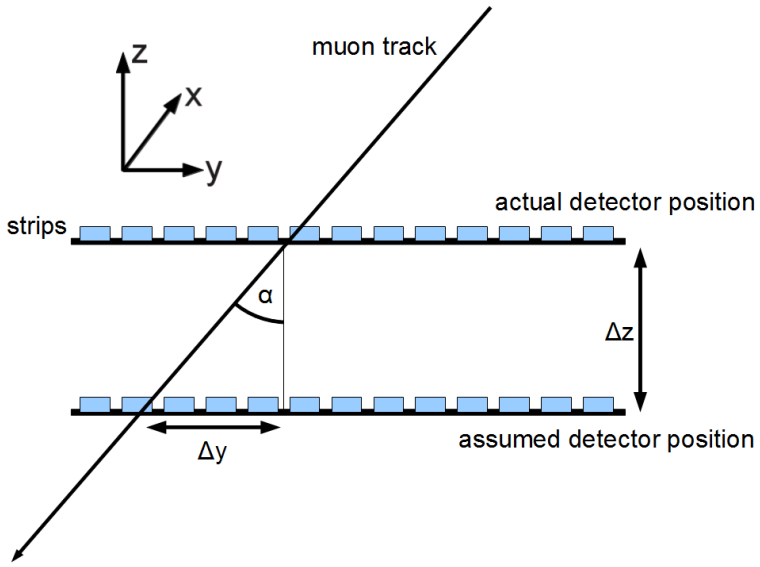

Figure 5.20: Schematic picture of the muon track through the Micromegas detector for the determination of the detector position correction Δz.

$$\alpha = \arctan m_{\mathrm{y}}$$

with index y only for the y-direction. To get the correction

$$\Delta z = \frac{\Delta y}{\tan \alpha} = \frac{\Delta y}{m_{\mathrm{y}}} \tag{5.14}$$

for the detector position, the values of the residual Δy versus m_{y} are filled in a histogram for each event, separately for all detector segments. Figure 5.21 shows this as an example for one segment of the detector. The distribution is fitted with a straight line. The slope of that line corresponds to Δz and the intercept with the y-axis is Δy as can be easily seen from (5.14).

Δz and Δy are calculated for all the detector segments and filled in 3D histograms as a function of APV and scintillator ID. In figure 5.22 the detector position in the MDT space is shown before the alignment. With the variation of the Δz values along the APV IDs and scintillator IDs, respectively, the rotation around the y- and the x-axis can be corrected. If there are no more variations along the APV and scintillator IDs, overall shift in z-direction can be corrected. And in figure 5.23 the shift in y-direction for all the parts is shown. The non-vanishing slope along the scintillator ID-axis is due to a rotation around the z-axis and can be used to correct for this. Furthermore, there is a gap between APV 7 and APV 8. The test chamber consists of two boards, which are glued together between APV 7 and APV 8. So APV 0 with 7 and APV 8 with 15 have to be corrected separately.

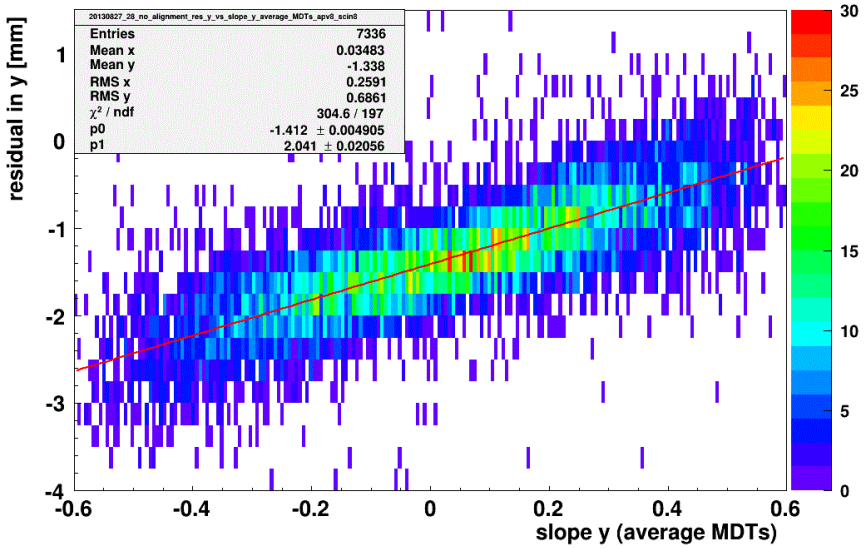

Figure 5.21: Distribution of the residual versus the muon track slope, fitted with a straight line.

Figure 5.24 and 5.25 show again the deviation in z and the deviation in y versus APV and scintillator ID, but after the corrections. Due to low statistics in some detector segments there is a larger variance of the results. Since the detector is only mounted on its edges, it is not totally flat, as can be seen also in figure 5.24. Additionally, the inflation of the detector, caused by the slight overpressure of the gas mixture inside the detector is also visible.

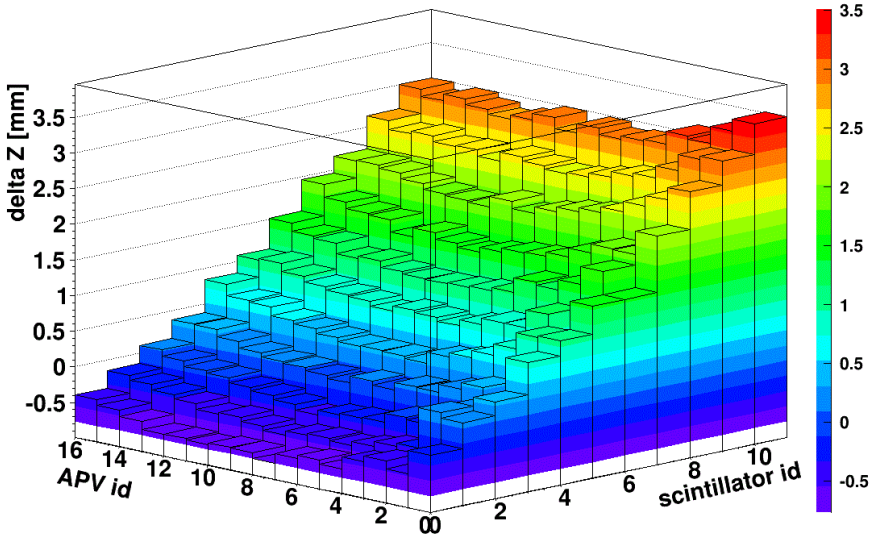

Figure 5.22: Δz versus APV ID and scintillator ID before the corrections. The detector lies not horizonlat and the rotation around the x axis has to be corrected.

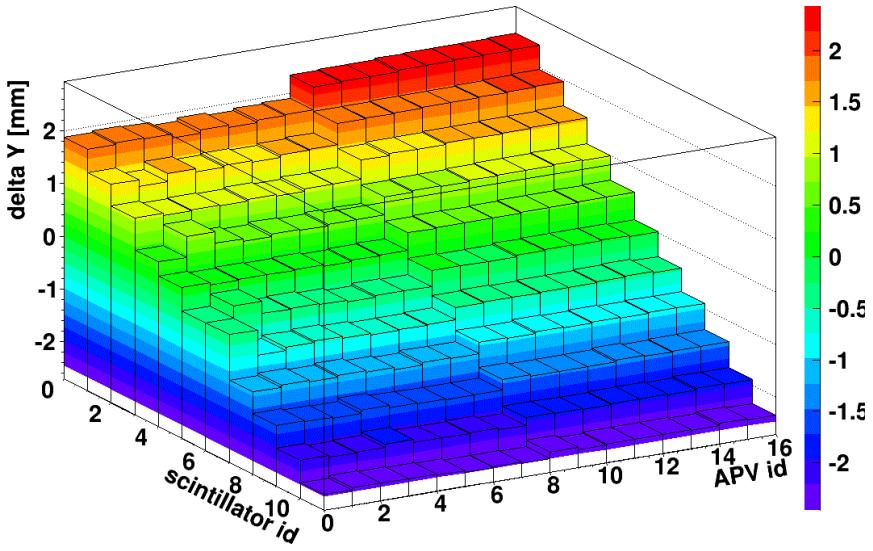

Figure 5.23: Δy versus APV ID and scintillator ID before the corrections. The rotation around the z axis and the shift between the two PCB boards can be seen.

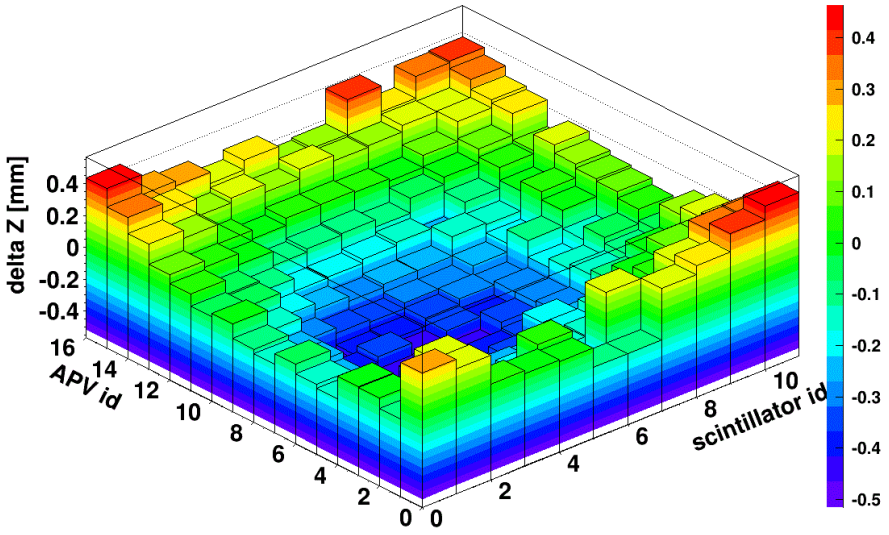

Figure 5.24: Δz versus APV ID and scintillator ID after the corrections. The inflation due to the small overpressure can be seen.

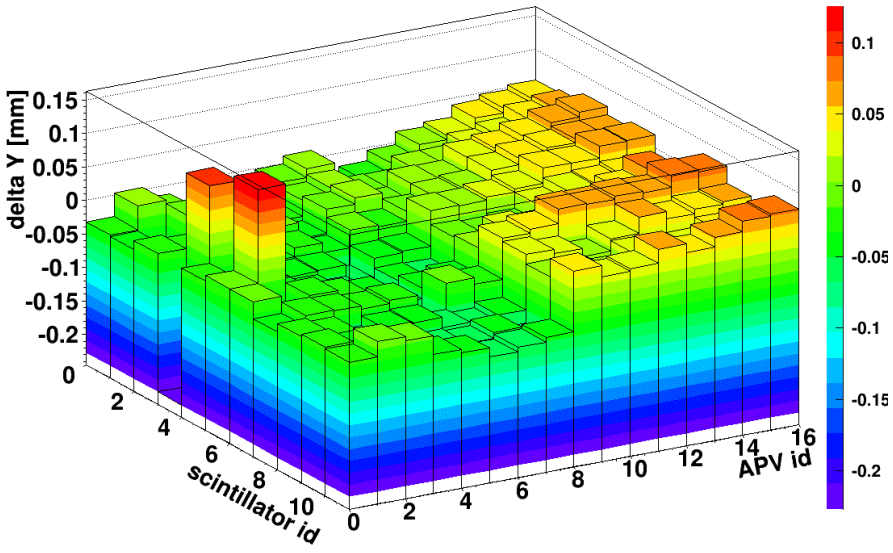

Figure 5.25: Δy versus APV ID and scintillator ID after the corrections. In the shift in the y-direction are still differences up to about 100 μm.

6 Results

In the following chapter the results for spatial and angular resolution, signal timing and efficiency in the large L1 Micromegas chamber for the three measurement campaigns are presented.

6.1 Spatial Resolution

One of the essential properties of a Micromegas chamber is the spatial resolution. It is important to have a good spatial resolution for track determination and momentum measurements in magnetic fields. The results for the spatial resolution of the L1 chamber are discussed in the following sections. The spatial resolution for 120 GeV pions and cosmic muons, measured with the centroid method (see sction 4.2) as well as with the μTPC-method for tracks, not perpendicular to the detector, introduced in section 4.4, will be presented.

6.1.1 Pion Testbeam at SPS/CERN

The spatial resolution for the four measurements in the pion testbeam, discussed in section 5.1, was determined. Primarily the scan along the strips in the middle of the detector is presented. First the standard deviation σ_{L1} of the residual distribution of the test chamber, where all reference detectors are used in the track fit, is determined. The residual is the difference between the predicted hit position and the measured hit position in the L1 chamber, as described in section 5.1.3. Now, the spatial resolution σ_{sr} for the L1 detector can be calculated:

$$\sigma_{\mathrm{sr}} = \sqrt{\sigma_{\mathrm{L1}}^2 - \sigma_{\mathrm{track}}^2}\ , \tag{6.1}$$

where σ_{track} is the track accuracy.

As the uncertainties for σ_{L1} the fitting error is used. This error, $\Delta\sigma_{\mathrm{L1}}$, and the error of the track accuracy $\Delta\sigma_{\mathrm{track}}$ yields the error of the spatial resolution:

$$\Delta\sigma_{\mathrm{sr}} = \frac{1}{\sigma_{\mathrm{sr}}}\sqrt{(\sigma_{\mathrm{L1}} \cdot \Delta\sigma_{\mathrm{L1}})^2 + (\sigma_{\mathrm{track}} \cdot \Delta\sigma_{\mathrm{track}})^2} \tag{6.2}$$

The spatial resolution was calculated for all beam positions in the scan and plotted in figure 6.1 versus the y position. Because of the movable table, on which the detector stood, the adjustment position is used as y position. So the scan along the strips has an offset of about 25 cm, i.e. in figure 6.1 position 250 mm is where the strips ended on the readout side.

It can be seen that the spatial resolution in the detector is quite homogeneous. Averaging over these values leads to a mean spatial resolution:

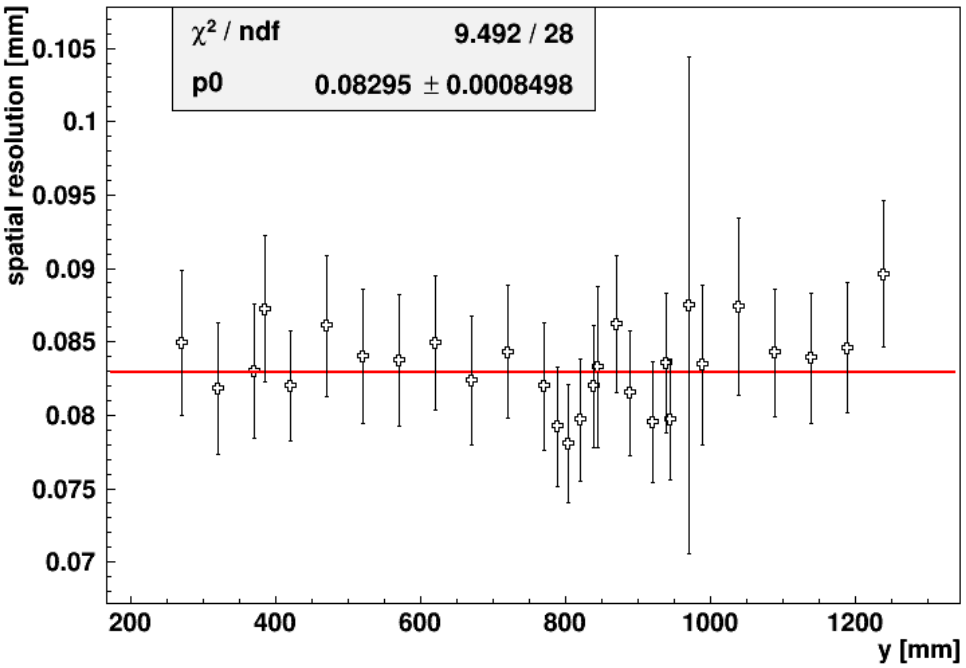

Figure 6.1: Spatial resolution versus position of the beam spot along the strips of the Micromegas for a scan in the middle of the chamber.

$$\overline{\sigma_{\mathrm{sr}}} = (83.0 \pm 0.9)\,\mu\mathrm{m}\ . \tag{6.3}$$

The same procedure was repeated for the scan along the strips on the left and the right side of the detector. In figure 6.2 the spatial resolutions are plotted. The blue markers represent the resolution for the scan on the left side (connector 1 and 2) and the red markers for the right side (connector 15 and 16) (see figure 5.3).

The spatial resolution is homogeneous within the scans, but on the edges of the detector by 20 % worse than for the scan in the middle. The track accuracy for these scans were worse than for the middle, because of the not possible correction of the rotations of the reference detectors, but this is only a 10 % effect. Where the other 10 % come from has to be studied.

Additional to the scan along the strips there were runs taken with a rotation of the L1 chamber. The detector was rotated around the strip direction with the angles -10°, -20° and -30° with respect to the beam. For the runs with a rotated test chamber the residuals were determined as well. In figure 6.3 the spatial resolution as a function of the angle of incidence is plotted, the larger the angle of incidence the broader the residual distributions. Due to the energy loss fluctuations of the minimum ionizing particle along its path the centroid method for the determination of the cluster position does not work as well as for perpendicular tracks to the detector. Similar results are shown and discussed in [Bortfeldt et al., 2012].

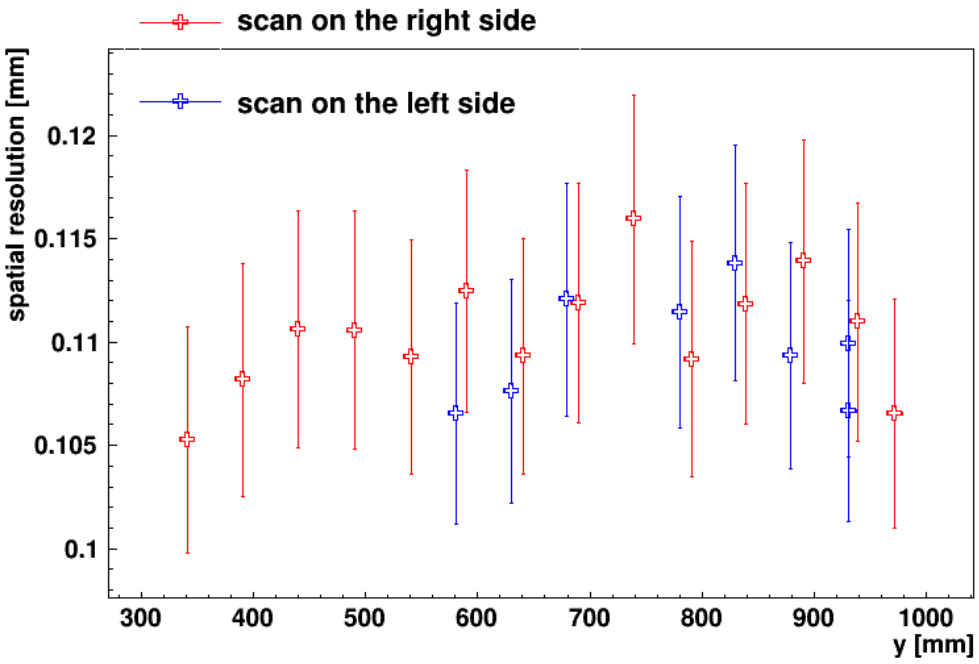

Figure 6.2: Spatial resolution versus position of the beam spot along the strips of the Micromegas. The blue markers refer to the scan on the left side, the red marker to the scan on the right side.

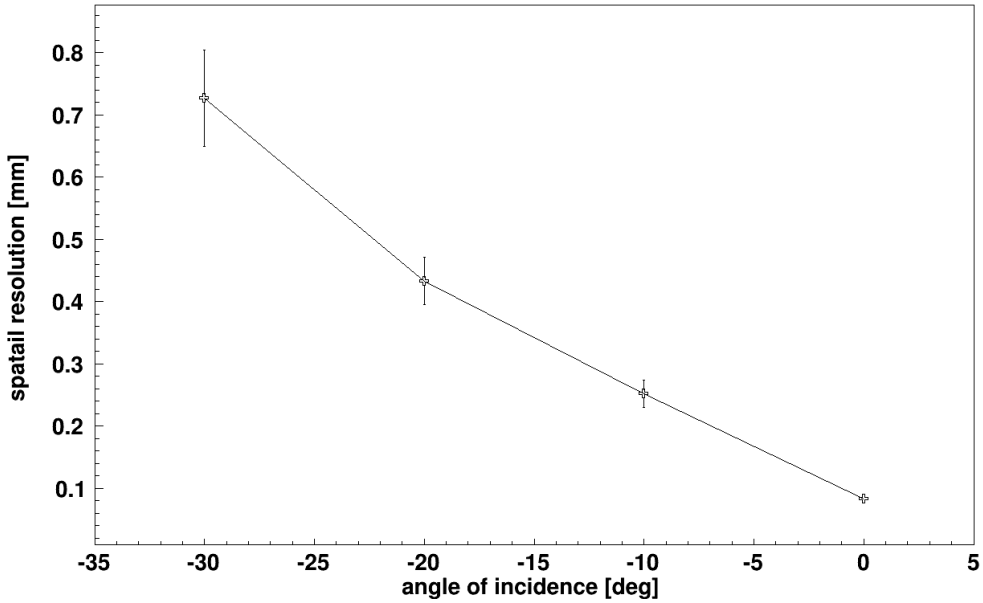

Figure 6.3: Spatial resolution for different angle of incidences in the test chamber.

6.1.2 Cosmic-Ray Facility

Because of the CRF's track accuracy around 40 μm the track of the triggered muons is almost precisely known. The hit predictions in the detector plane can be calculated with these tracks and compared to the hit positions in the test chamber. With cosmic muons the whole Micromegas detector can be investigated at once.

For the whole detector the residual in the y-direction is plotted for reference tracks with an inclination between $-1°$ and $1°$. This leads to the distribution shown in figure 6.4, which is fitted with two Gaussian functions. The standard deviation of the narrow Gaussian function gives the spatial resolution σ_{sr} of the L1 chamber and the broad Gaussian function is used again because of the δ-electrons. Thus we get for the spatial resolution of the L1 micromegas:

$$\sigma_{\mathrm{sr}} = (238.7 \pm 1.3)\,\mu\mathrm{m}$$

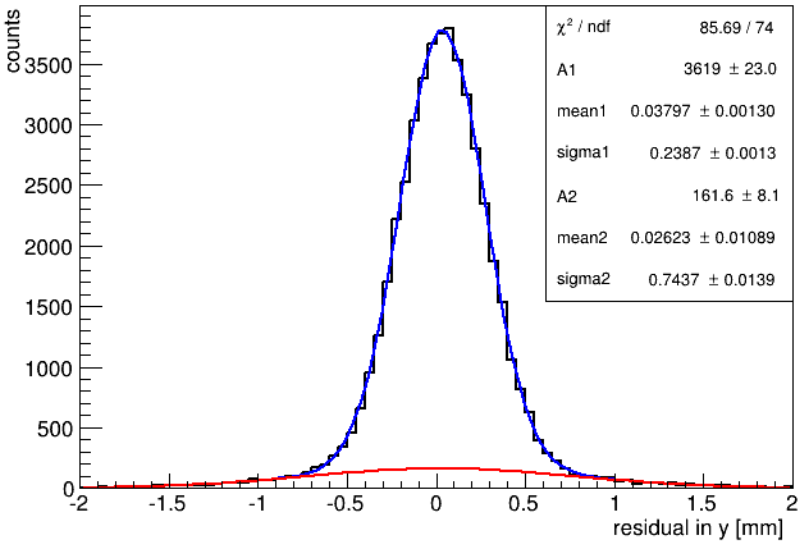

Figure 6.4: Residual distribution for reference track angle between $-1°$ and $1°$, fitted with two Gaussian functions.

The result for the spatial resolution is here about three times as broad as in the measurement at the testbeam with 120 GeV pions. One reason for that could be that the energy of the cosmic muons is lower than the energy of the pions, so the muons do more multiple scattering than the pions. Another possible reason for the deviation is that the measurement here was taken over five days, so during that time the test detector and the reference chambers have moved because of the temperature variation. This movement has, due to the lack of alignment sensors on the Micromegas chamber, not been corrected for. The runs at the pion testbeam took only 20 minutes. The mean value of the residual distribution versus the time is plotted in figure 6.5. The upper figure is for the Micromegas and the lower is the mean residual between both reference chambers. Because

of the larger area of the MDT chambers, the variation of the mean value of the residual distribution for the MDT chambers should be bigger, but it seems like the variation for the Micromegas detector is bigger. The movement of the MDT chambers with the temperature variations could influence the track prediction and the spatial resolution could seem worse than it is.

These effects do not describe the total effect. It is not understood and has to be investigated further. How the temperature dependence and the cuts on the MDT track influences the residual distribution, has to be studied.

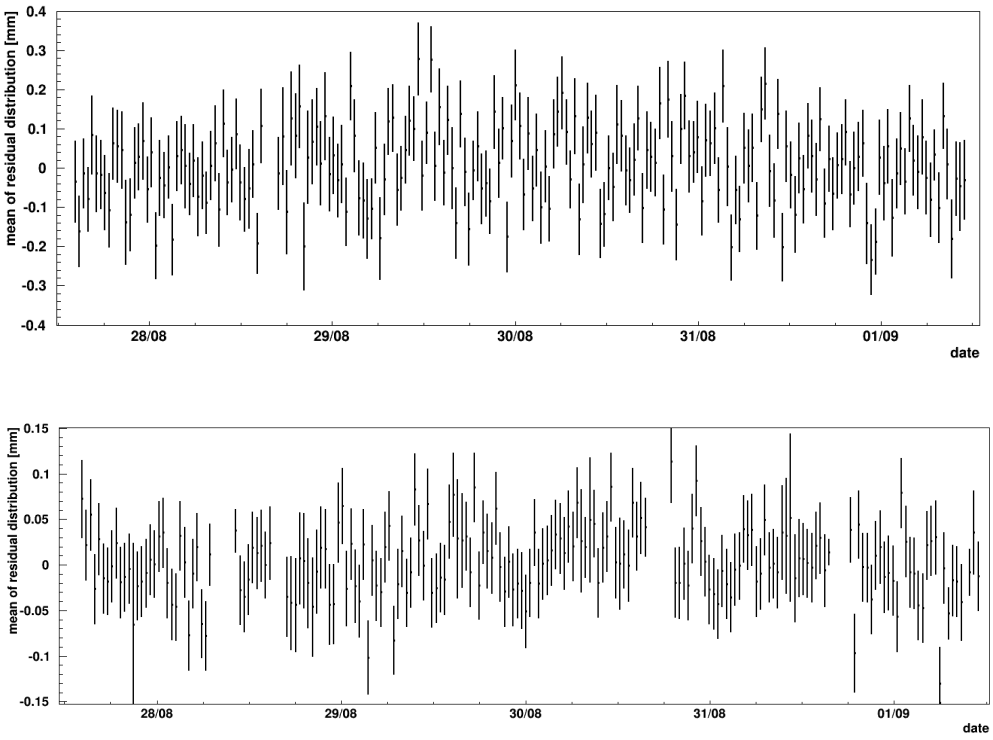

Figure 6.5: Mean of the residual distribution versus time for the Micromegas detector (upper) and for the residual of the two MDT chambers (lower). The variation in the upper figure is about three times larger than in the lower.

Figure 6.6 shows the spatial resolution as a function of the track angle predicted by the MDT chambers. The larger the track angle becomes the larger the spatial resolution is, up to about 600 μm for a track angle of 30°.

It is also possible to calculate the spatial resolution via the μTPC method introduced in section 4.4. Therefore the fitted straight line in the time-strip number-space is extrapolated to the readout plane (see section 6.4.2). Figure 6.7 shows the result for the spatial resolution as a function of the absolute value of the predicted track angle. This result is not as good as the result earlier presented. Although the spatial resolution might improve by excluding single strips from the uTPC-fit or using a more advanced data point weighting, the measured data presented here are in general of good quality, such that a large improvement is unlikely.

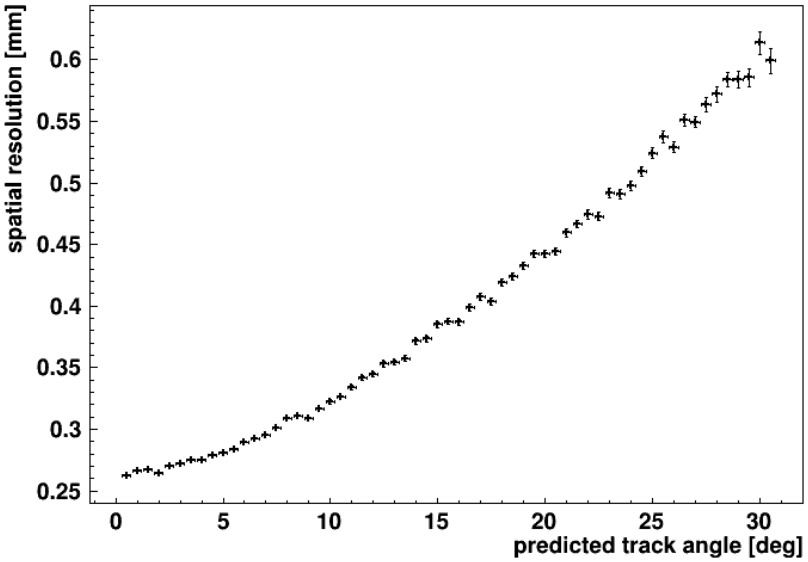

Figure 6.6: Spatial resolution as a function of the absolute value of the predicted track angle, calculated via the centroid method.

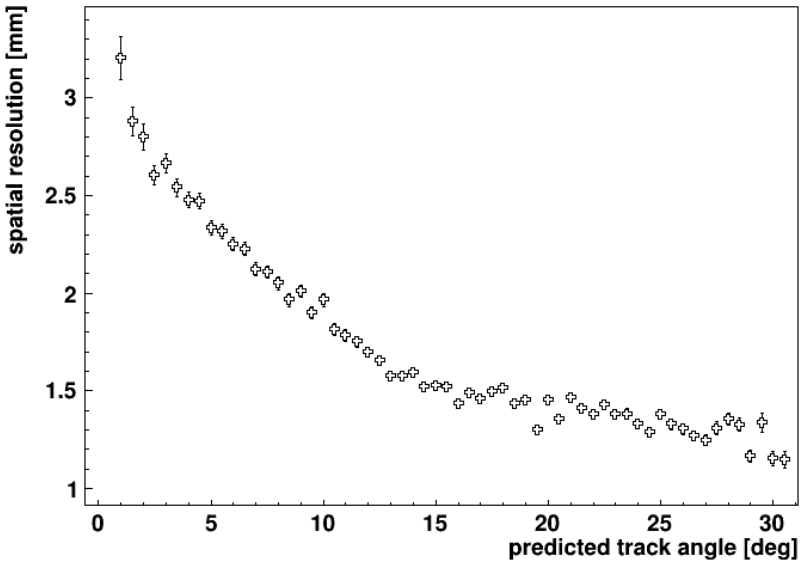

Figure 6.7: Spataial resolution as a function of the absolute value of the predicted track angle, calculated with the μTPC method

6.1.3 Discussion

The large Micromegas detector has shown an averaged spatial resolution of $\overline{\sigma_{\mathrm{sr}}} = (83.0 \pm 0.9)\,\mu$m in the scan along the strips with perpendicular incident 120 GeV pions. The scans along the strips on the edges of the test chamber did not show such a good result, because of the not as good track accuracy as for the scan in the middle of the detector. The measurement in the Cosmic-Ray Facility has shown only a spatial resolution $\sigma_{\mathrm{sr}} = (238.7 \pm 1.3)\,\mu$m for track angles between $-1°$ and $1°$. It is not jet understood, why this result is three times higher. It is probably due to the not optimized reference track reconstruction in this specific setup. The spatial resolution calculated with the centroid method is even for angles of 30 degrees smaller than the spatial resolution determined with the μTPC method. After some necessary improvements, the μTPC spatial resolution should show similar or better results than the centroid method.

6.2 Efficiency

Another important property of Micromegas detectors is their efficiency. They should see all minimum ionizing particles which cross their active area. In practice this is not possible due to the pillars on the readout plane, but a value close to 100 % can be reached. One possibility for inefficiencies are pillars between mesh and anode strips. The electrons created in the drift region cannot pass the pillars, so the electrons cannot be detected. To illustrate the effect of the pillars, in figure 6.8 the inefficiencies in the beam profile are shown for each reference detector in the testbeam telescope. The small spots in the distributions with more entries occur because of the pillars, which are periodically spaced by 2.5 mm with a diameter of 300 μm.

6.2.1 Pion Testbeam at SPS/CERN

The efficiencies are determined for all three scans along the strips.

To calculate the efficiency η for the test chamber L1 the number of events where all reference detectors and the test chamber have registered a hit, N_{all}, is divided by the number of events where all the reference detectors have seen a hit regardless of the test chamber, N_{ref}:

$$\eta = \frac{N_{\mathrm{all}}}{N_{\mathrm{ref}}} \tag{6.4}$$

with its statistical error

$$\Delta\eta = \sqrt{\frac{\eta\,(1-\eta)}{N_{\mathrm{ref}}}} \tag{6.5}$$

This is calculated for all runs in the three scans along the strips. The results are plotted for the scan in the middle of the detector in figure 6.9. During the measurement the detector had to be turn upside down to cover the whole length

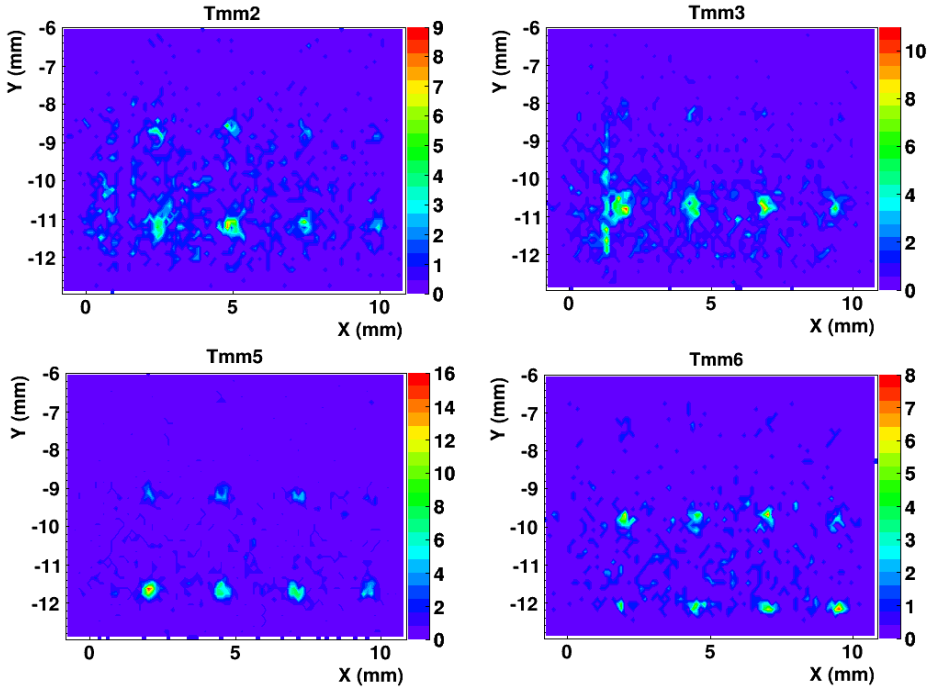

Figure 6.8: Inefficiencies in the beam profile for the reference detectors. The spots with more entries represent the pillars. Furthermore in Tmm3 a single dead strip is visible.

of the strips with this scan. The data points before and after the rotation have been drawn different colors, for better separation.

Figure 6.10 shows for comparison the pulse height for all runs in the scan. Again, the data taken before and after rotation have been drawn in different colors. A similar trend yields for the black markers the lower the cluster charge the lower efficiency. The efficiency after the rotation is in general high, although the charge is lower than before the rotation. But with in the green subsample, the correlation between efficiency and cluster charge seems to be similar. Figure 6.13 shows the efficiency as a function of the pulse height. A correlation can be seen, but divided in different groups. The data points in the scan before the rotation consists of two groups, clearly separated from the data points after the rotation also consisting of two groups.

A clear overall correlation is not visible. Throughout the scan the same voltages were used, so there have to be some mechanical deformations, which influence the width of the drift and amplification regions and thus influence the efficiency.

The results for the scans at the edges are shown in figure 6.11, where the blue markers represent the left scan and the red markers the right scan. The efficiencies and pulse heights do not have that large differences. For these scans no similar effect occur, no correlation can be seen (see figure 6.14). The differences between the edges and the middle of the detector have to be studied.

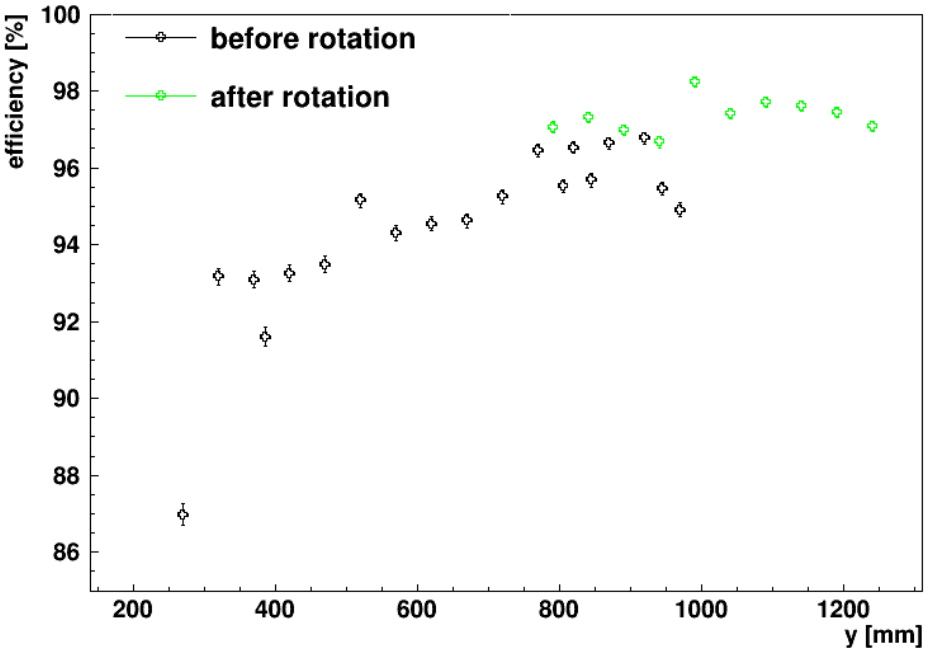

Figure 6.9: Efficiency versus position of the beam spot along the strips of the Micromegas for the scan in the middle of the chamber. The black markers represent the data points before the upside down rotation of the detector and the green markers the data points after the rotation of the detector.

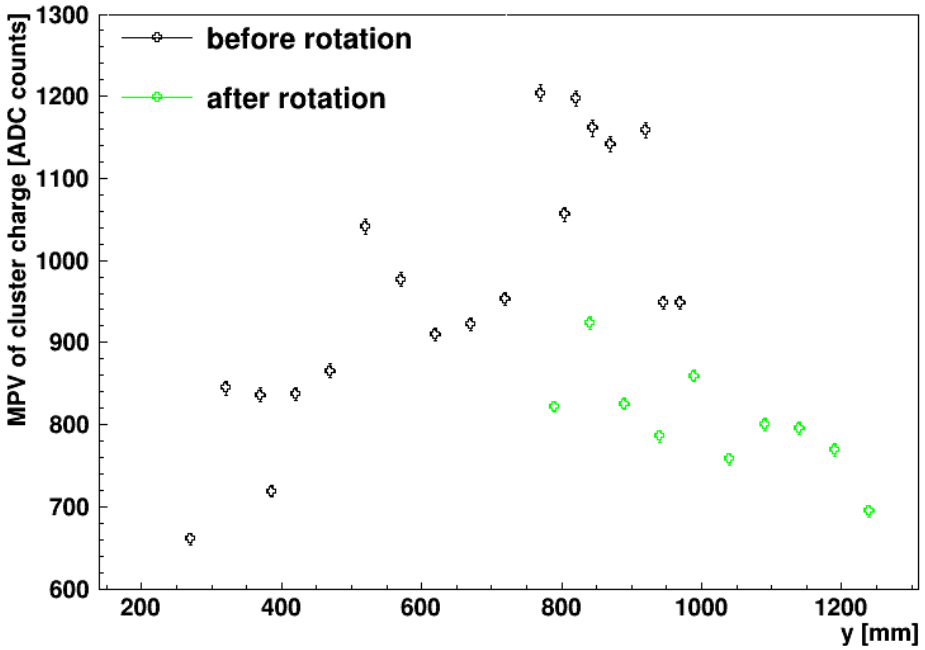

Figure 6.10: Most probable value of the charge distribution versus position of the beam spot along the strips of the Micromegas. The color coding is the same as in figure 6.9.

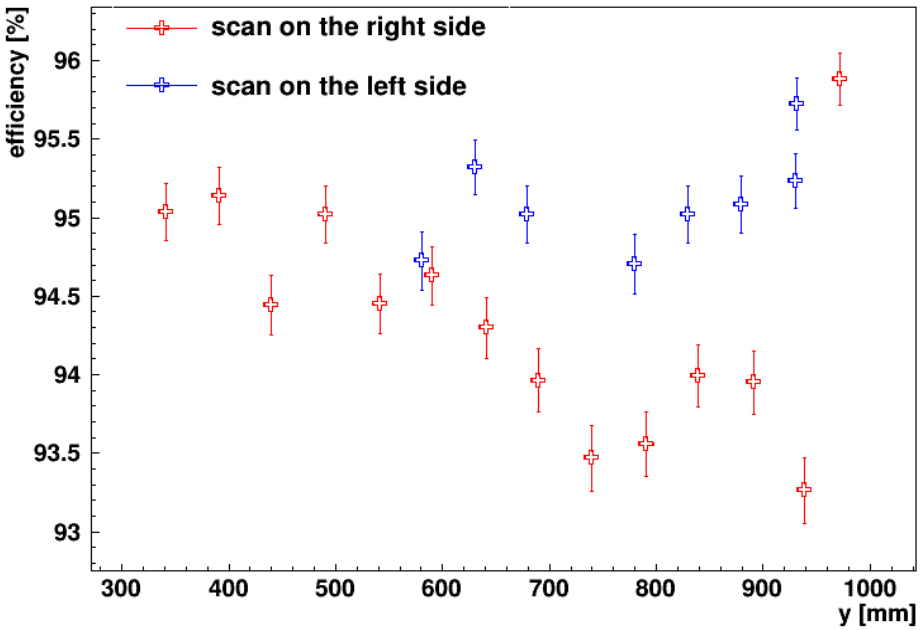

Figure 6.11: Efficiency versus position of the beam spot along the strips of the Micromegas. The blue markers represent the scan on the left side, the red marker the scan on the right side.

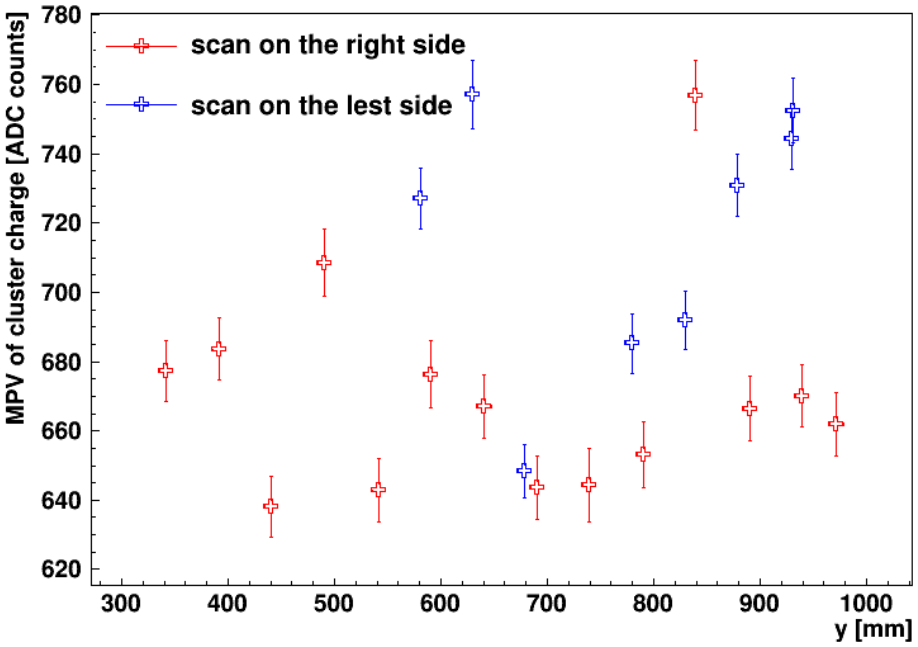

Figure 6.12: Most probable value of the charge distribution versus position of the beam spot along the strips of the Micromegas. The color coding is the same as in figure 6.11.

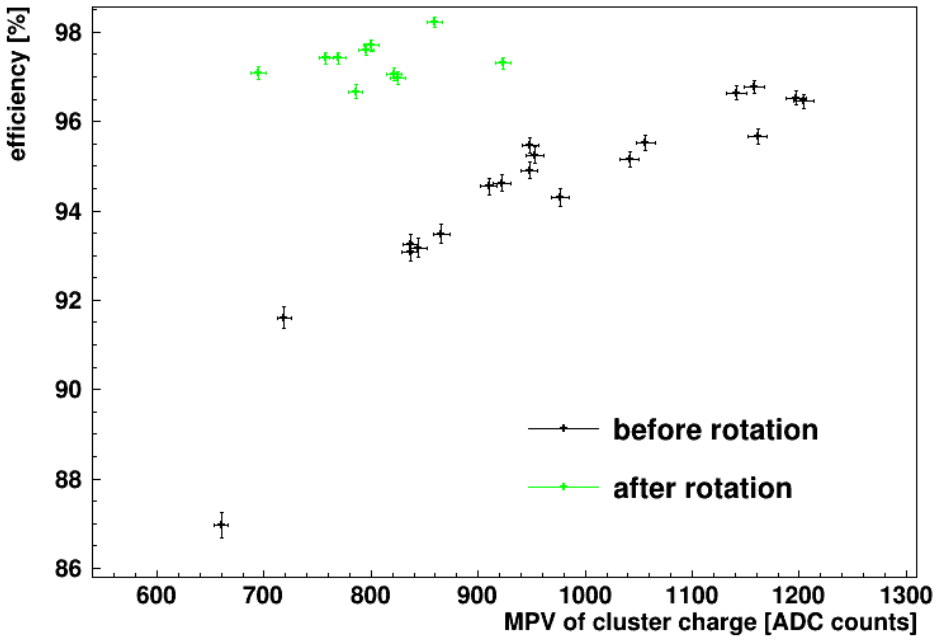

Figure 6.13: Efficiency as a function of the most probable value of the charge distribution. The color coding is the same as in figure 6.9. A correlation between efficiency and charge can be seen.

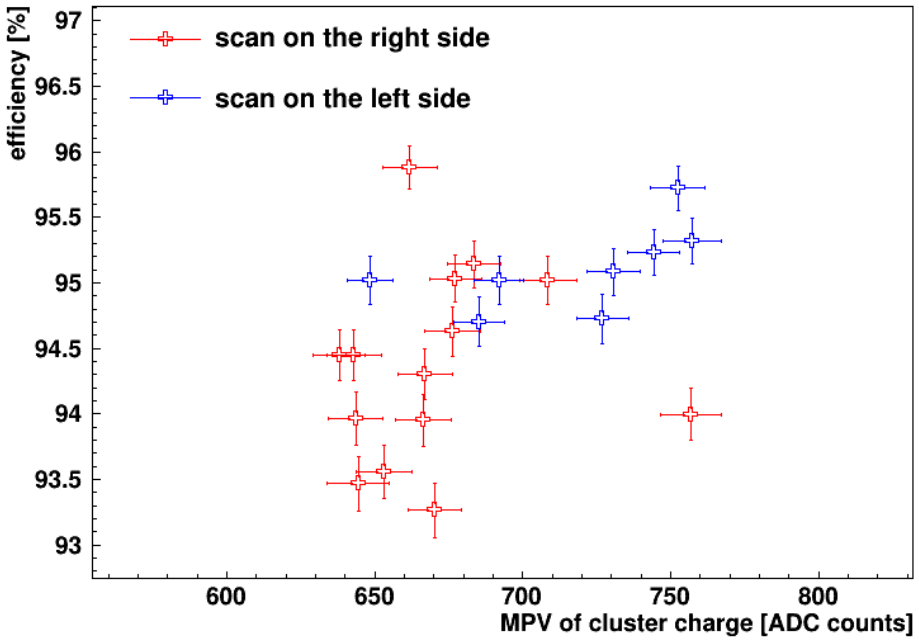

Figure 6.14: Efficiency as a function of the most probable value of the charge distribution. The color coding is the same as in figure 6.14. No correlation can be seen.

6.2.2 Cosmic-Ray Facility

For the determination of the efficiency in the measurements taken in the CRF the residual distribution is used. 99.7 % of the physical events are inside the $\pm 3\sigma$ band, so these are counted as true hits. Figure 6.15 shows the residual versus the predicted position of the cluster. In this analysis always the closest cluster to the prediction was selected. In figure 6.15 also a structured noise distribution can be seen, which comes from the geometrical properties of the If there was no hit inside the $\pm 3\sigma$ band, the position of a noise signals can be closest to the prediction. Because of that the overall efficiency is the number of events inside the $\pm 3\sigma$ band divided by the total number of selected events:

$$\eta = (95.18 \pm 0.03)\,\% \ .$$

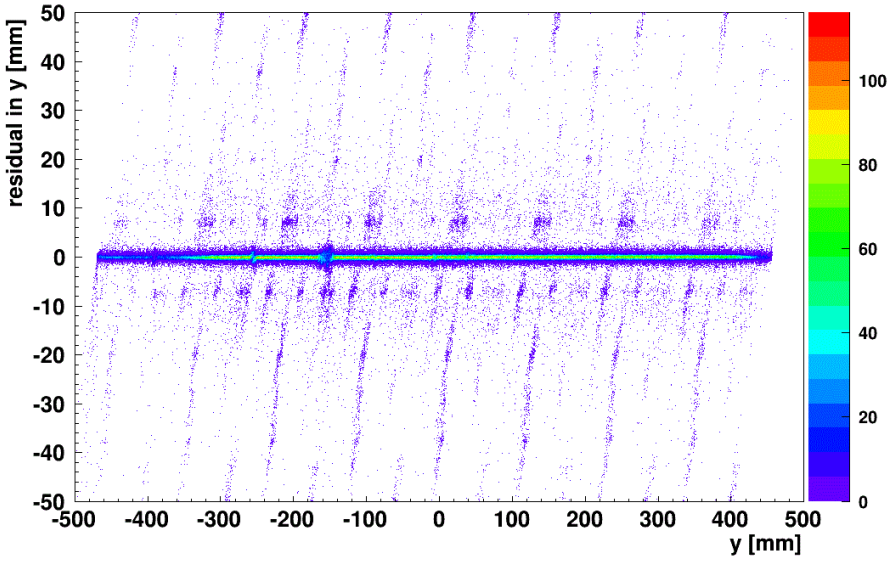

Figure 6.15: Distribution of the residual in y versus the predicted y position from the MDT chambers. As $\pm 3\sigma$ band ± 1.028 mm was taken. The APV25 with the number 5 reads out the strips around position -150 mm and APV25 with number 3 at -250 mm. A possible reason for the structured noise distribution are geometrical properties of the PCB traces

The efficiency was calculated for all detector segments (see figure 6.16). It is mostly homogeneous, but the strips connected to the master frontend boards (see chapter 3) have allways a lower efficiency than the strips read out with slave frontend boards. Except for the first three pairs of APV25, there it is the other way around. The APV25 with the number 5 has the lowest efficiency, because some of the strips connected to that APV25 were accidentally soldered together, so individual charge measurement on these strips is not available. The same can be seen for the APV with number 3, but there is the effect not so large.

Figure 6.17 shows the pulse heights for each detector segment divided by the averaged pulse height over all events. The upper right side has smaller pulse height

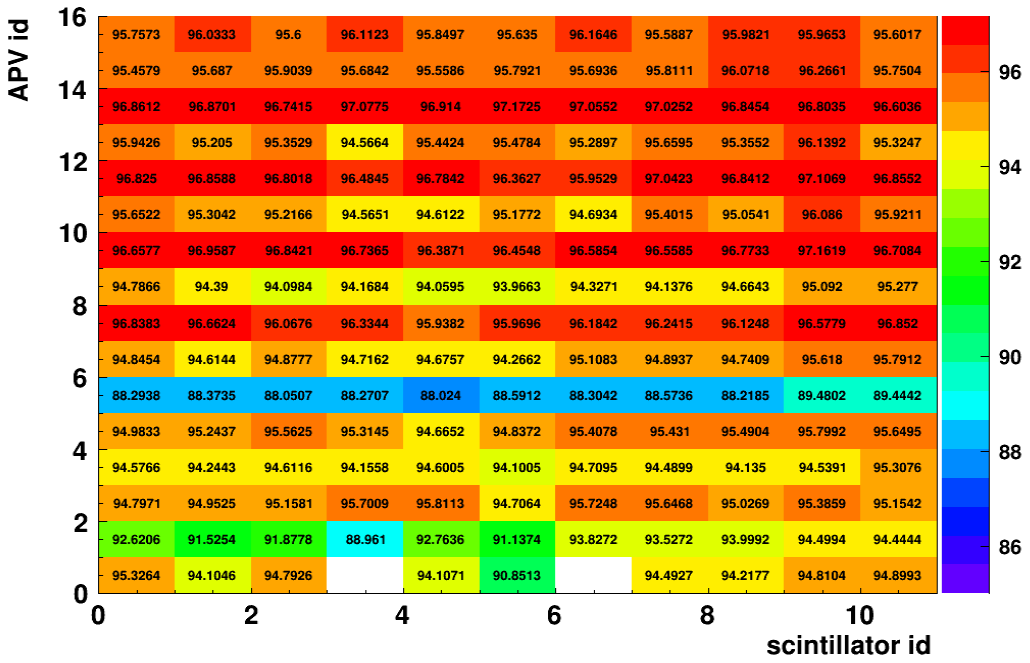

Figure 6.16: Efficiency, calculated for all detector segments.

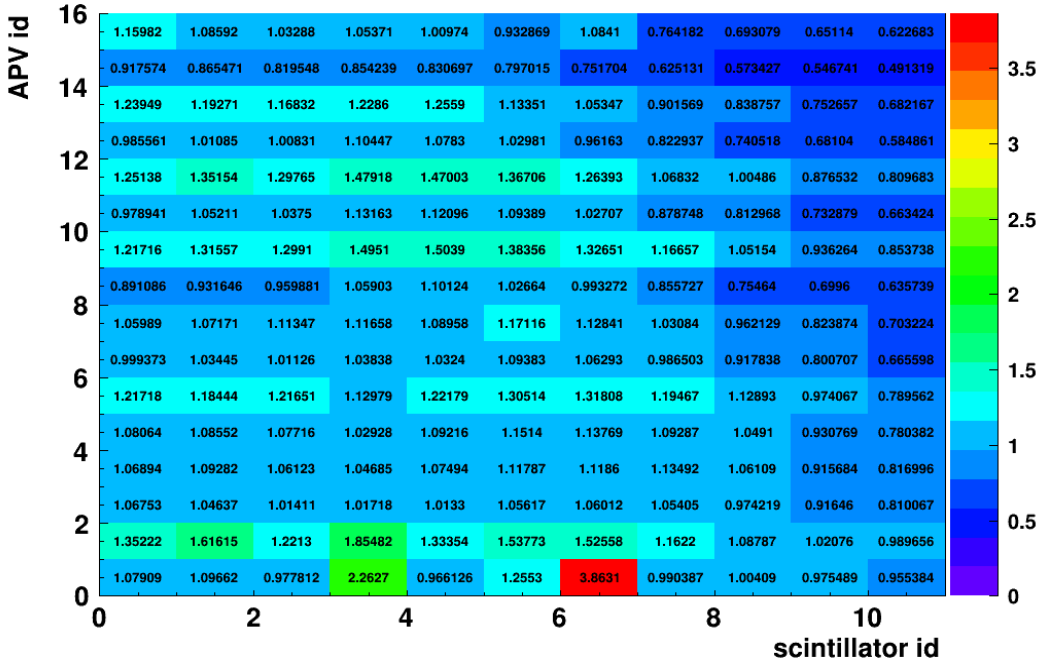

Figure 6.17: Pulse height for all detector segments normalized to the average detector pulse height over all events.

than the rest. The gas input is on the left upper side and the gas output on the right lower side. So on the right upper side the gas mixture is not optimal and the pulse height are lower. It seems like, one effect that can be seen is a correlation between efficiency and charge distribution for each APV25 separately, but only if the determination of the efficiency worked well. There are other effects on the pulse height variations.

A possible explanation for low efficiency on APV25 with number 0 and 1 is, that the photomultiplier of the scintillators stuck out of the edges of the L1 chamber and if they got hit by a muon, they registered the hit, but the test chamber could not see it.

The results for the APV25 with the number 7 are similar to the results from the scan along the strips in the middle of the detector in the pion testbeam.

6.2.3 Discussion

The behaviour of the L1 chamber shown in the testbeam is very similar to the behaviour in the CRF. There are some inhomogeneities with the readout electronics and strips, which are soldered together. But for the size of detector the efficiency is good. It was around 95 % and reached a maximum value of (98.22 ± 0.11) % for the scan in the middle of the detector in the pion testbeam. Due to the not homogeneous gas circulation the pulse height is lower for the parts in the detector with not the optimal gas mixture.

6.3 Signal Propagation Time

For the timing information of the Micromegas the signal propagation on the striplines has to be investigated. On the copper strips the signal has a specific propagation velocity. The signal propagation time on the stripline can be measured.

6.3.1 Pion Testbeam at SPS/CERN

A difference in the arrival time of signals on strips as a function of the cluster position along the strips of the test chamber was observed. For this analysis only the time of the earliest signal detected on a strip within the cluster with the highest charge is used and only for those clusters of the L1 chamber which are in the $\pm 3\sigma$ region of the residual distribution, i.e. which represent physical hits, caused by the traversing pion.

The signal starting point for these strips is histogrammed in figure 6.18. To estimate the maximum of this distribution the central part is fitted with a Gaussian function. This procedure gave the best estimate of the maximum, hereby 75 % of the entries are used for the fit. This is repeated for the whole scan along the strips and plotted versus the y position of the test detector in figure 6.19.

The mean cluster arrival times as a function of the y position is fitted with a straight line. The slope of this line gives the signal propagation time per distance:

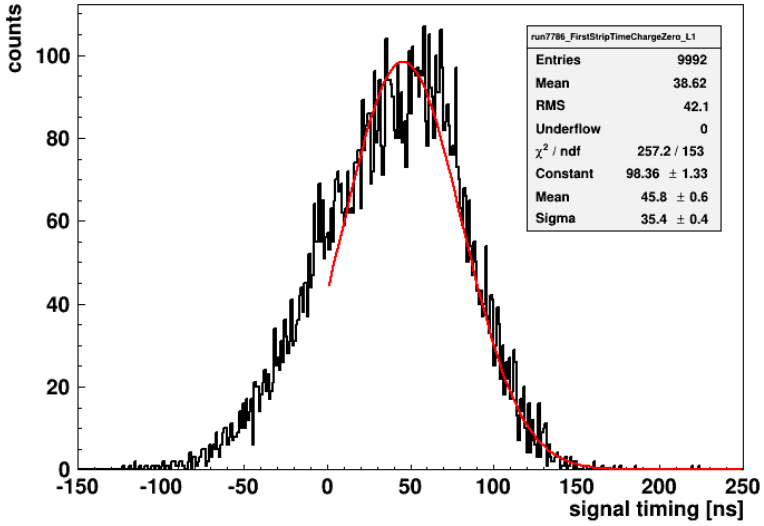

Figure 6.18: Signal timing, fitted with a Gaussian function over the central part.

$$t_{\text{propagation}} = (5.60 \pm 0.64)\,\frac{\text{ns}}{\text{m}}\ . \tag{6.6}$$

6.3.2 Measurement with Cosmic Muons

To confirm this result the measurement with cosmic muons was used, as described in section 5.2. By recording the scintillator signals with a TDC, the asynchronous trigger timing t_{trigger} could be recorded with respect to the synchronous SRS trigger. The Micromegas signal timing, deduced from the APV25 signals, shows a 25 ns jitter with respect to the particle passage as discussed in section 3.1. Figure 6.20 shows the 25 ns broad distribution of the time jitter from the APV25 readout.

To determine the corrected timing t_{cor} the signal time t_{s} was used again from the strip with the shortest signal time in the cluster with the highest charge. In order to eliminate the 25ns time jitter, the measured strip timing t_{s}, the trigger timing t_{trigger}, which is the time difference between the scintillator trigger and the APV25 trigger, and the effective photon time of flight in the scintillator

$$t_{\text{photon}} = \frac{l}{v_{\text{photon}}}$$

are substracted:

$$t_{\text{cor}} = t_{\text{s}} + t_{\text{trigger}} - f_{\text{reflection}} \cdot t_{\text{photon}}\ .$$

$v_{\text{photon}} = c \cdot n^{-1} = 1.899 \times 10^{8}\text{m} \cdot \text{s}^{-1}$ is the propagation velocity of photons in the scintillator with a refractive index of $n = 1.58$ [Saint-Gobain Crystals, 2005], c is the speed of light and l is the distance covered in the scintillator. $f_{\text{reflection}} = -3.33$

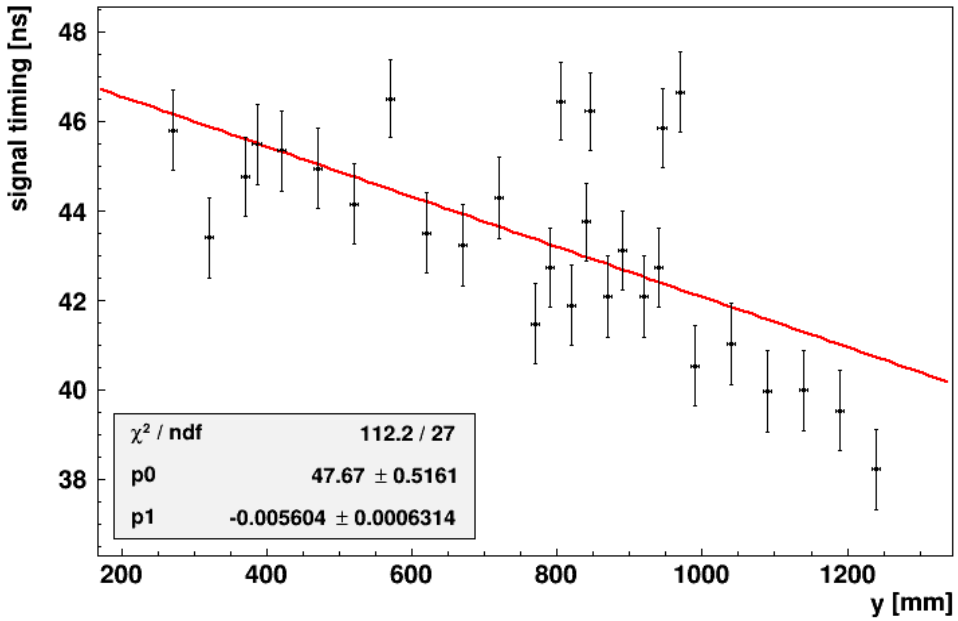

Figure 6.19: Signal timing versus position of the beam spot along the strips of the Micromegas. The readout is at position $y \approx 250\,\text{mm}$.

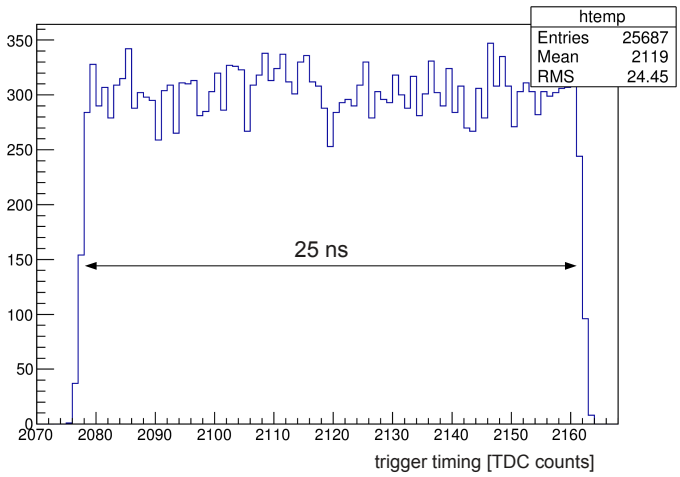

Figure 6.20: 25 ns broad distribution of the trigger time (1 TDC count = 296 ps).

is the correction factor of the reflections of the muons on the scintillator surfaces (see section 6.4.2).

Figure 6.21 shows the values for t_{cor} as a function of the muon hit position in the detector, where the readout side is at position zero. Fitting this distribution with a straight line gives for the signal propagation time:

$$t_{\text{propagation}} = (6.59 \pm 0.57)\,\frac{\text{ns}}{\text{m}}\ . \tag{6.7}$$

Although signal propagation time on the stripline is by about 18 % higher than the value previously measured with pions the results from both measurements agree within their errors. There could be a systematic error because of the 9.5 cm wide scintillators.

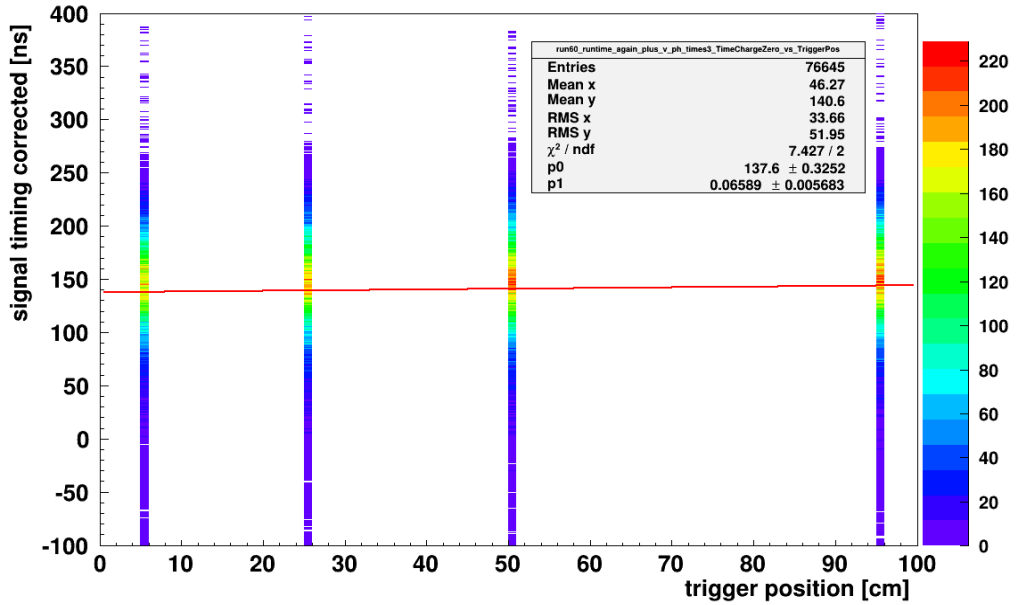

Figure 6.21: Signal timing as a function of the muon hit position, fitted with a straight line. The readout is at position zero.

6.3.3 Discussion

The two measured values agree within their quoted uncertainties. The average from both measurements gives the mean signal propagation time of the the striplines in resistive strip Micromegas:

$$\overline{t_{\text{propagation}}} = (6.10 \pm 0.61)\,\frac{\text{ns}}{\text{m}}\ .$$

$$t_{\text{propagation,lit}} = 0.0334\sqrt{0.48 \cdot \epsilon + 0.7}\ \left[\frac{\text{ns}}{\text{m}}\right] = 5.64\,\frac{\text{ns}}{\text{m}}\ , \tag{6.8}$$

where $\epsilon = 4.5$ is the dielectric constant of FR4 (PCB material). $t_{\text{propagation,lit}}$ is taken from [Nührmann, 1994], which gives a description of the stripline with its signal propagation time.

The two values agree well within the quoted uncertainty. That shows, that if large Micromegas detectors shall be used for triggering purposes in the new Small Wheels in the ATLAS detector, the signal timing has to be corrected for the signal propagation time of the stripline. For Micromegas with a strip length of 2 m the events could otherwise be matched to the wrong bunch crossing.

6.4 Angular Resolution

The last property investigated in this thesis is the angular resolution.

6.4.1 Pion Testbeam at SPS/CERN

Specific runs have been taken, which allow for investigating the angular resolution of the L1 micromegas chamber. The detector was rotated around the strip direction with the values -10°, -20° and -30°.

To reconstruct the track angle the μTPC mode is used as explained in section 4.4.

Before the angle of incidence can be reconstructed, the effective drift velocity had to be determined. That can be done by solving the μTPC equation (4.12) for the drift velocity and use the true angle α, which is known from the rotation of the chamber:

$$v_{\text{drift}} = \frac{\text{p}}{m \cdot \tan\alpha \cdot \text{tb}} \ ,$$

where p is the pitch of the strips, tb the length of one timebin (25 ns) and m the slope of the fitted straight line (Eq. (4.9)) in the time-strip-space.

The reconstructed drift velocity is plotted in figure 6.22. As effective drift velocity the value at the maximum of the distribution is taken. This leads for an electric drift field of $E_{\text{drift}} = 600\,\text{V/cm}$ to

$$v_{\text{drift}} = (0.051 \pm 0.004)\,\frac{\text{mm}}{\text{ns}} \ .$$

The simulated result from figure 2.3 for an electric drift field of $E_{\text{drift}} = 600\,\text{V/cm}$ is

$$v_{\text{drift}} = 0.046\,\frac{\text{mm}}{\text{ns}} \ .$$

The reconstructed angles Θ are filled in histograms for the three different angles (see figure 6.23 - 6.25). It can be seen, that the angle reconstruction works better for larger angles of incidence. About 50 % of the entries in the central part of the histogram are used for the fit with a Gaussian function. For the entries in the histogram, which were not used for the fit, the reconstruction did not work. As value for the reconstructed angle the mean of the Gaussian function in taken, its width gives the angular resolution. The result for the reconstructed angle is plotted in figure 6.31 and the result for the angular resolution in figure 6.32 together with the results for the CRF measurement.

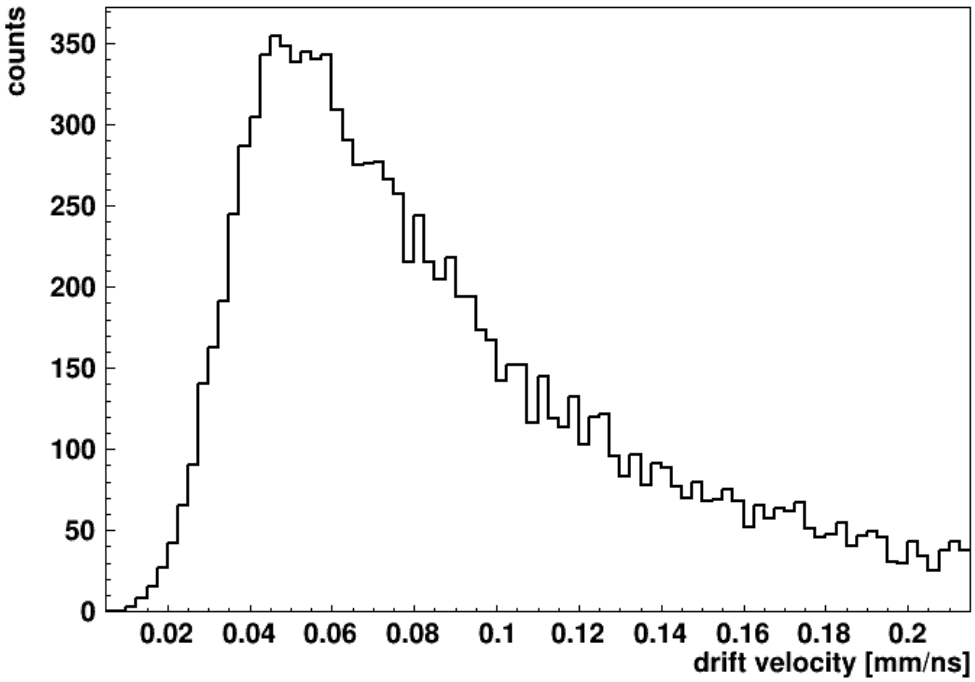

Figure 6.22: Distribution of the drift velocity.

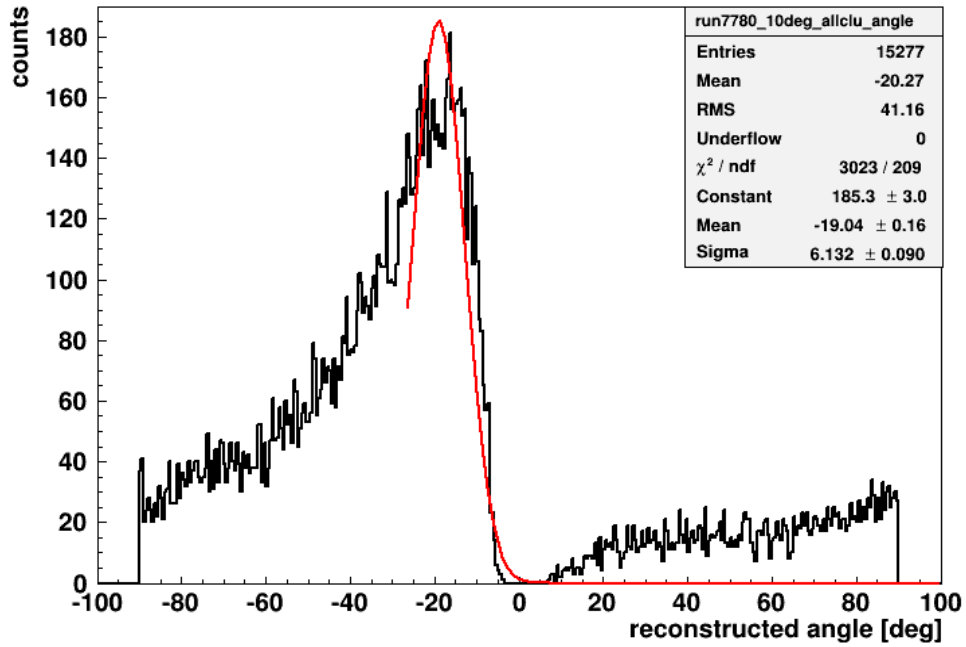

Figure 6.23: Distribution of the reconstructed angle Θ for the angle of incidence $|\alpha| = 10°$, the central part is estimated with a Gaussian function.

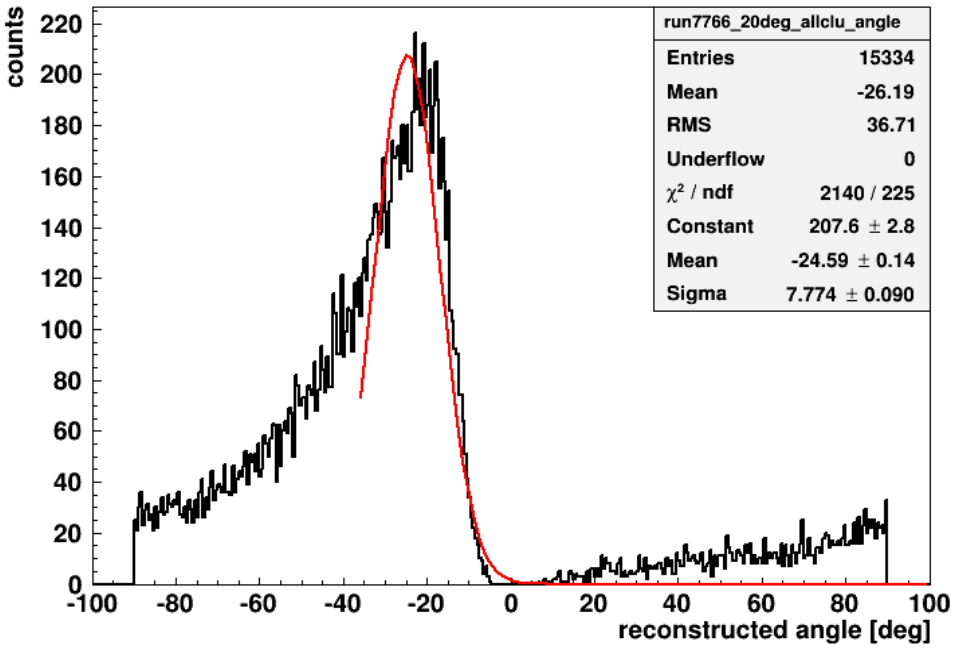

Figure 6.24: Distribution of the reconstructed angle Θ for the angle of incidence $|\alpha| = 20°$, the central part is estimated with a Gaussian function.

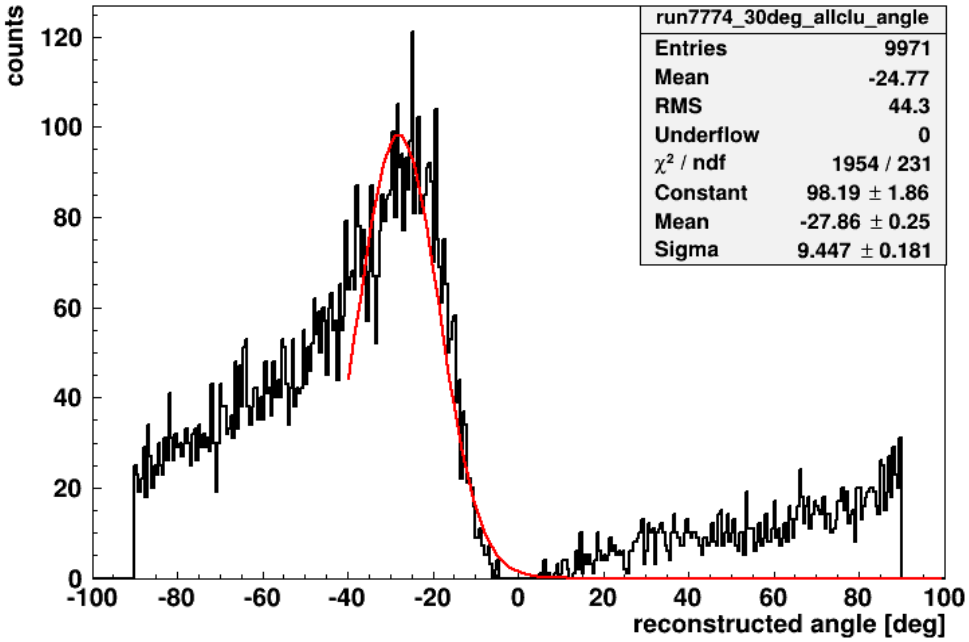

Figure 6.25: Distribution of the reconstructed angle Θ for the angle of incidence $|\alpha| = 30°$, the central part is estimated with a Gaussian function.

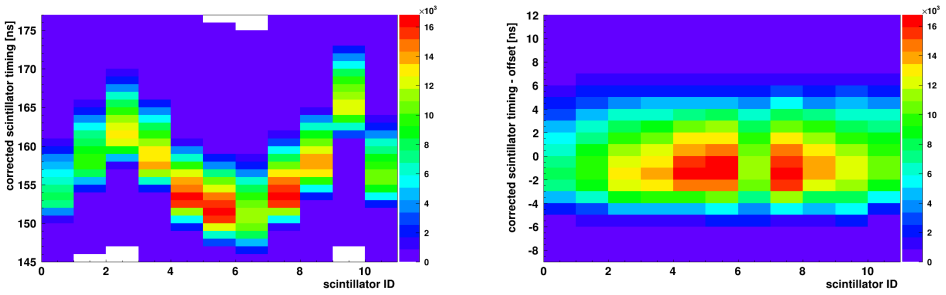

Figure 6.26: Scintillator timing as a function of the scintillator ID without correction (left) and offset corrected (right).

6.4.2 Cosmic-Ray Facility

Determination of the Signal Timing Correction

Via μTPC method (see in section 4.4) it is possible to reconstruct the hit in the detector. Therefore the straight line from the μTPC fit is extrapolated to the readout plane. But due to the offset of the signal timing t_s it has to be calibrated. The readout of muon signals has three different time intervals, which have to be accounted for:

- the 25 ns time jitter (see section 3.1),
- the TDC offsets from the readout of the scintillators and
- the photon propagation time in the scintillators.

This is done with a correction, which can be determined with the additional trigger scintillators on the Micromegas.

The calibration starts with the TDC offsets by adding the scintillator timing $t_{\text{scintillator}}$, which is shown in figure 6.26 (left). It can be seen, that all scintillators have a different offset, so the offset t_{offset} has to be subtracted (see figure 6.26 (right)).

The scintillator timing has to be, additionally to the offset, corrected by the photon propagation time in the scintillator t_{photon} (photon timing). Figure 6.27 (left) shows the correlation of scinitillator and photon timing. The assumed photon timing $t_{\text{photon}} = l \cdot n \cdot c^{-1}$ has to be corrected by a factor $f_{\text{reflection}}$, where l is the real distance covered in the scintillator, c the speed of light and n the refraction index of the scintillator material. The photons in the scintillator get reflected on the sides, so the effective distance covered in the scintillator is longer than the real distance. $f_{\text{reflection}} = -3.33$ is the inverse of the slope of the correlation in figure 6.27 (left).

To eliminate the 25 ns time jitter between particle passage and APV25 trigger, the trigger timing t_{trigger}, which is given as correction time of the MDT chambers, has to be subtracted from the signal timing. Figure 6.28 shows the correlation of these two values.

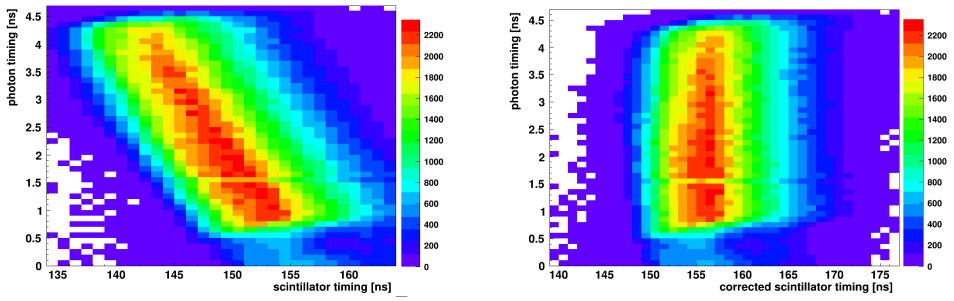

Figure 6.27: Photon propagation time in the scintillator as a function of the scintillator timing (left) and as a funtion of the corrected scintillator timing (right).

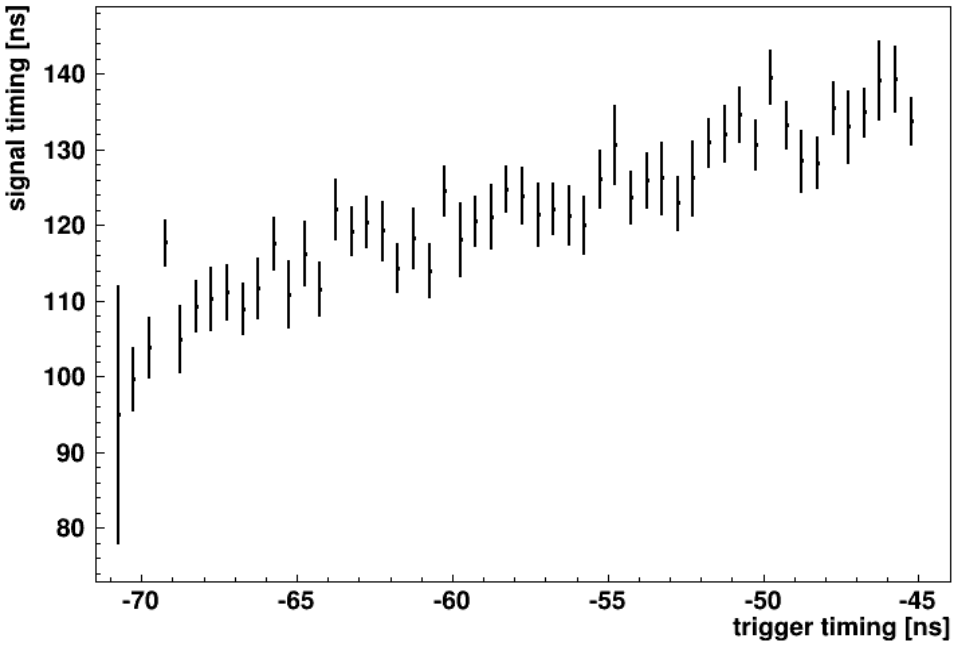

Figure 6.28: Correlation between signal and trigger timing, used for the timing correction.

These corrections yield the corrected timing t_{cor}:

$$t_{\mathrm{cor}} = t_{\mathrm{s}} + (t_{\mathrm{scintillator}} - t_{\mathrm{offset}} - f_{\mathrm{reflection}} \cdot t_{\mathrm{photon}}) - t_{\mathrm{trigger}} \ . \tag{6.9}$$

The corrected timing is used in the following section for the μTPC method.

Reconstruction of the Track Angle

All the events in the $\pm 3\sigma$ band of the residual distribution were used for the angular resolution analysis. The average angles of the two tracklets reconstructed in the reference chambers is in the following used as reference angle.

Because of the different electric field in the drift region as compared to sec 6.4.1, the effective electron drift velocity was determined again for the electric field of $E = 350\,\mathrm{V/cm}$:

$$v_{\mathrm{drift}} = (0.039 \pm 0.002)\,\frac{\mathrm{mm}}{\mathrm{ns}} \ .$$

The simulated result from figure 2.3 for an electric drift field of $E = 350\,\mathrm{V/cm}$ is

$$v_{\mathrm{drift}} = 0.037\,\frac{\mathrm{mm}}{\mathrm{ns}} \ .$$

With this drift velocity the angle of incidence Θ is reconstructed and filled in histograms. Figure 6.29 and 6.30 are two examples for the angle reconstruction. These distributions were fitted like the ones for the measurement in the pion testbeam (see section 6.4.1). The fits work with the optimized operational parameters better than for the data from the pion testbeam. The reconstructed angle as a function of the track angle are plotted in figure 6.31 together with the result of the measurement in the pion testbeam. It can be seen, that the angle reconstruction does not work for track angles smaller than 10° (see also [ATLAS Collaboration, 2013]). For angles larger than 10°, it works the better the larger the track angle is. The reconstructed angles do not agree with their prediction, but for predicted angles larger than 10° the function rises monotonously. So these angle can be corrected.

By comparing the assumed track angle, given by the reference chambers and the measured track angle in the Micromegas, it was possible to determine the angular resolution. For this, the central peak of the residual distribution was fitted with a Gaussian function. The data points in the μTPC method can be weighted for the fit. The angular resolution was determined for twice. Once with equally weighted pata points and then the pulseheight was used as weight. The angular resolution for the charge weighted data points is slightly better than for the equally weighted data points (see figure 6.32). The best result is for the large track angle of 30°, there the angular resolution is about $\sigma_{\Theta} = (5.66 \pm 0.12)°$.

6.4.3 Discussion

The angle reconstruction worked because of the optimization of the Micromegas operational parameters for the measurement in the CRF better than for the

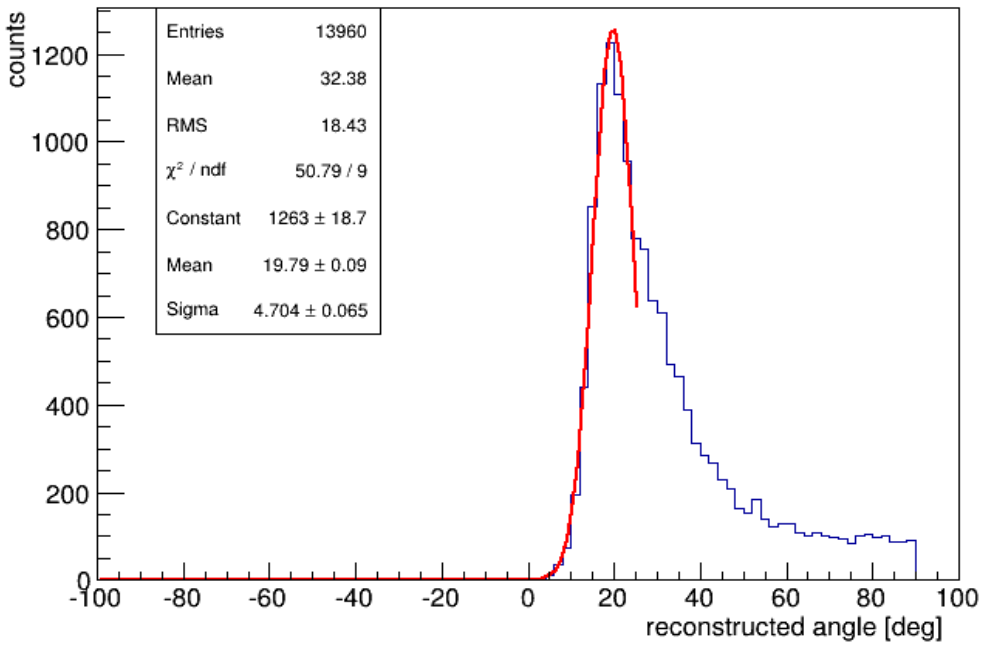

Figure 6.29: Distribution of the reconstructed angle Θ for the angle of incidence $|\alpha| = 20°$, the central part is estimated with a Gaussian function.

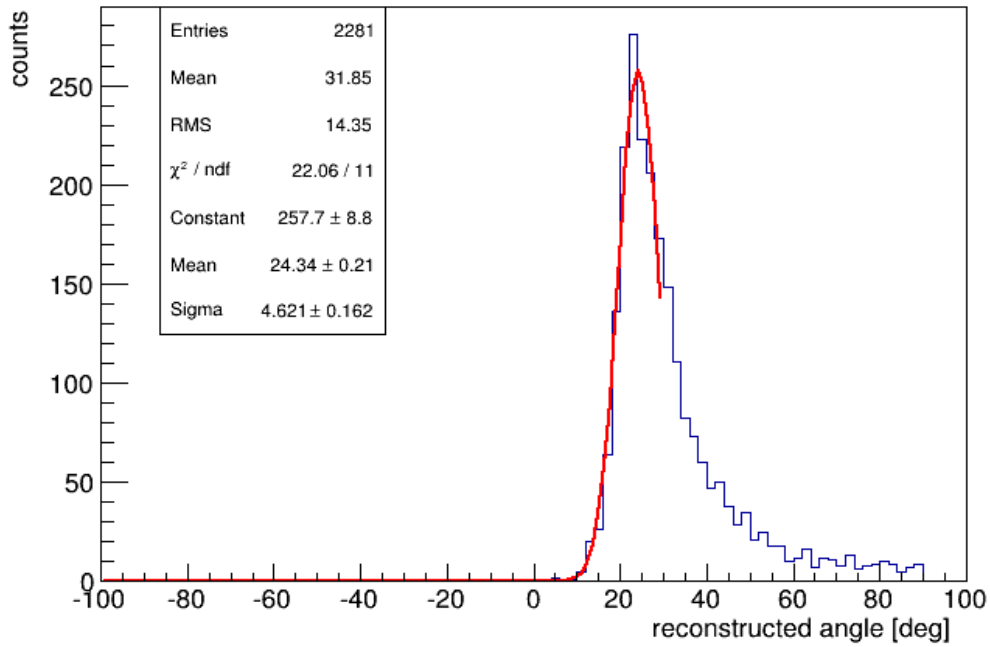

Figure 6.30: Distribution of the reconstructed angle Θ for the angle of incidence $|\alpha| = 30°$, the central part is estimated with a Gaussian function.

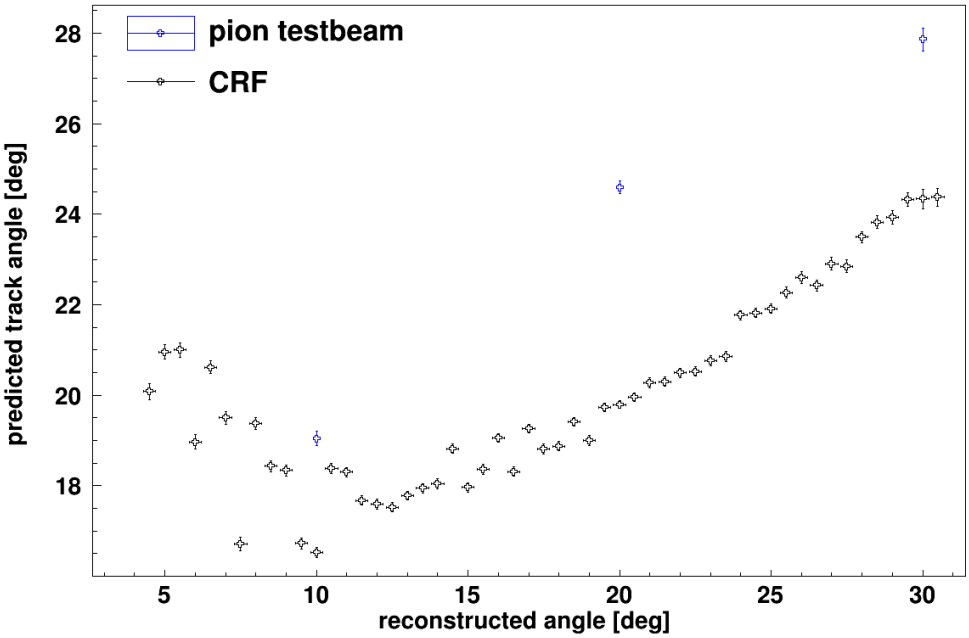

Figure 6.31: Reconstructed angle as a function of the predicted track angle. The black markers represent the measurement at the CRF and the blue markers the measurement in the pion test beam. For angles smaller than 10° this method does not work. For larger angles the function rises monotonously, so it can be corrected.

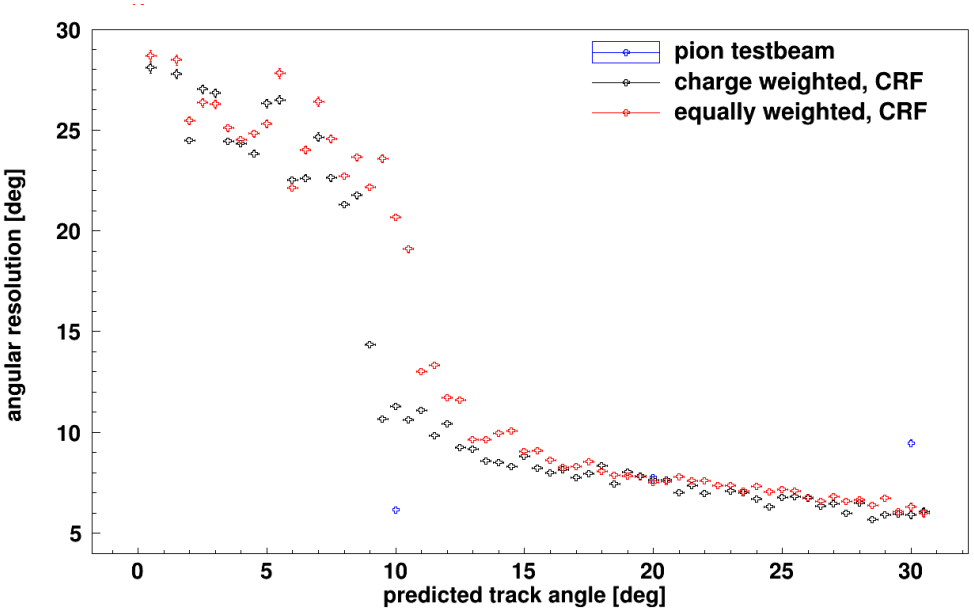

Figure 6.32: Angular resolution as a function of the predicted track angle. The black markers represent the μTPC method with charge weighted data points and the red markers with equally weighted data points, both results are from the CRF. The blue markers represent the result from the measurement in the pion testbeam.

measurement in the pion testbeam. If the pulse height is used as weight for the μTPC method, the reconstruction works better and an angular resolution of $\sigma_\Theta = (5.66 \pm 0.12)^\circ$ for large angles of incidence can be reached. The angle reconstruction is better for large track angles than for small ones.

7 Summary and Outlook

A $1\,\mathrm{m}^2$ large Micromegas detector was investigated in three measurement campaigns. First, in a 120 GeV pion testbeam at SPS/CERN, where the beam spot had a area of about $1\,\mathrm{cm}^2$ and, due to the high pion momentum multiple scattering. Then a dedicated measurement with cosmic muons in Garching/Munich is presented investigating the signal propagation time on readout strips with improved timing capabilities. Finally, the overall homogeneity with respect to pulse height, efficiency, mechanical accuracy and spatial resolution was investigated in the Cosmic-Ray Facility, which has a good track prediction of about 40 μm. In which the Micromegas detector could be installed on an aluminium support stage. Computer programs were developed to analyze the data from the three measurement and to merge different data streams.

The large Micromegas detector has shown an averaged spatial resolution of $\overline{\sigma_{\mathrm{sr}}} = (83.0 \pm 0.9)\,\mu$m in the scan along the strips with perpendicular incident 120 GeV pions. The scans along the strips on the edges of the test chamber did not show such a good result, because of the slightly degraded track accuracy as compared to the scan in the middle of the detector. The results $\sigma_{\mathrm{sr}} = (238.7 \pm 1.3)\,\mu$m in the Cosmic-Ray were not as good as for the pion testbeam, but that is not entirely understood. It is probably due to the not optimized reference track reconstruction in this specific setup. How the temperature dependence and the cuts on the MDT track influences the residual distribution, has to be studied. The spatial resolution calculated with the centroid method is even for angles of 30 degrees smaller than the spatial resolution determined with the μTPC method. After some necessary improvements, the μTPC spatial resolution should show similar or better results than the centroid method.

The behaviour of the L1 chamber demonstrated in the pion testbeam is very similar to the behaviour in the CRF. There are some pulse height and efficiency inhomogeneities due to the differing behavior of master and slave APV25 readout electronics and noisy regions in the detector, which are created by badly soldered or interconnected readout strips. But nevertheless for the size of detector the overall efficiency of 95 % is very satisfactory. It reached a maximum value of (98.22 ± 0.11) % for the scan in the middle of the detector in the pion testbeam. Due to the not homogeneous gas circulation within the detector the pulse height is lower within the detector regions with the not optimal gas mixture. Although the efficiency behavior seems to be complex correlation between pulse height and efficiency has been observed.

The analysis for the signal propagation time on the readout strips led to two consistent results. With 120 GeV pions, a signal propagation time of $t_{\mathrm{propagation}} = (5.60 \pm 0.64)\,\mathrm{ns} \cdot \mathrm{m}^{-1}$ has been measured. With cosmic muons we observe a propagation time of $t_{\mathrm{propagation}} = (6.59 \pm 0.57)\,\mathrm{ns} \cdot \mathrm{m}^{-1}$. Both values are equivalent within

their respective uncertainty. The averaged result $\overline{t_{\text{propagation}}} = (6.10 \pm 0.61)\,\text{ns} \cdot \text{m}^{-1}$ agrees well with the literature value of $t_{\text{propagation}} = 5.64\,\text{ns} \cdot \text{m}^{-1}$. That shows, that if large Micromegas detectors is to be used for triggering purposes in the new Small Wheels in the ATLAS detector, the signal timing has to be corrected for the signal propagation time time of the stripline. For Micromegas with a strip length of 2 m the events could otherwise be matched to the wrong bunch crossing.

It could be demonstrated, the with the large L1 Micromegas, a reconstruction of the track inclination is possible in a single plane. The performance in the CRF has been better than in the high-energy pion test beam, because of the explicit optimization of the Micromegas operational parameters. If the single strip pulse height is used as weight for the μTPC method, the reconstruction improves and an angular resolution of $\sigma_\Theta(5.66 \pm 0.12)^\circ$ for large angles of incidence can be reached. As expected the angle reconstruction is better for large track angles than for small ones.

Overall the detector showed a good performance.

Bibliography

[ALICE Collaboration, 2008] ALICE Collaboration (2008). The ALICE Experiment at the CERN LHC. *JINST*, 3.

[Andriamonje et al., 2004] Andriamonje, S., Aune, S., Dafni, T., Fanourakis, G., Ferrer Ribas, E., Fischer, H., Franz, J., Geralis, T., Giganon, A., Giomataris, Y., Heinsius, F., Königsmann, K., Papaevangelou, T., and Zachariadou, K. (2004). A Micromegas detector for Athe CAST experiment. *Nucl.Instrum.Meth. A*, 518(1-2):252–255.

[ATLAS Collaboration, 2008] ATLAS Collaboration (2008). The ATLAS Experiment at the CERN Large Hadron Collider. *JINST*, 3.

[ATLAS Collaboration, 2013] ATLAS Collaboration (2013). New Small Wheel Technical Design Report. (May).

[Beringer, J. et. al. (Particle Data Group), 2012] Beringer, J. et. al. (Particle Data Group) (2012). Review of Particle Physics. *Physical Review D*, 86(1):010001.

[Bortfeldt, 2013] Bortfeldt, J. (2013). Private conversation.

[Bortfeldt et al., 2012] Bortfeldt, J., Biebel, O., Heereman, D., and Hertenberger, R. (2012). Development of a High-Resolution Muon Tracking System Based on Micropattern Detectors. *Nuclear Science, IEEE Transactions on*, 59(4):1252–1258.

[Bortfeldt et al., 2013] Bortfeldt, J., Biebel, O., Hertenberger, R., Lösel, P., Moll, S., Müller, R., Ruschke, A., and Zibell, A. (2013). Floating Strip Micromegas Detector. *poster, presented at 13th Vienna Conferece on Instrumentation - VCI2013*.

[Carnegie et al., 2005] Carnegie, R. K., Dixit, M. S., Dubeau, J., and Karlen, D. (2005). Resolution studies of cosmic-ray tracks in a TPC with GEM readout. *Nucl.Instrum.Meth. A*, 538(February 2008):372–383.

[CERN website, 2008] CERN website (2008). Big Science. *http://bigscience.web.cern.ch*, (last visited 25.9.2013).

[CMS Collaboration, 2008] CMS Collaboration (2008). The CMS Experiment at the CERN LHC. *JINST*, 3.

[Dubbert et al., 2002] Dubbert, J., Binder, M., Hertenberger, R., Elmsheuser, J., Kortner, O., Rauscher, F., Rykaczewski, M., Sahr, O., Schaile, D., Staude, A.,

Steffens, H., Stiller, W., Zhuravlov, V., and Zupančič, C. (2002). First Results from the Cosmic-Ray Test-Facility at LMU Munich.

[Garfield, 2013] Garfield (2013). http://garfield.web.cern.ch/garfield/.

[Giomataris et al., 1996] Giomataris, Y., Rebourgeard, P., Robert, J. P., and Charpak, G. (1996). MICROMEGAS : a high-granularity position-sensitive detector for high particle-flux environments. *Nucl.Instrum.Meth. A*, 376:29–35.

[Groom et al., 2001] Groom, D. E., Mokhov, N. V., and Striganov, S. I. (2001). Muon Stopping Power and Range Tables 10Mev - 100TeV. *Atomic Dta and Nulear Data Tables*, 78(2):183–156.

[Horvat, 2005] Horvat, S. (2005). Study of the Higgs Discovery Potential in the Process pp $\rightarrow$ H $\rightarrow 4\mu$. *Dissertation (Zagreb University)*.

[Jones, 2001] Jones, L. (2001). APV25-S1 User Guide. (September):1–20.

[Leo, 1994] Leo, W. R. (1994). *Techniques for Nulear and Particle Physics Experiments*. Springer, second edition.

[LHCb Collaboration, 2008] LHCb Collaboration (2008). The LHCb Detector at the LHC. *JINST*, 3.

[Martoiu et al., 2011] Martoiu, S., Muller, H., and Toledo, J. (2011). Front-end electronics for the Scalable Readout System of RD51. *Nuclear Science Symposium and Medical Imaging Conference (NSS/MIC)*, pages 2036–2038.

[Nikolopoulos et al., 2009] Nikolopoulos, K., Alexopoulos, T., Altintas, A. A., Alviggi, M., Arik, M., Cetin, S. A., Chernyatine, V., Cheu, E., Volpe, D. D., Dris, M., Fassouliotis, D., Gazis, E. N., Giordano, R., Gratchev, V., Guan, L., Iengo, P., Ioannou, P., Li, C., Johns, K., Kaushik, V., Khodinov, A., Kourkoumelis, C., Maltezos, S., Mermigka, K., MÃijller, H., Park, W., Persembe, S., Petridou, C., Petti, R., Polychronakos, V., Purohit, M. V., Sampsonidis, D., Sekhniaidze, G., Shao, M., Sun, Y. J., Tsipolitis, G., Veenhof, R., Wang, X. L., Wotschack, J., Wu, S. X., Zhao, T., and Zhao, Z. G. (2009). The ATLAS muon Micromegas R&D project: towards large-size chambers for the s-LHC. *Journal of Instrumentation*, 4(12):P12015.

[Nührmann, 1994] Nührmann, D. (1994). *Das komplette Werkbuch Elektronik, Band 3&4*. Franzis'.

[Nygren and Marx, 1978] Nygren, D. R. and Marx, J. N. (1978). The Time Projection Chamber. *Physics Today*, (October):46.

[Panasonic Corporation, 2013] Panasonic Corporation (2013). P5K, P5KS Series - For board-to-board Narrow pitch connectors (0.5mm pitch). *http://pewa.panasonic.com/assets/pcsd/catalog/p5k-catalog.pdf*.

[Placidi et al., 2000] Placidi, P., Marchioro, A., and Moreira, P. (2000). CMS Tracker PLL Reference Manual. *CERN - EP/MIC, Geneva Switzerland*.

[Platchkov et al., 2003] Platchkov, S., Abbon, P., Ball, J., Bedfer, Y., Bernet, C., Delagnes, E., Giganon, a., Kunne, F., Le Goff, J.-M., Magnon, a., Marchand, C., Neyret, D., Pereira, H., Rebourgeard, P., and Thers, D. (2003). A large size MICROMEGAS detector for the COMPASS experiment at CERN. *2002 IEEE Nuclear Science Symposium Conference Record*, 1:292–296.

[Rauscher, 2005] Rauscher, F. (2005). Untersuchung des Verhaltens von Driftrohren bei staker γ Bestrahlung sowie Vermessung von Driftrohrkammern mit Hilfe von Myonen der kosmischen Höhenstrahlung. *Dissertation (LMU Munich)*, pages 75–90.

[Saint-Gobain Crystals, 2005] Saint-Gobain Crystals (2005). Premium Plastic Scintillators. *Data Sheet*.

[Thomson, A. C. et. al., 2009] Thomson, A. C. et. al. (2009). X-RAY DATA BOOKLET. *LBNL University of California*.

[Toledo et al., 2011] Toledo, J., Muller, H., Esteve, R., MonzÃş, J. M., Tarazona, A., and Martoiu, S. (2011). The front-end concentrator card for the rd51 scalable readout system. *Journal of Instrumentation*, 6(11):C11028.

[Zibell, 2013] Zibell, A. (2013). High Background Rate Investigation on small Monitored Drift Tubes and Development of a Readout System for Micromegas with SRS. *Dissertation in preparation (LMU Munich)*.

Acknowledgments

Ich möchte folgenden Personen danken:

- Prof. Dr. Otmar Biebel für die Möglichkeit diese Arbeit am Lehrstuhl für experimentelle Teilchenphysik zu schreiben.
- Dr. Ralf Hertenberger für die herausragende Betreuung und die Unterstützung bei allen Messungen.
- Prof. Dr. Dorothee Schaile für das gute Arbeitsklima an ihrem Lehrstuhl.
- Der MAMMA collaboration für die zur Verfügung Stellung des Micromegas Detektors.
- Jona Bortfeldt für die hervoragende Hilfe, immer wenn ich sie gebraucht habe, und die vielen guten Ideen.
- Dr. Felix Rauscher und Andre Zibell für die Hilfe beim Auslesen der Detektoren.
- Der ganzen Hardware Gruppe, weil es echt Spaß gemacht hat.
- Und meiner Familie für die seelische und materielle Unterstützung.

Selbstständigkeitserklärung

Hiermit erkläre ich, dass ich die vorliegende Arbeit selbstständig angefertigt und keine anderen als die angegebenen Quellen und Hilfsmittel benutzt habe.

München, den 2.10.2013